LARGE DEFORMATION NONLINEAR FEA
AND APPLICATIONS FOR
METAL FORMING PROCESSES

by

Wan Cheng, M.Eng

A thesis
Submitted to the School of Graduate Studies
in Partial Fulfilment of the Requirements
for the Degree of
Doctor of Philosophy

McMaster University
August 1995

LARGE DEFORMATION NONLINEAR FEA AND APPLICATIONS FOR METAL FORMING PROCESSES

DOCTOR OF PHILOSOPHY | McMASTER UNIVERSITY

(Mechanical Engineering) | Hamilton Ontario

TITLE: Large Deformation FEA and Applications for Metal Forming Processes

AUTHOR: Wan Cheng

(B.Eng. - Taiyuan Heavy Machinery Institute, China)

(M.Eng. - Beijing University of Iron and Steel Tech., China)

(M.Eng. - McMaster University)

SUPERVISOR: Professor Mateusz P. Sklad

NUMBER OF PAGES: 140

ABSTRACT

The contents of this thesis reflect a general effort in the endeavour of exploring and developing the effective FEM tools for metal forming analysis. There are three major parts in this work.

In chapter 2, an unique mathematical derivation of large deformation equations is presented on the basis of a direct linearization of the "future" virtual work equation without using any pseudo stress tensor and corresponding conjugate strain tensor. A major advantage of this derivation is that a clear physical understanding is carried through the whole mathematical process. Therefore distinctive perception on key fundamentals such as: equilibrium equation, strain measure, constitutive relation, stress rotation and residual force evaluation are presented and discussed on a consistent and integrated basis. The code developed in this part of work forms an independent module for 2D bulk forming analysis, while the methodology is carried through the rest of thesis.

A particular effort is described in Chapter 3, which addresses the problem and techniques used in dealing with the frictional contact boundary condition which is common in metal forming processes. A typical ring compression problem is used to show the problem and solution. The algorithm and code developed there is a part of the 2D package.

Chapter 4 presents a full description of a 3D degenerated shell element formulation based on the consistent large deformation formulation presented in Chapter 2. Various aspects of techniques used in shell elements to prevent elements from locking have been reviewed. A special penalty method is devised to enforce the Kirchhoff constraint which has been missing in the degenerated shell element discretization. The method has successfully prevented 3-node and 4-node elements from shear locking in analysing the typical cup

drawing process.

At the end of the thesis, a summary of the thesis is presented. Conclusions and recommendations for further work are provided.

ACKNOWLEDGEMENTS

I wish to express my sincere appreciation to my supervisor, Dr. M. Sklad, for his constant guidance and support during the course of this work. I also want to extend this appreciation to Dr. R. Sowerby for the valuable discussions with him.

Sincere thanks are owed to Dr. D. AE. Oravas, Civil Engineering and Engineering Mechanics Department, McMaster Univ.. His excellent course of "Continuum Mechanics" has always been a great inspiration for me throughout this study.

The financial support from the Department of Mechanical Engineering and the Natural Science and Engineering Research Council of Canada are gratefully acknowledged.

Thanks are also due to Marianne Van Der Wel, computing service co-ordinator, for her consistent support for my heavy usage of computing facilities.

Finally, I owe my deepest thanks to my wife, Ye Li and daughter, Becky Cheng. Without their constant understanding and sacrifices, the completion of this thesis would be impossible.

CHAPTER 1

Introduction

§1 Metal Forming and FEA

Metal forming has historically played a distinctive role in the process of industrialization, and remains one of the most important industries in the modern economy. Metal forming processes can be categorized into two major groups: one is bulk forming, which contains various traditional forming methods, such as: forging, rolling, extrusion, etc. The other is sheet metal forming which primarily refers to stamping processes.

Metal forming has been a traditional research field in mechanical engineering. Most of the time, its content has been exclusively related to the mechanical behaviour of metal forming processes. The theoretical development in this field has been closely connected to the developments of the theory of plasticity and computer methods.

Although most of the mathematical fundamentals on plasticity have been established for nearly one hundred years, metal forming processes still represent a major challenge to modern engineering analysis methods. In terms of mechanics, almost all metal forming processes involve large deformation with nonlinear material behaviour and contact boundaries. All of these natures make the analysis of such a process extremely nonlinear.

Since about 1970, finite element method (FEM) has brought a new era to the analysis of metal forming processes. With FEM, metal forming processes could be solved with minimum mathematical simplifications, which made it possible to simulate the whole deformation process with the history of material yielding, hardenning, loading and unloading, etc. The finite element method is also able to consider thermal and boundary contact and friction effects, etc.

In the early years of finite element analysis of metal forming processes, successes were mainly concentrated in the field of small deformation incremental elastic-plastic FEA and flow field oriented nonlinear FEA approaches, such as rigid-plastic FEA and elasto-viscous FEA[1-6]. All those approaches are basically constructed in the frame of small deformation incremental theory. In the 80's, continuum mechanics oriented finite deformation formulation made so much progress that they began to draw most of the attention in the field. A good summary of the developments during this period of time can be found in reference[7]. It is now evident to say that finite deformation elastic-plastic FEA represents the dominating approach in the analysis of metal forming processes.

The application of nonlinear FEA in sheet metal forming has lagged behind the progress in bulk forming. The reason is technical. Structurally, sheet metal parts are always three dimensional and thin shell structured, which make them most naturally represented by shell/membrane elements. However, those elements are challenging in terms of mathematics and numerical implementation, particularly in the case of shell elements. A particular numerical difficulty called element "locking" had puzzled the field for some years (as discussed in Chapter 4). It was observed that structures approximated by shell elements tend to exhibit an extraordinarily stiffer nature than it should be. This phenomenon occurs particularly in the thin shell structures, and is often so severe that the numerical stability is not achievable. Early remedies like "reduced integration" were proven to be not enough to prevent the thin shell element from locking, especially in stamping simulation and analysis, where large deformation and severe boundary constraints are common practices.

Only until late 80's, positive results with potential of general applicability started to be reported[8-13]. Unfortunately, few numerical techniques were fully published. The general view of the problem is that the locking in thin shell elements is basically due to the inability of the elements to represent the deformation patterns where the Kirchhoff condition (i.e. the normal direction fibre of the shell mid-surface remains normal after deformation) should dominate. So the common understanding is to prevent shell elements from locking certain type of Kirchhoff constraint has to be numerically enforced[14].

"Reduced or selectively reduced integration" schemes are helpful by reducing the effects of transverse shear strain components in the deformation energy. However, they also introduce "spurious deformation mode" in the element deformation patterns. Since the spurious deformation modes do not affect the deformation energy in the element, they could be over exaggerated. Therefore, the "hourglass control" mechanism must be implemented in those elements simultaneously. This class of elements are gaining popularity now, because they are often effective, and cheaper in computing cost. Nonetheless, these elements are recommended to be used with caution. A fundamental fact is the theories of reduced integration and hourglass control are only well discussed in terms of regular element shape. For large deformation stamping analysis, element distortion is usual.

Some other techniques such as mixed strain component interpolation are also widely reported and discussed. This type of remedy addresses the fundamental inability of shell elements to represent the Kirchhoff constraints. Since the numerical techniques can only be seen as enhancing the element behaviour in thin shell situations, their success is still not guaranteed.

Due to the situation discussed above, there is still a lack of common recognition of which is the best. The success is not always guaranteed. In this work, a general penalty method for implementing the Kirchhoff constraint directly in shell elements is presented. The method is shown to be successful for three noded and four noded elements in analysing stamping process. Due to the generality of the method, it can be added to any elements with or without combining with other techniques, and therefore provide another choice for achieving the reliability and robustness in analysing stamping processes.

§2 The Outline of Current Work

The contents of this thesis reflect a general effort in the endeavour of exploring and developing the effective FEM tools for metal forming analysis. There are three major parts in this work.

In chapter 2, An unique mathematical derivation of large deformation equations is presented on the basis of a direct linearization of the "future" virtual work equation without using any pseudo stress tensor and corresponding conjugate strain tensor. A major advantage of this derivation is that a clear physical understanding is carried through the whole mathematical process. Therefore distinctive perception on key fundamentals such as: equilibrium equation, strain measure, constitutive relation, stress rotation and residual force evaluation are presented and discussed on a consistent and integrated basis. The code developed in this part of work forms an independent module for 2D bulk forming analysis, while the methodology is carried through the rest of thesis.

A particular effort is described in Chapter 3, which addresses the problem and techniques used in dealing with the frictional contact boundary condition which is common in metal forming processes. A typical ring compression problem is used to show the problem and solution. The algorithm and code developed there is a part of the 2D package.

Chapter 4 presents a full description of a 3D degenerated shell element formulation based on the consistent large deformation formulation presented in Chapter 2. Various aspects of techniques used in shell elements to prevent elements from locking have been reviewed. A special penalty method is devised to enforce the Kirchhoff constraint which has been missing in the degenerated shell element discretization. The method has successfully prevented 3-node and 4-node elements from shear locking in analysing the typical cup drawing process.

At the end of the thesis, a summary of the thesis is presented. Conclusions and recommendations for further work are provided.

§3 References

[1] Marcal, P.V. and King, I.P., *Elasto-plastic analysis of two dimensional stress system by the finite element method,* Inter. J. Mech. Sci., **9** (1967), p143-155.

[2] Yamada, Y., Yoshimura, N. and Sakurai, T., *Plastic stress strain matrix and its application for the solution of elastic-plastic problems by the finite element method,* Inter. J. Mech. Sci., **10** (1967), p343-354.

[3] Zienkiewicz, O.C., Valliappan, S. and King, I.P., *Elastoplastic solutions of engineering problems -- "Initial stress", finite element approach,* Inter. J. Numer. Meths. Engrg., (1969), p75-100.

[4] Lee, C.H. and Kobayashi, S., *New solutions to rigid-plastic deformation problems using a matrix method,* J. Engrg. Ind., Trans. ASME, **7** (1973), p865-873.

[5] Zienkiewicz, O.C. and Godbole, P.N., *Flow of plastic and visco-plastic solids with special reference to extrusion and forming processes,* Inter. J. Numer. Meths. Engrg., **8** (1974), p3-16.

[6] Zienkiewicz, O.C. and Cormeau, I.C., *Visco-plasticity and creep in elastc solids -- A unified numerical solution approach,* Inter. J. Numer. Meths. Engrg., **8** (1974), p821-845.

[7] Rebelo, N., *Review of FE Simulation Methods in Metal Forming,* Proc. Metal Forming Process Simulation in Ind., p7-24, Baden-Baden, Germany, Sept., 1994.

[8] Toh, C.H. and Kobayashi, S., *Deformation Analysis and Blank Design in Square Cup Drawing*, Int. J. Mach. Tool Des. Res., Vol.1, No.1, p15-32, 1985

[9] Nakamachi, E., *A Finite Element Simulation of the Sheet Metal Forming Process*, Int. J. Numer. Meths. Engng., **25** (1988), p283-292.

[10] Nakamachi, E. and Sowerby, R., *Finite Element Modeling of the Punch Stretching of Square Plates*, J. of Applied Mech., Trans. ASME, **55** (1988), p667-671.

[11] Germain, Y., Chung, K. and Wagoner, R.H., *A Rigid-Viscoplastic Finite Element Program for Sheet Metal Forming Analysis*, Int. J. Mech. Sci., **31** (1989), p1-24.

[12] Rebelo, N., Naagtegaal, J.C. and Hibbitt, H.D., *Finite Element Analysis of Sheet Forming Processes*, Int. J. Numer. Meths. Engng, **30** (1990), p1739-1758.

[13] Gelin, J.C., Boulmane, L. and Boisse, P., *Quasi-static implicit and transiant explicit analysis of sheet metal forming using a C^0 three node shell element*, Proc. of the 2nd Int. Conf. NUMISHEET'93, Isehara, Japan, 1993, 53-64

[14] ABAQUS 5.2, Theory Manual, 1994.

CHAPTER 2

A Consistent Large Deformation FEA Formulation

§1 Introduction

An unique mathematical derivation of large deformation equations is presented on the basis of a direct linearization of the "future" virtual work equation without using any pseudo stress tensor and corresponding conjugate strain tensor. A major advantage of this derivation is that a clear physical understanding is carried through the whole mathematical process. Therefore, distinctive perceptions on key fundamentals such as: equilibrium equation, strain measure, constitutive relation, stress rotation and residual force evaluation are presented and discussed on a consistent and integrated basis.

The focus of this chapter is rather on the physical interpretation than on the sophisticated mathematical derivation. Only major steps are briefly listed. Most of the other derivations are available in many continuum mechanics books. Due to the word processing difficulties, there exist two types of tensor and vector notation in the context. Bold character is used in the text to represent tensor/vector, while double/single overlined character is used in equations.

§2 A General View of Nonlinear Large Deformation Problem

Firstly, the fundamentals involved in solving a nonlinear large deformation problem are reviewed.

The primary reasoning behind a large deformation problem does not basically differ from a small deformation problem. When a continuous body is forced to move/deform to a new position (configuration), the following things may occur:

(1) the forced configuration change (described by displacement field) could incur internal deformation in the body and the deformation can be measured by properly defined strain tensor field;
(2) the internal strain field must incur internal stress in a certain way which depends on the nature of the material involved;
(3) only when the internal stress in the body is fully in equilibrium with the external force which causes the body motion, the new configuration can be stablized.

These points represent three fundamentals in any deformation problem: strain measure, constitutive relation and equilibrium equations. The basic simplification made in small deformation analysis is that the motion/deformation of the continuous body is so small that: (1) linear strain measure can be adopted; (2) the increment of stress tensor is only caused by strain increment; (3) the difference between initial configuration and deformed configuration can be ignored. Since none of the assumptions are justifiable in a large deformation situation, nonlinear equations arise.

§3 Incremental Description of Large Deformation Process

In most metal forming processes, nonlinearities will arise in all three fronts mentioned before, plus contact boundary nonlinearity, so that the deformation process has to be described in an incremental way, because only on a smaller incremental scale can linearization be justified. Therefore, three successive configurations: the initial configuration γ^0 (usually unstressed, undeformed), the current configuration γ^t and the future (incremented) configuration $\gamma^{t+\Delta t}$ are usually considered (Figure 2.1).

In an incremental solution process, it is always assumed that all the variables on the current configuration γ^t have been successfully solved in the previous incremental step, therefore the task is simply to obtain the solution on the "future configuration" $\gamma^{t+\Delta t}$ on the basis of the known current solution on γ^t.

§4 Strain Measures

In an incremental solution process, strain measure means two things: one is the choice of a proper strain measure for current strain increment, the other is the selection of a correct way to accumulate strain increments to define the total strain.

Finite strain measure is a matter of choice to some degree. For example, when a tensile specimen is stretched in a multi-stage manner:

$$l_0 \xrightarrow{\Delta l_1} l_1 \xrightarrow{\Delta l_2} l_2 \xrightarrow{\Delta l_3} l_3 \xrightarrow{\Delta l_4} \cdots\ \cdots \xrightarrow{\Delta l_n} l_n$$

a "natural logarithm strain" measure is usually preferred to the "engineering strain" measure. However, the choice of strain measure does influence the constitutive relation when strain and stress have to be co-related later, which after all can only be based on physical evidence, not mathematics.

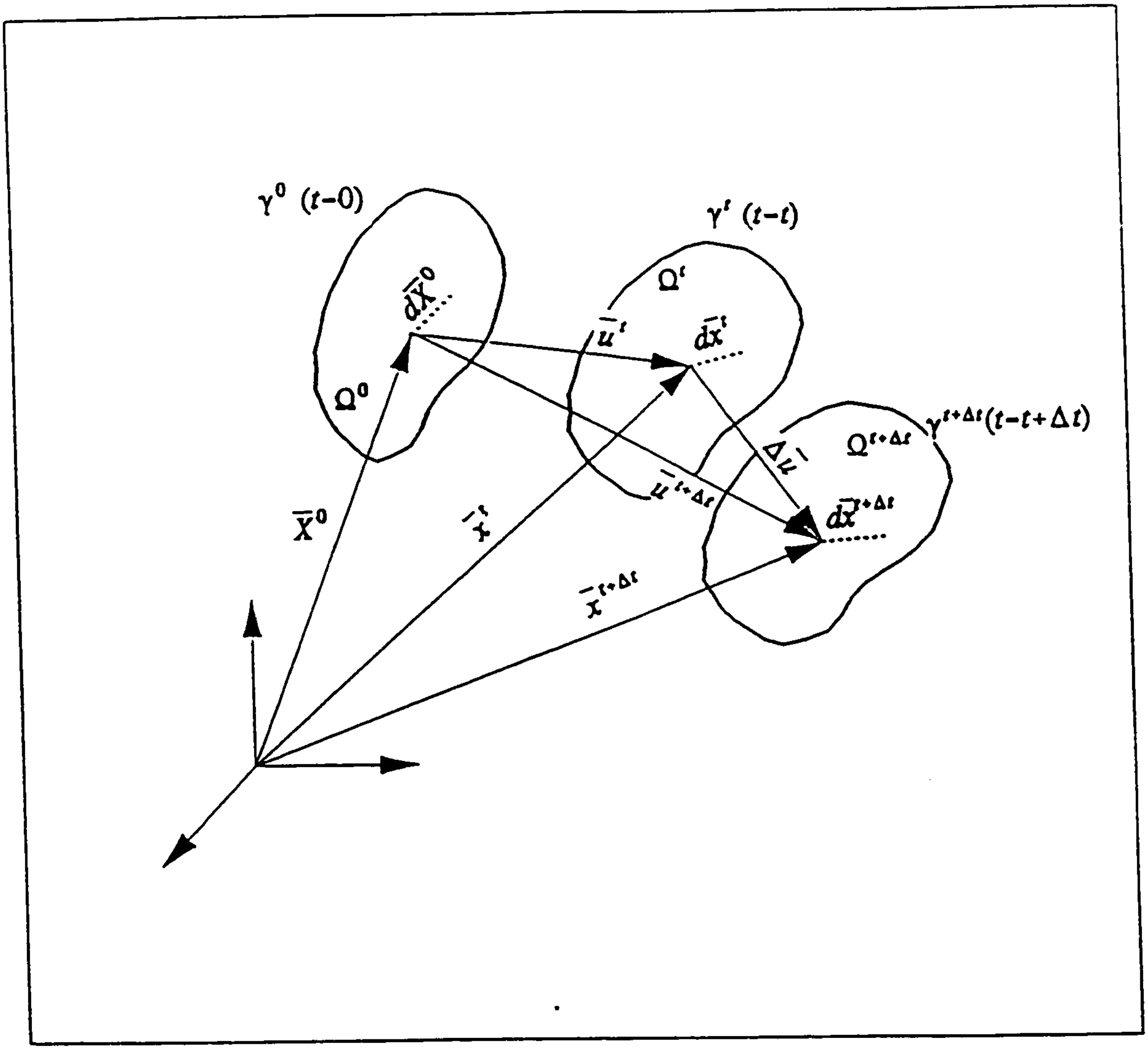

Figure 2.1 The Kinematic Description of a Finite Deformation Process

In the theory of continuum mechanics, the deformation between any two configurations is described by the "deformation gradient tensor **F**" which is defined as

$$\overline{\overline{F}} = \frac{\partial \bar{x}}{\partial \overline{X}} \qquad i.e. \qquad F_{ij} = \frac{\partial x_j}{\partial X_i}$$

Considering the three configurations in Figure 2.1, we have three **F** tensors:

$$\overline{\overline{F}}{}_0^t = \frac{\partial \bar{x}^t}{\partial \overline{X}^0} \qquad \overline{\overline{F}}{}_0^{t+\Delta t} = \frac{\partial \bar{x}^{t+\Delta t}}{\partial \overline{X}^0} \qquad \overline{\overline{F}}{}_t^{t+\Delta t} = \overline{\overline{F}}_t = \frac{\partial \bar{x}^{t+\Delta t}}{\partial \bar{x}^t}$$

which are related by the chain rule as:

$$\overline{\overline{F}}{}_0^{t+\Delta t} = \overline{\overline{F}}{}_0^t \bullet \overline{\overline{F}}_t$$

This relation indicates that if $\mathbf{F}_t$ is interpreted as a deformation description between $\gamma^{t+\Delta t}$ and γ^t, then the deformation gradient **F** is not additive, i.e. $\Delta\mathbf{F} = \mathbf{F}_0^{t+\Delta t} - \mathbf{F}_0^t \neq \mathbf{F}_t$. Therefore, the first choice we have to make is whether we should keep the integrity of $\mathbf{F}_0^{t+\Delta t}$ or simply focus on $\mathbf{F}_t$ as a measure of strain increment in each incremental step and accumulate those increments as the total strain measure. Compared with the case of natural logarithm strain and engineering strain in one dimension situation, $\mathbf{F}_t$ is chosen as the description of incremental deformation and all the calculations are based on the current configuration γ^t.

As a common known fact, $\mathbf{F}_t$ can not be used directly to describe strain, because rigid body motion may also be contained in $\mathbf{F}_t$. To extract the pure deformation portion out of $\mathbf{F}_t$, there are different choices. For example,

small strain tensor

$$\bar{\bar{\varepsilon}}_t = \frac{1}{2}(\bar{\bar{F}}_t + \bar{\bar{F}}_t^T) - \bar{\bar{1}} \tag{1}$$

Green-Lagrangian strain tensor

$$\bar{\bar{E}}_t = \frac{1}{2}(\bar{\bar{F}}_t \bullet \bar{\bar{F}}_t^T - \bar{\bar{1}}) \tag{2}$$

Two polar decompositions of $\mathbf{F}_t$

$$\bar{\bar{F}}_t = \bar{\bar{U}}_t \bullet \bar{\bar{R}}_t = \bar{\bar{R}}_t \bullet \bar{\bar{V}}_t \tag{3}$$

where, $\mathbf{R}_t$ denotes the orthonormal rotation tensor;

$\mathbf{U}_t$ denotes the symmetrical pre-stretch tensor;

$\mathbf{V}_t$ denotes the symmetrical post-stretch tensor;

and, the subscript t indicates the tensors occur and are measured in the current configuration γ^t.

To evaluate those strain measures, We observe an unit cube in Figure 2.2(a) which is initially aligned with the Cartesian axes x_1, x_2, x_3. It is first deformed in simple tension, being extended in the x_1 direction by a small amount e, with strain $-ve$ in x_2 and x_3 directions (Figure 2.2(b)), and then rotated by a small angle α about x_3 (Figure 2.2(c)) and another β

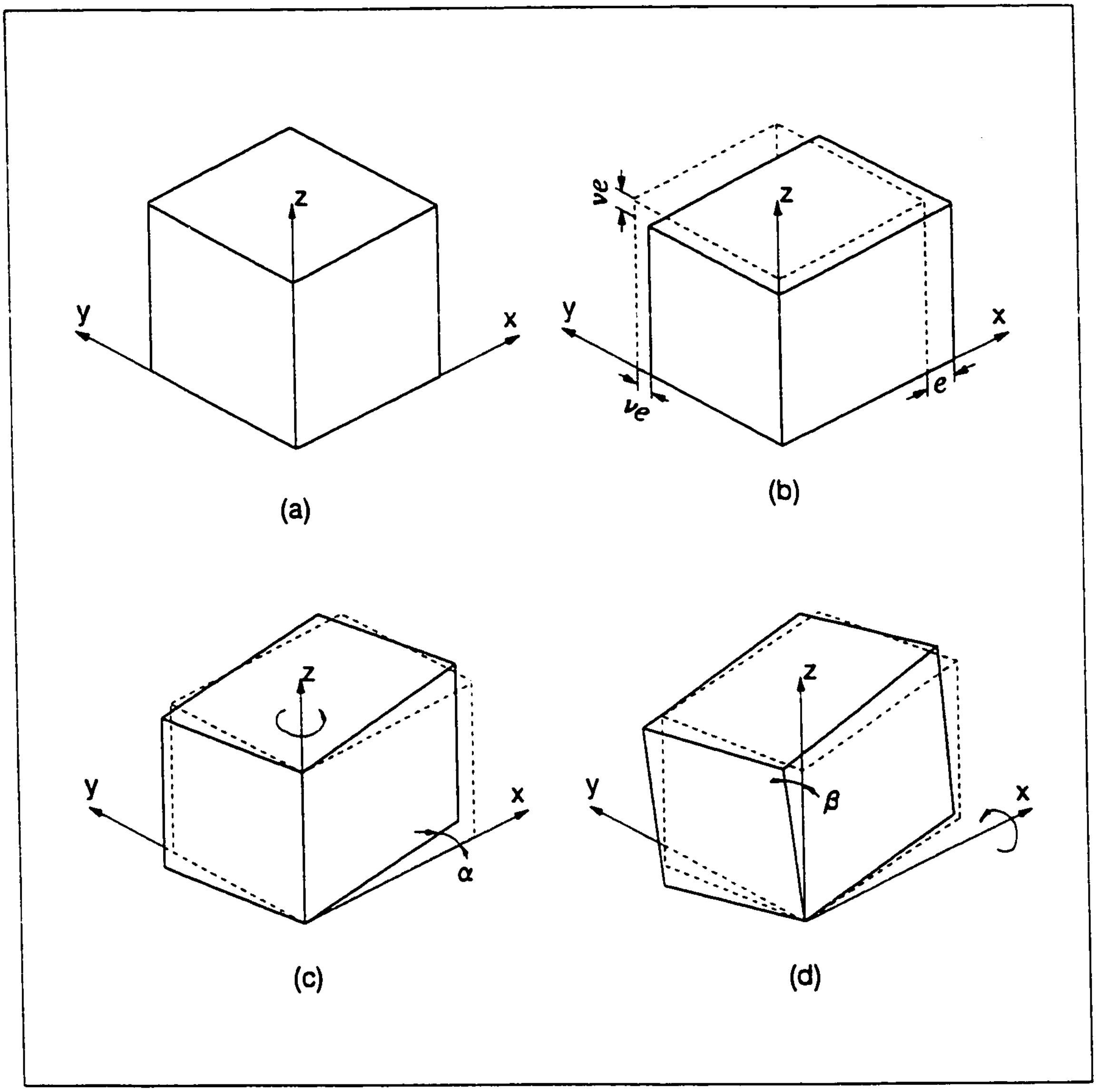

Figure 2.2 Combined Extension and Rotation of Cubic Element

about x_1 (Figure 2.2(d)). The resulting displacement field is as follows

$$
\begin{aligned}
u_1 &= x_1\left[(1+e)\cos\alpha - 1\right] - x_2(1-ve)\sin\alpha \\
u_2 &= x_1(1+e)\sin\alpha\cos\beta + x_2\left[(1-ve)\cos\alpha\sin\beta - 1\right] - x_3(1-ve)\sin\beta \\
u_3 &= x_1(1+e)\sin\alpha\sin\beta + x_2(1-ve)\cos\alpha\sin\beta + x_3\left[(1-ve)\cos\beta - 1\right]
\end{aligned}
$$

Using this displacement field, all the four strains are numerically evaluated according to their definitions in Equ.(1)-(3), and results are tabled (Table 1 & 2).

Table 1 Comparison of Different Strain Measure

	ε_t	E_t	U_t-1	V_t-1
e=0.01, v=0.5 α=2°, β=2°	.009385 .000251 .000615 .000251 -.006212 -.000011 .000615 -.000011 -.005606	.010050 .000000 .000000 .000000 -.004987 .000000 .000000 .000000 -.004987	.010000 .000000 .000000 .000000 -.005000 .000000 .000000 .000000 -.005000	.009982 .000523 .000018 .000523 -.004987 .000001 .000018 .000001 -.005000
e=0.01, v=0.5 α=5°, β=5°	.006157 .000486 .003836 .000486 -.012560 -.000165 .003836 .000165 -.008786	.010050 .000000 .000000 .000000 -.004987 .000000 .000000 .000000 -.004987	.010000 .000000 .000000 .000000 -.005000 .000000 .000000 .000000 -.005000	.009886 .001297 .000114 .001297 -.004887 .000010 .000114 .000010 -.004999
e=0.01, v=0.5 α=10°, β=10°	-.005344 -.000030 .015230 -.000030 -.035000 -.001312 .015230 -.001312 -.020120	.010050 .000000 .000000 .000000 -.004987 .000000 .000000 .000000 -.004987	.010000 .000000 .000000 .000000 -.005000 .000000 .000000 .000000 -.005000	.009548 .002526 .000445 .002526 -.004561 .000077 .000445 .000077 -.004986

Table 2 Comparison between Rotation Tensor $\mathbf{R}_t$ and Spin Tensor ω_t

	$\mathbf{R}_t$	$1+\omega_t$
e=0.01, v=0.5 α=2°, β=2°	.999400 .034880 .001218 -.034900 .998800 .034880 .000000 -.034900 .999400	1.00000 .034980 .000615 -.034980 1.00000 .034710 -.000615 -.034710 1.00000
e=0.01, v=0.5 α=5°, β=5°	.996200 .086820 .007596 -.087160 .992400 .086820 .000000 -.087160 .996200	1.00000 .087210 .003836 -.087210 1.00000 .086550 -.003836 -.086550 1.00000
e=0.01, v=0.5 α=10°, β=10°	.984800 .171000 .030150 -.173600 .969800 .171000 .000000 -.173600 .984800	1.00000 .172800 .015230 -.172800 1.00000 .171500 -.015230 -.171500 1.00000

Viewing the results, it is clear that ($\mathbf{U}_t$-1) and $\mathbf{R}_t$ from polar decomposition provide ideal strain and rotation measure of the real motion at any rotation increment level.

Small strain is the worst because it is very much rotation sensitive. When $\alpha=\beta=5^o$, it is already tremendously erroneous on all components.

$\mathbf{V}_t$ is fundamentally the same tensor as $\mathbf{U}_t$, the difference is simply caused by the frame rotation (notice: $\mathbf{U}_t=\mathbf{R}_t^T\bullet\mathbf{V}_t\bullet\mathbf{R}_t$)

It is worthwhile to mention that Green-Lagrangian strain $\mathbf{E}_t$ also has a steady performance with a reasonable accuracy and rotation insensitivity. The following equations will justify the observation:

$$\bar{\bar{E}}_t = \frac{1}{2}(\bar{\bar{F}}_t\bullet\bar{\bar{F}}_t^T - \bar{\bar{1}}) = \frac{1}{2}\left[(\bar{\bar{U}}_t\bullet\bar{\bar{R}}_t)\bullet(\bar{\bar{R}}_t^T\bullet\bar{\bar{U}}_t) - \bar{\bar{1}}\right]$$

$$= \frac{1}{2}(\bar{\bar{U}}_t\bullet\bar{\bar{U}}_t - \bar{\bar{1}}) = (\bar{\bar{U}}_t - \bar{\bar{1}}) + \frac{1}{2}(\bar{\bar{U}}_t - \bar{\bar{1}})\bullet(\bar{\bar{U}}_t - \bar{\bar{1}}) \approx \bar{\bar{U}}_t - \bar{\bar{1}}$$

Therefore, $\mathbf{E}_t$ is indeed rotation free and can be a reasonable alternative to $\mathbf{U}_t$ in formulation because $\mathbf{U}_t$ is not explicitly expressible.

§5 Useful Relations about Deformation Tensors

To facilitate the mathematical derivation in the next section, we now list the following useful relations. Proofs can be found in various continuum mechanics books[19].

The material time rates of the above tensors at the current instant are given by

$$\frac{d\bar{\bar{F}}_t}{dt} = \bar{\bar{L}} = \frac{\partial \bar{v}}{\partial \bar{x}^t}$$

$$\frac{d\bar{\bar{U}}_t}{dt} = \frac{d\bar{\bar{V}}_t}{dt} = \frac{d\bar{\bar{E}}_t}{dt} = \frac{d\bar{\bar{\varepsilon}}_t}{dt} = \bar{\bar{D}} = \frac{1}{2}(\bar{\bar{L}} + \bar{\bar{L}}^T)$$

$$\frac{d\bar{\bar{R}}_t}{dt} = \bar{\bar{W}} = \frac{1}{2}(\bar{\bar{L}} - \bar{\bar{L}}^T)$$

which can justify the following first order approximations:

$$\bar{\bar{U}}_t \approx \bar{\bar{V}}_t \approx \bar{\bar{1}} + \bar{\bar{D}}\bullet\Delta t = \bar{\bar{1}} + \bar{\bar{\varepsilon}}_t \tag{4a}$$

$$\bar{\bar{R}}_t \approx \bar{\bar{1}} + \bar{\bar{W}}\bullet\Delta t = \bar{\bar{1}} + \bar{\bar{\omega}}_t \tag{4b}$$

$$\bar{\bar{E}}_t \approx \bar{\bar{D}}\bullet\Delta t = \bar{\bar{\varepsilon}}_t \tag{4c}$$

where

$$\varepsilon^t_{ij} = \frac{1}{2}\left(\frac{\partial u_j}{\partial x_i^t} + \frac{\partial u_i}{\partial x_j^t}\right)$$

$$\omega^t_{ij} = \frac{1}{2}\left(\frac{\partial u_j}{\partial x_i^t} - \frac{\partial u_i}{\partial x_j^t}\right)$$

are the well known small strain tensor and spin tensor. Another commomly used tensor in FEM is "displacement gradient tensor" $\mathbf{u}_t$, which is defined as

$$\bar{\bar{u}}_t = \frac{\partial \bar{u}_t}{\partial \bar{x}^t} = \bar{\bar{F}}_t - \bar{\bar{1}} = \bar{\bar{\varepsilon}}_t + \bar{\bar{\omega}}_t$$

Therefore

$$\bar{\bar{F}}_t = \bar{\bar{1}} + \bar{\bar{u}}_t = \bar{\bar{1}} + \bar{\bar{\varepsilon}}_t + \bar{\bar{\omega}}_t$$

Without losing the first order accuracy, it is easy to demonstrate that

$$\bar{\bar{F}}_t^{-1} = \frac{\partial \bar{x}^t}{\partial \bar{x}^{t+\Delta t}} \approx \bar{\bar{1}} - \bar{\bar{u}}_t = \bar{\bar{1}} - \bar{\bar{\varepsilon}}_t - \bar{\bar{\omega}}_t$$

§6 Equilibrium

§6-1. Field Equations and Virtual Work Principle

At any moment of the deformation process, the stress field is governed by the following equilibrium equations:

$$\begin{aligned} \sigma_{ij,j} + \rho b_i &= 0 && in\ \ \Omega \\ \sigma_{ij} n_j &= \bar{t}_i && on\ \ \Gamma_F \\ u_i &= \bar{u}_i && on\ \ \Gamma_D \end{aligned} \qquad (5)$$

where

σ_{ij} is the Cauchy (true) stress tensor in the deformed configuration Ω;

ρ is the mass density in the body;

b_i is the body force vector which can include the acceleration term;

u_i is the displacement vector which is specified by a given vector function u_i on the surface portion Γ_D;

t_i is the traction vector function prescribed on the surface Γ_F with an unit normal vector n_i.

Due to the difficulties in directly solving the field equations, the virtual work principle is usually adopted in finite element formulation, which states the same boundary value problem in an integral form:

$$\int_{\Omega} \bar{\bar{\sigma}} : \delta\bar{\bar{\varepsilon}} \, d\Omega = \int_{\Omega} \rho \bar{b} \bullet \delta\bar{u} \, d\Omega + \int_{\Gamma_F} \bar{t} \bullet \delta\bar{u} \, d\Gamma \tag{6a}$$

or,

$$\int_{\Omega} \sigma_{ij} \delta\varepsilon_{ij} \, d\Omega = \int_{\Omega} \rho b_i \delta u_i \, d\Omega + \int_{\Gamma_F} t_i \delta u_i \, d\Gamma \tag{6b}$$

Again, σ_{ij}, b_i, t_i, Ω and Γ_F remain the same definition as in the field equations. δu_i is an arbitrary kinematically admissible virtual displacement field which is assumed that (i) infinitesimally small; (ii) superimposed on the configuration Ω where the equilibrium is established. Therefore:

$$\delta\varepsilon_{ij} = \frac{1}{2}\left(\frac{\partial(\delta u_i)}{\partial x_j} + \frac{\partial(\delta u_j)}{\partial x_i}\right) \qquad in \quad \Omega$$

$$\delta u_i = 0 \qquad on \quad \Gamma_D$$

It is necessary to emphasize the facts that:

(1) virtual work equation (6) is exactly a mathematical equivalence of the field equation set (5), should δu_i have indeed included all the possible virtual displacement fields which are kinematically admissible.

(2) the virtual work equation (6) is instantaneous, for example, to obtain the equilibrium stress state in $\gamma^{t+\Delta t}$, the virtual work equation must be:

$$\begin{aligned}&\int_{\Omega^{t+\Delta t}} \sigma_{ij}^{t+\Delta t}\,\delta\varepsilon_{ij}^{t+\Delta t}\,d\Omega^{t+\Delta t} \\ &= \int_{\Omega^{t+\Delta t}} \rho^{t+\Delta t} b_i^{t+\Delta t}\,\delta u_i^{t+\Delta t}\,d\Omega^{t+\Delta t} + \int_{\Gamma_F^{t+\Delta t}} t_i^{t+\Delta t}\,\delta u_i^{t+\Delta t}\,d\Gamma_F^{t+\Delta t}\end{aligned} \tag{7}$$

in which all the variables and integrations occur on $\gamma^{t+\Delta t}$. For example,

$$\delta\varepsilon_{ij}^{t+\Delta t} = \frac{1}{2}\left(\frac{\partial(\delta u_i)}{\partial x_j^{t+\Delta t}} + \frac{\partial(\delta u_j)}{\partial x_i^{t+\Delta t}}\right)$$

This imposes a difficulty because $\gamma^{t+\Delta t}$ is not a known configuration *a priori*. This is where the geometrical nonlinearity begins, because we have to build up a linearized approximation of equation (7) on the known configuration γ^t.

(3) equilibrium discussion here is totally independent of any particular strain measure and constitutive relation. Therefore, stress solutions which come out of the virtual work equation could only be an equilibrium solution, but not necessarily the true solution. The true solution can be obtained only if the correct strain measure and constitutive relation have been implemented simultaneously.

§6-2 Incremental form of the virtual work principle

As has been mentioned, virtual work principle is instantaneous. Therefore, at the current moment, we have:

$$\int_{\Omega^t} \overline{\overline{\sigma}}^t : \delta\overline{\overline{\varepsilon}}^t \, d\Omega^t = \int_{\Omega^t} \rho^t \, \overline{b}^t \bullet \delta\overline{u}^t \, d\Omega^t + \int_{\Gamma_F^t} \overline{t}^t \bullet \delta\overline{u}^t \, d\Gamma^t$$

at the next incremented moment t+Δt, we have:

$$\int_{\Omega^{t+\Delta t}} \overline{\overline{\sigma}}^{t+\Delta t} : \delta\overline{\overline{\varepsilon}}^{t+\Delta t} d\Omega^{t+\Delta t} = \int_{\Omega^{t+\Delta t}} \rho^{t+\Delta t} \overline{b}^{t+\Delta t} \bullet \delta\overline{u}^{t+\Delta t} d\Omega^{t+\Delta t} + \int_{\Gamma_F^{t+\Delta t}} \overline{t}^{t+\Delta t} \bullet \delta\overline{u}^{t+\Delta t} d\Gamma^{t+\Delta t}$$

However, the two equations can not be compared directly, because the descriptions are based on two different configurations γ^t and $\gamma^{t+\Delta t}$ respectively. Following transformations have to be made *a priori*.

As will be found out later, the major terms in the incremental equation come from the transformation of the virtual internal work term

$$\int_{\Omega^{t+\Delta t}} \overline{\overline{\sigma}}^{t+\Delta t} : \delta\overline{\overline{\varepsilon}}^{t+\Delta t} \, d\Omega^{t+\Delta t}$$

So this term is worked on first:

(1) Transform the integration from $\gamma^{t+\Delta t}$ to γ^{t} :

$$\int_{\Omega^{t+\Delta t}} \overline{\overline{\sigma}}^{t+\Delta t} : \delta\overline{\overline{\varepsilon}}^{t+\Delta t} d\Omega^{t+\Delta t} = \int_{\Omega^{t}} \overline{\overline{\sigma}}^{t+\Delta t} : \delta\overline{\overline{\varepsilon}}^{t+\Delta t} \frac{\rho^{t}}{\rho^{t+\Delta t}} d\Omega^{t} \approx \int_{\Omega^{t}} \overline{\overline{\sigma}}^{t+\Delta t} : \delta\overline{\overline{\varepsilon}}^{t+\Delta t} d\Omega^{t}$$

where $\rho^{t} \approx \rho^{t+\Delta t}$ due to the material incompressibility of the metal forming process.

(2) Since σ^{t} and $\sigma^{t+\Delta t}$ are the Cauchy true stress tensors of the same material point at time t and t+Δt respectively, it is perceivable (as shown in Figure 2.3) that the change between σ^{t} and $\sigma^{t+\Delta t}$ are twofold: one is stress increment caused by deformation (strain) at the material point, the other is the stress rotation caused by the rigid body motion at the point. Therefore, the process can be viewed as follows:

$$\overline{\overline{\sigma}}^{t} \xrightarrow{\overline{\overline{U}}_t} (\overline{\overline{\sigma}}^{t} + \Delta\overline{\overline{\sigma}}^{*}) \xrightarrow{\overline{\overline{R}}_t} \overline{\overline{R}}_t^{T} \bullet (\overline{\overline{\sigma}}^{t} + \Delta\overline{\overline{\sigma}}^{*}) \bullet \overline{\overline{R}}_t = \overline{\overline{\sigma}}^{t+\Delta t}$$

where $\Delta\sigma^{*}$ is the stress increment caused by U_t, assuming no rigid body rotation, and therefore should be the stress increment determined by constitutive equation.

Using $\mathbf{R}_t \approx \mathbf{1} + \omega_t$ and $\mathbf{R}_t^{T} \approx \mathbf{1} - \omega_t$ and neglecting any higher than first order terms about $\Delta\sigma^{*}$ and ω_t, it is straightforward to have

$$\bar{\bar{\sigma}}^{t+\Delta t} = (\bar{\bar{1}} - \bar{\bar{\omega}}_t)\bullet(\bar{\bar{\sigma}}^t + \Delta\bar{\bar{\sigma}}^{\bullet})\bullet(\bar{\bar{1}} + \bar{\bar{\omega}}_t)$$

$$\approx \bar{\bar{\sigma}}^t + \Delta\bar{\bar{\sigma}}^{\bullet} - \bar{\bar{\omega}}_t\bullet\bar{\bar{\sigma}}^t + \bar{\bar{\sigma}}^t\bullet\bar{\bar{\omega}}_t$$

or

$$\Delta\bar{\bar{\sigma}} = \bar{\bar{\sigma}}^{t+\Delta t} - \bar{\bar{\sigma}}^t \approx \Delta\bar{\bar{\sigma}}^{\bullet} - \bar{\bar{\omega}}_t\bullet\bar{\bar{\sigma}}^t + \bar{\bar{\sigma}}^t\bullet\bar{\bar{\omega}}_t$$

(3) Then, using chain rule, we have

$$\delta\bar{\bar{u}}^{t+\Delta t} = \frac{\partial(\delta\bar{u})}{\partial\bar{x}^{t+\Delta t}} = \frac{\partial\bar{x}^t}{\partial\bar{x}^{t+\Delta t}}\bullet\frac{\partial(\delta\bar{u})}{\partial\bar{x}^t} = \bar{\bar{F}}_t^{-1}\bullet\delta\bar{\bar{u}}^t \approx (\bar{\bar{1}} - \bar{\bar{u}}_t)\bullet\delta\bar{\bar{u}}_t$$

(4) Therefore

$$\begin{aligned}
\bar{\bar{\sigma}}^{t+\Delta t} : \delta\bar{\bar{\varepsilon}}^{t+\Delta t} &= \bar{\bar{\sigma}}^{t+\Delta t} : (\delta\bar{\bar{u}}^{t+\Delta t})^T \\
&\approx (\bar{\bar{\sigma}}^t + \Delta\bar{\bar{\sigma}}^{\bullet} - \bar{\bar{\omega}}_t\bullet\bar{\bar{\sigma}}^t + \bar{\bar{\sigma}}^t\bullet\bar{\bar{\omega}}_t):[(\bar{\bar{1}} - \bar{\bar{u}}_t)\bullet\delta\bar{\bar{u}}^t]^T \\
&= [(\bar{\bar{\sigma}}^t + \Delta\bar{\bar{\sigma}}^{\bullet} - \bar{\bar{\omega}}_t\bullet\bar{\bar{\sigma}}^t + \bar{\bar{\sigma}}^t\bullet\bar{\bar{\omega}}_t)\bullet(\bar{\bar{1}} - \bar{\bar{u}}_t)]:(\delta\bar{\bar{u}}^t)^T \\
&\approx (\bar{\bar{\sigma}}^t + \Delta\bar{\bar{\sigma}}^{\bullet} - \bar{\bar{\sigma}}^t\bullet\bar{\bar{\varepsilon}}_t - \bar{\bar{\varepsilon}}_t\bullet\bar{\bar{\sigma}}^t + \bar{\bar{u}}_t^T\bullet\bar{\bar{\sigma}}^t):(\delta\bar{\bar{u}}^t)^T \\
&= \bar{\bar{\sigma}}^t:\delta\bar{\bar{\varepsilon}}^t + \Delta\bar{\bar{\sigma}}^{\bullet}:\delta\bar{\bar{\varepsilon}}^t - (\bar{\bar{\sigma}}^t\bullet\bar{\bar{\varepsilon}}_t + \bar{\bar{\varepsilon}}_t\bullet\bar{\bar{\sigma}}^t):\delta\bar{\bar{\varepsilon}}^t + (\bar{\bar{\sigma}}^t\bullet\bar{\bar{u}}_t):\delta\bar{\bar{u}}^t \\
&= \bar{\bar{\sigma}}^t:\delta\bar{\bar{\varepsilon}}^t + \Delta\bar{\bar{\sigma}}^{\bullet}:\delta\bar{\bar{\varepsilon}}^t - 2(\bar{\bar{\varepsilon}}_t\bullet\bar{\bar{\sigma}}^t):\delta\bar{\bar{\varepsilon}}^t + (\bar{\bar{\sigma}}^t\bullet\bar{\bar{u}}_t):\delta\bar{\bar{u}}^t
\end{aligned}$$

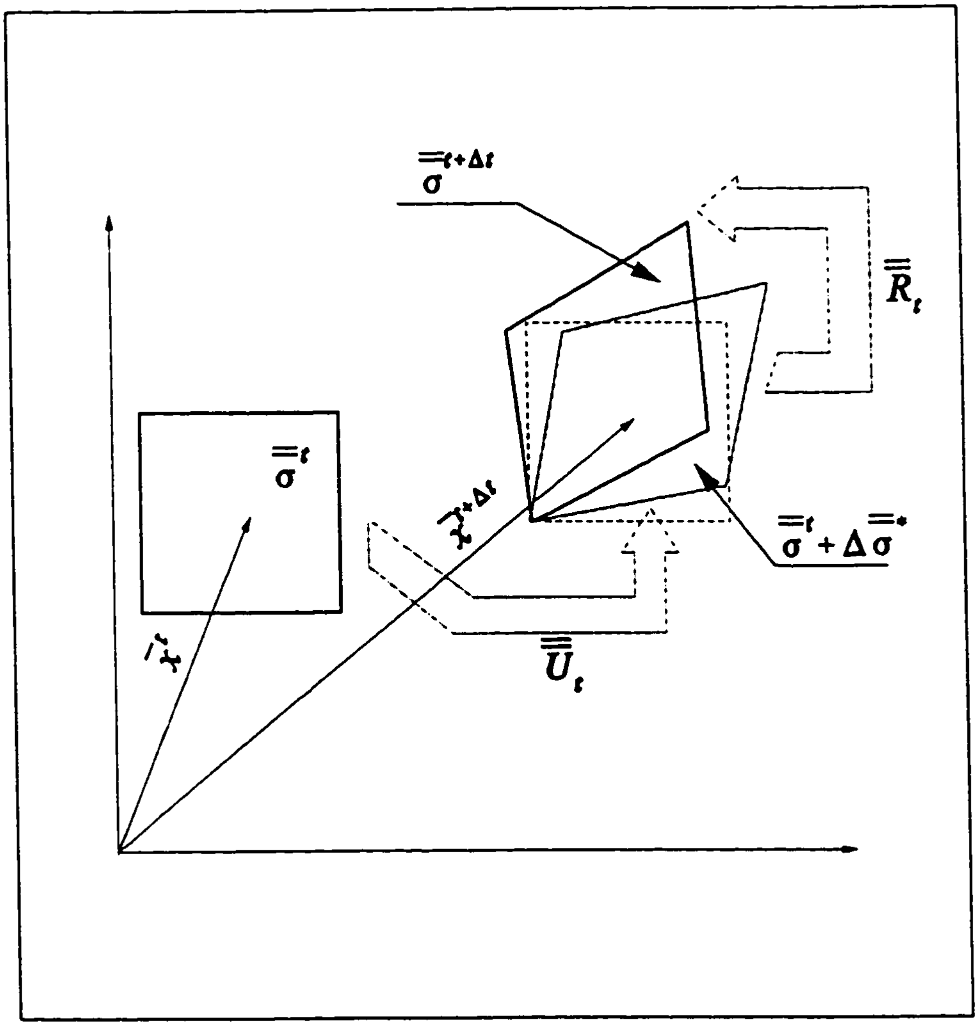

Figure 2.3 Stress Increment with Finite Rigid Body Rotation

where following mathematical identities have been used:

$$\overline{\overline{A}}:\overline{\overline{B}} = \overline{\overline{A}}^T:\overline{\overline{B}}^T = (\overline{\overline{A}}^T\bullet\overline{\overline{B}}):\overline{\overline{1}} = (\overline{\overline{A}}\bullet\overline{\overline{B}}^T):\overline{\overline{1}}, \quad and \quad (\overline{\overline{A}}\bullet\overline{\overline{B}})\bullet\overline{\overline{C}} = \overline{\overline{A}}\bullet(\overline{\overline{B}}\bullet\overline{\overline{C}})$$

Thus

$$\begin{aligned} &\int_{\Omega^{t+\Delta t}} \overline{\overline{\sigma}}^{t+\Delta t}:\delta\overline{\overline{\varepsilon}}^{t+\Delta t} d\Omega^{t+\Delta t} - \int_{\Omega^t} \overline{\overline{\sigma}}^t:\delta\overline{\overline{\varepsilon}}^t d\Omega^t \\ &= \int_{\Omega^t} \left[\Delta\overline{\overline{\sigma}}^{\bullet}:\delta\overline{\overline{\varepsilon}}^t - 2(\overline{\overline{\varepsilon}}_t\bullet\overline{\overline{\sigma}}^t):\delta\overline{\overline{\varepsilon}}^t + (\overline{\overline{\sigma}}^t\bullet\overline{\overline{u}}_t):\delta\overline{\overline{u}}^t\right] d\Omega^t \end{aligned} \tag{8}$$

Working on the other terms, we have

(1) body force term:

$$\begin{aligned} \int_{\Omega^{t+\Delta t}} \rho^{t+\Delta t}\overline{b}^{t+\Delta t}\bullet\delta\overline{u}^{t+\Delta t}\, d\Omega^{t+\Delta t} &= \int_{\Omega^t} \rho^{t+\Delta t}\overline{b}^{t+\Delta t}\bullet\delta\overline{u}^{t+\Delta t}\frac{\rho^t}{\rho^{t+\Delta t}}\, d\Omega^t \\ = \int_{\Omega^t} \rho^t\overline{b}^{t+\Delta t}\bullet\delta\overline{u}^{t+\Delta t}\, d\Omega^t &= \int_{\Omega^t} \rho^t\overline{b}^{t+\Delta t}\bullet\delta\overline{u}^t\, d\Omega^t \end{aligned}$$

because both of $\delta u^{t+\Delta t}$ and δu^t are arbitrary virtual displacement field. Then, we have

$$\int_{\Omega^{t+\Delta t}} \rho^{t+\Delta t}\overline{b}^{t+\Delta t}\bullet\delta\overline{u}^{t+\Delta t} d\Omega^{t+\Delta t} - \int_{\Omega^t} \rho^t\overline{b}^t\bullet\delta\overline{u}^t d\Omega^t = \int_{\Omega^t} \rho^t\Delta\overline{b}^t\bullet\delta\overline{u}^t d\Omega^t \tag{9}$$

where $\Delta\mathbf{b}=\mathbf{b}^{t+\Delta t}-\mathbf{b}^t$ is the increment of the body force density.

(2) surface traction force term: noting $\|\mathbf{F}_t\|=\rho^t/\rho^{t+\Delta t}\approx 1$, $\mathbf{F}_t^{-1}\approx\mathbf{1}-\mathbf{u}_t$, and $\delta\mathbf{u}^{t+\Delta t}=\delta\mathbf{u}^t$

$$\int_{\Gamma_F^{t+\Delta t}} \bar{t}^{t+\Delta t}\bullet\delta\bar{u}^{t+\Delta t}\,d\Gamma_F^{t+\Delta t} = \int_{\Gamma_F^{t+\Delta t}} (d\Gamma_F^{t+\Delta t}\,\bar{n}^{t+\Delta t})\bullet\bar{\bar{\sigma}}^{t+\Delta t}\bullet\delta\bar{u}^{t+\Delta t}$$

$$= \int_{\Gamma_F^t} (d\Gamma_F^t\,\bar{n}^t)\bullet(\|\bar{\bar{F}}_t\|\,\bar{\bar{F}}_t^{-1})\bullet\bar{\bar{\sigma}}^{t+\Delta t}\bullet\delta\bar{u}^t$$

where $\mathbf{t}_o^{t+\Delta t}=\mathbf{n}^t\bullet\sigma^{t+\Delta t}$ is the total surface force at time t+Δt, but exerted on the current configuration γ^t. Therefore, we have:

$$\begin{aligned}&\int_{\Gamma_F^{t+\Delta t}} \bar{t}^{t+\Delta t}\bullet\delta\bar{u}^{t+\Delta t}\,d\Gamma_F^{t+\Delta t} - \int_{\Gamma_F^t}\bar{t}^t\bullet\delta\bar{u}^t\,d\Gamma_F^t\\ &= \int_{\Gamma_F^t}\Delta\bar{t}\bullet\delta\bar{u}^t\,d\Gamma_F^t - \int_{\Gamma_F^t}\bar{n}^t\bullet(\bar{\bar{u}}_t\bullet\bar{\bar{\sigma}}^t)\bullet\delta\bar{u}^t\,d\Gamma_F^t\end{aligned} \tag{10}$$

Where $\Delta\mathbf{t}=\mathbf{n}^t\bullet\Delta\sigma$ is the surface force increment acting on the current configuration γ^t

(3) Putting equations (8), (9) and (10) together yields the linearized incremental form of the equilibrium equation (11):

$$\begin{aligned}&\int_{\Omega^t}\left[(\Delta\bar{\bar{\sigma}}^{*}-2\bar{\bar{\varepsilon}}_t\bullet\bar{\bar{\sigma}}^t):\delta\bar{\bar{\varepsilon}}^t+(\bar{\bar{\sigma}}^t\bullet\bar{\bar{u}}_t):\delta\bar{\bar{u}}^t\right]d\Omega^t+\int_{\Gamma_F^t}\bar{n}^t\bullet(\bar{\bar{u}}_t\bullet\bar{\bar{\sigma}}^t)\bullet\delta\bar{u}^t\,d\Gamma_F^t\\ &= \int_{\Omega^t}\rho^t\Delta\bar{b}\bullet\delta\bar{u}^t\,d\Omega^t+\int_{\Gamma_F^t}\Delta\bar{t}\bullet\delta\bar{u}^t\,d\Gamma_F^t\end{aligned} \tag{11}$$

which is fully described in the known current configuration γ^t, and therefore can be numerically formulated. The first integral term on the left hand side coincides with the well accepted updated Lagrangian formulation by McMeeking and Rice[1], but is derived from a totally different perspective. And the second term has not appeared in their work.

It should be recognized that:

(1) equation (11) is mathematically a first order approximation of equation (7), which is no more than a statement of the stress equilibrium at time $t+\Delta t$.

(2) although it is mathematically true that $\mathbf{S}^{t+\Delta t}:\delta\mathbf{E}^{t+\Delta t}=\sigma^{t+\Delta t}:\delta\varepsilon^{t+\Delta t}$, where $\mathbf{S}^{t+\Delta t}$ stands for the second Piola-Kirchhoff stress tensor and $\delta\mathbf{E}^{t+\Delta t}$ for the variation in Green-Lagrangian strain tensor, that does not necessarily suggest we have to use $\mathbf{S}^{t+\Delta t}$ and $\mathbf{E}^{t+\Delta t}$ as a pair in constitutive relation.

(3) as will be discussed later in §10, the real purpose of using equ.(11) is to formulate a best possible tangential stiffness matrix. However, considering the commonly used Newton-Raphson solution scheme, sacrifice has to be made to achieve the best numerical efficiency. So, flexibility is allowed in the numerical implementation equation (11).

§7 Constitutive Relationship

As it is believed that equilibrium and constitutive relation should be discussed independently, one of major efforts in §6 is to avoid using "virtual stress" and its "conjugate strain". The benefits here are not only simplified mathematical expressions, but more importantly a better physical vision of the discussion. In order to extend the common sense one dimensional stress-strain relation established in tensile test to three dimensional situations, solid physical definitions of both strain and stress are of importance.

It has been a common understanding that the plastic deformation is incremental and history-dependent, therefore the strain-rate-oriented flow theories are most popular. For metal deformation, Prandtl-Reuss flow rule is still dominant:

$$d\varepsilon_{ij} = \sigma'_{ij} d\lambda + \frac{1}{2G} d\sigma'_{ij} + \frac{1-2\nu}{E} \delta_{ij} d\sigma_{kk} \qquad (12)$$

In R. Hill's book[2], $d\varepsilon_{ij}$ is defined in terms of "natural strain increment", which coincides with small strain description. Referring to equ.(4), this equation does not contradict with any of the strain measures discussed in §4, should the increment be kept infinitesimally small.

For finite deformation increment, we have to argue that only the strain measure which physically makes sense should be used to replace $d\varepsilon_{ij}$ in equ.(12). Therefore, as discussed in §4, the ideal candidate is $\mathbf{U}_t$-1. However, since $\mathbf{U}_t$ has no explicit expression, it can hardly be formulated. Pillinger and Hartlay *at el*[3] suggested using "LCR increment of strain". It seems also a straightforward choice to use Green-Lagrangian strain $\mathbf{E}_t$ in formulating stiffness matrix, but come back to $\mathbf{U}_t$ to evaluate the real stress increment during residual force calculation of Newton-Raphson iterations, which will be further discussed in §10.

In the case of using $\Delta\sigma^*$ and $\mathbf{E}_t$, constitutive relation may be expressed as

$$\Delta\sigma^*_{ij} = D^{ep}_{ijkl} E^t_{ij}$$

where D^{ep}_{ijkl} is the elastic-plastic matrix of tangent modulus, which depends on the current stress and loading history. For Prandtl-Reuss materials, D^{ep}_{ijkl} stands for the well-known Yamada elastic-plastic matrix[4].

Again, it should be emphasized that the Prandtl-Reuss equation is in an instantaneous rate form, which means $\{d\varepsilon\}$ and $\{d\sigma\}$ have to be infinitesimally small and $[D^{ep}]$ should be referred to the stress state which is just before $\{d\varepsilon\}$ and $\{d\sigma\}$ occur. But, in the finite element formulation, the finite increment $\{\Delta\varepsilon\}$ and $\{\Delta\sigma\}$ must be implemented. This is not a problem when the objective is just to seek a linearized equation and defining the tangential stiffness matrix. However, in residual force calculation when the goal becomes to evaluate the true stress increment $\{\Delta\sigma\}$ based on the obtained strain increment $\{\Delta\varepsilon\}$, it does incur errors. Thus, a proper integration algorithm must be used to reduce such errors. The detail will be discussed in §9.

§8 Finite Element Equations

Here, finite element equations that follow from Equ.(11) are being derived. Before proceeding, a notation change is made. Instead of writing the displacement gradient tensor occurring between configuration γ^t and $\gamma^{t+\Delta t}$ as $\mathbf{u}_t$, $\Delta\mathbf{u}$ is used to emphasize the incremental nature of this deformation. The subscript t is no longer used because here the focus is on the updated Lagrangian description so that the reference configuration is defaulted as γ^t. Similarly, ε_t, $\mathbf{E}_t$, $\mathbf{U}_t$, $\mathbf{R}_t$, and ω_t are replaced by $\Delta\varepsilon$, $\Delta\mathbf{E}$, $\Delta\mathbf{U}$, $\Delta\mathbf{R}$, and $\Delta\omega$ respectively.

In finite element formulations, the continuous body is discretized into finite elements. On each single element, the displacement field, body force field and surface traction force distribution are interpolated by a known function whose form depends on the type of element used. The matrix form of these interpolations are as follows:

$$\{\Delta u\}^{(e)} = [N]\{\Delta \tilde{u}\}^{(e)}$$

$$\{\delta u\}^{(e)} = [N]\{\delta \tilde{u}\}^{(e)}$$

$$\{\Delta b\}^{(e)} = [N]\{\Delta \tilde{b}\}^{(e)}$$

$$\{\Delta t\}^{(e)} = [N]\{\Delta \tilde{t}\}^{(e)}$$

where, [N] is the shape function matrix;

$\{\Delta u\}^{(e)}$ is the vector of the displacement increment over the element.

$\{\Delta \tilde{u}\}^{(e)}$ is the vector of the displacement increments at the nodal points associated with the element;

similarly, $\{\delta u\}^{(e)}$, $\{\Delta b\}^{(e)}$, and $\{\Delta t\}^{(e)}$ are vector functions defined over the element, and $\{\delta \tilde{u}\}^{(e)}$, $\{\Delta \tilde{b}\}^{(e)}$, and $\{\Delta \tilde{t}\}^{(e)}$ are the corresponding nodal value vectors respectively.

Based on the displacement interpolation, the following strain expressions can be given:

$$\{\delta \varepsilon\}^{(e)} = [B_o]^{(e)}\{\delta \tilde{u}\}^{(e)}$$

$$\{\Delta \varepsilon\}^{(e)} = [B_o]^{(e)}\{\Delta \tilde{u}\}^{(e)}$$

$$\{\Delta E\}^{(e)} = [\overline{B}]^{(e)}\{\Delta \tilde{u}\}^{(e)}$$

$$\{\theta\}^{(e)} = [G]^{(e)}\{\Delta\bar{u}\}^{(e)}$$

where, $\{\delta\varepsilon\}^{(e)}$ is the vector form of the virtual small strain tensor over the element.

$\{\Delta\varepsilon\}^{(e)}$ is the vector form of the small strain increment tensor over the element;

$\{\Delta E\}^{(e)}$ is the vector form of the Green-Lagrangian strain increment tensor over the element;

$\{\theta\}^{(e)}$ is the vector form of the displacement gradient increment tensor $\Delta u_{j,i}$ over the element;

$[B_o]^{(e)}$ is the conventional small strain matrix which relates the nodal displacement increment to the small strain tensor over the element;

$[B]^{(e)}$ is the nonlinear Green-Lagrangian strain matrix which relates the nodal displacement increment to Green-Lagrangian strain tensor over the element ($[B]^{(e)}=[B_o]^{(e)}+[B_L]^{(e)}$);

$[G]^{(e)}$ is the displacement gradient matrix which relates the nodal displacement increment to the displacement gradient increment tensor over the element;

Following these notation conventions, the incremental equilibrium equation (11) can be transformed into the matrix equation

$$\{\delta\bar{u}\}^{(e)T}\left([K_o]^{(e)} + [K_\varepsilon]^{(e)} + [K_u]^{(e)} + [K_t]^{(e)}\right)\{\Delta\bar{u}\}^{(e)} = \{\delta\bar{u}\}^{(e)T}\{\Delta R\}^{(e)} \qquad (13)$$

where, $[K_o]$ is derived from term $\Delta\sigma^*:\delta\varepsilon$. If $\Delta\sigma^*_{ij} = D^{ep}_{ijkl}\,\Delta\varepsilon_{kl}$ is assumed, it is the conventional small strain stiffness matrix, i.e.

$$\left[K_o\right]^{(e)} = \int_{\Omega^{(e)t}} \left[B_o\right]^{(e)T} \left[D_{ep}\right]^{(e)} \left[B_o\right]^{(e)} \, d\Omega^{(e)t}$$

Or, when $\Delta\sigma^*_{ij} = D^{ep}_{ijkl}\Delta E_{kl}$ is used,

$$\left[K_o\right]^{(e)} = \int_{\Omega^{(e)t}} \left[B_o\right]^{(e)T} \left[D_{ep}\right]^{(e)} \left[\overline{B}\right]^{(e)} \, d\Omega^{(e)t}$$

In this case, the matrix is not symmetrical, so a compromise can be made by replacing $\delta\varepsilon$ with δE in $\Delta\sigma^*:\delta\varepsilon$, then

$$\left[K_o\right]^{(e)} = \int_{\Omega^{(e)t}} \left[\overline{B}\right]^{(e)T} \left[D_{ep}\right]^{(e)} \left[\overline{B}\right]^{(e)} \, d\Omega^{(e)t}$$

$[K_\varepsilon]$ is from term $2(\Delta\varepsilon \bullet \sigma^t):\delta\varepsilon^t$,

$$\left[K_\varepsilon\right]^{(e)} = \int_{\Omega^{(e)t}} \left[B_o\right]^{(e)T} \left[S\right]^{(e)} \left[B_o\right]^{(e)} \, d\Omega^{(e)t}$$

$[K_u]$ is from term $(\sigma^t \bullet \Delta\mathbf{u}):\delta\mathbf{u}^t$,

$$\left[K_u\right]^{(e)} = \int_{\Omega^{(e)t}} \left[G\right]^{(e)T} \left[T\right]^{(e)} \left[G\right]^{(e)} \, d\Omega^{(e)t}$$

The details of [S] and [T] matrice can be found in Appendix 1.

$[K_t]$ is from the stress boundary integration term,

$$[K_t]^{(e)} = \int_{\Gamma_F^{(e)t}} [H]^{(e)T} [S_t]^{(e)} [G]^{(e)} \, d\Gamma_F^{(e)t}$$

The derivation of [H] and $[S_t]$ is also detailed in Appendix 1. Since $[K_t]$ is not symmetrical, it is often an optional term.

Adding those terms together yield the element stiffness matrix.

$$[K]^{(e)} = [K_o]^{(e)} + [K_\varepsilon]^{(e)} + [K_u]^{(e)} + [K_t]^{(e)} \tag{14}$$

And

$$\{\Delta R\}^{(e)} = \int_{\Omega^{(e)t}} \rho \, [N]^T [N] \{\Delta \bar{b}\}^{(e)} d\Omega^{(e)t} + \int_{\Gamma_F^{(e)t}} [N]^T [N] \{\Delta \bar{t}\}^{(e)} d\Gamma_F^{(e)t} \tag{15}$$

is the conventional equivalent element nodal force increment vector.

Because $\{\delta u\}^{(e)}$ is the arbitrary virtual nodal displacement vector, the incremental equilibrium equation in terms of the nodal displacement vector over a single element is obtained:

$$[K]^{(e)} \{\Delta \bar{u}\}^{(e)} = \{\Delta R\}^{(e)}$$

By a proper assembly of the incremental element equilibrium equations, the global incremental equilibrium equation will be achieved:

$$[K]\{\Delta\bar{u}\} = \{\Delta R\} \tag{16}$$

Again, as will be discussed in section §10, this equation is simply a linearization of the initial nonlinear equilibrium equation (11), thus itself alone can not produce the accurate stress field and strain field solutions unless a proper residual force evaluation scheme with proper use of the constitutive relation and finite strain description has been implemented simultaneously.

§9 Numerical Integration of Constitutive Equation

As mentioned at the end of §7, a proper numerical integration scheme for the elasto-plastic constitutive equation (12) must be devised to evaluate the finite stress increment $\{\Delta\sigma\}$ caused by the finite strain increment $\{\Delta\varepsilon\}$. This has been a topic of considerable interest and of importance in finite element analysis involving material non-linearity[5,6,7,8].

To facilitate a geometrical interpolation of various integration scheme, **S** and **e** are assumed to represent the vectors of the principal deviatoric stress and strain respectively. Then, assume the initial stress vector at time t is on the current yield surface (otherwise, use Hooke's law to bring it to the yield surface first) and denote the stress vector $\mathbf{S}_c$ as "the contact stress vector".

For Von Mises elastic-plastic materials with Prantl-Reuss associated flow rule, the stress increment vector can be expressed as:

$$\Delta\bar{S} = 2G\Delta\bar{e} - \frac{2G(\bar{S}_c \bullet \Delta\bar{e})}{R_c^2}\bar{S}_c$$

where $R_c^2 = S_c \bullet S_c$ is the current yield surface. Then

$$\bar{S}_f = \bar{S}_c + \Delta\bar{S}$$

This is called "direct method" without any correction[8]. As shown in Figure 2.4(a), the final stress vector S_f is seldom on the yield surface any more and therefore violates the yield surface consistancy condition (for simplicity, here we assume perfact elastoplasticity).

Denote $\Delta S_e = 2G\Delta e$, then the sum of two vectors $S_t = S_c + \Delta S_e$ is called the trial stress, or "elastic predictor". The efforts to bring the trial stress back to the yield surface can be classified as:

(1) <u>The Tangential Stiffness and Radial Return</u>

In this method the final stress vector is forced back to the yield surface in the direction of S_f calculated by direct method, thus

$$\bar{S}_f = \rho\left[\bar{S}_c + 2G\Delta\bar{e} - \frac{2G(\bar{S}_c \bullet \Delta\bar{e})}{R_c^2}\bar{S}_c\right]$$

where $0 \le \rho \le 1$ is the constant to bring back S_f. Figure 2.4(b) shows the method geometrically. This method is first introduced by Marcal[9].

(2) <u>The Secant Stiffness Method</u>

This method introduce an intermediate stress vector using the trial stress $\mathbf{S}_t$ and the contact stress $\mathbf{S}_c$:

$$\bar{S}_i = \frac{1}{2}(\bar{S}_t + \bar{S}_c)$$

Then, the final stress state is given by

$$\bar{S}_f = \bar{S}_t - \frac{2G(\bar{S}_i \bullet \Delta\bar{e})}{R_i^2}\bar{S}_i$$

where $R_i^2 = S_i \bullet S_i$. Rice and Tracy[10] proved this final stress vector happens to be on the yield surface. The method is pictured in Figure 2.4(c).

(3) <u>The Radial Return Method</u>

This method simply returns the trial stress vector to the yield surface directly (see Figure 2.4(d)), i.e.

$$\bar{S}_f = \lambda\left(\bar{S}_c + 2G\Delta\bar{e}\right)$$

where $0 \le \lambda \le 1$ is determined by the consistency condition $S_f \bullet S_f = R$. The method was first proposed by Wilkins[11]. Studies indicate that this method may look simple but the accuracy has been proved better than the first two[8].

Studies regarding to the superiority of one method over another are extensive. It has

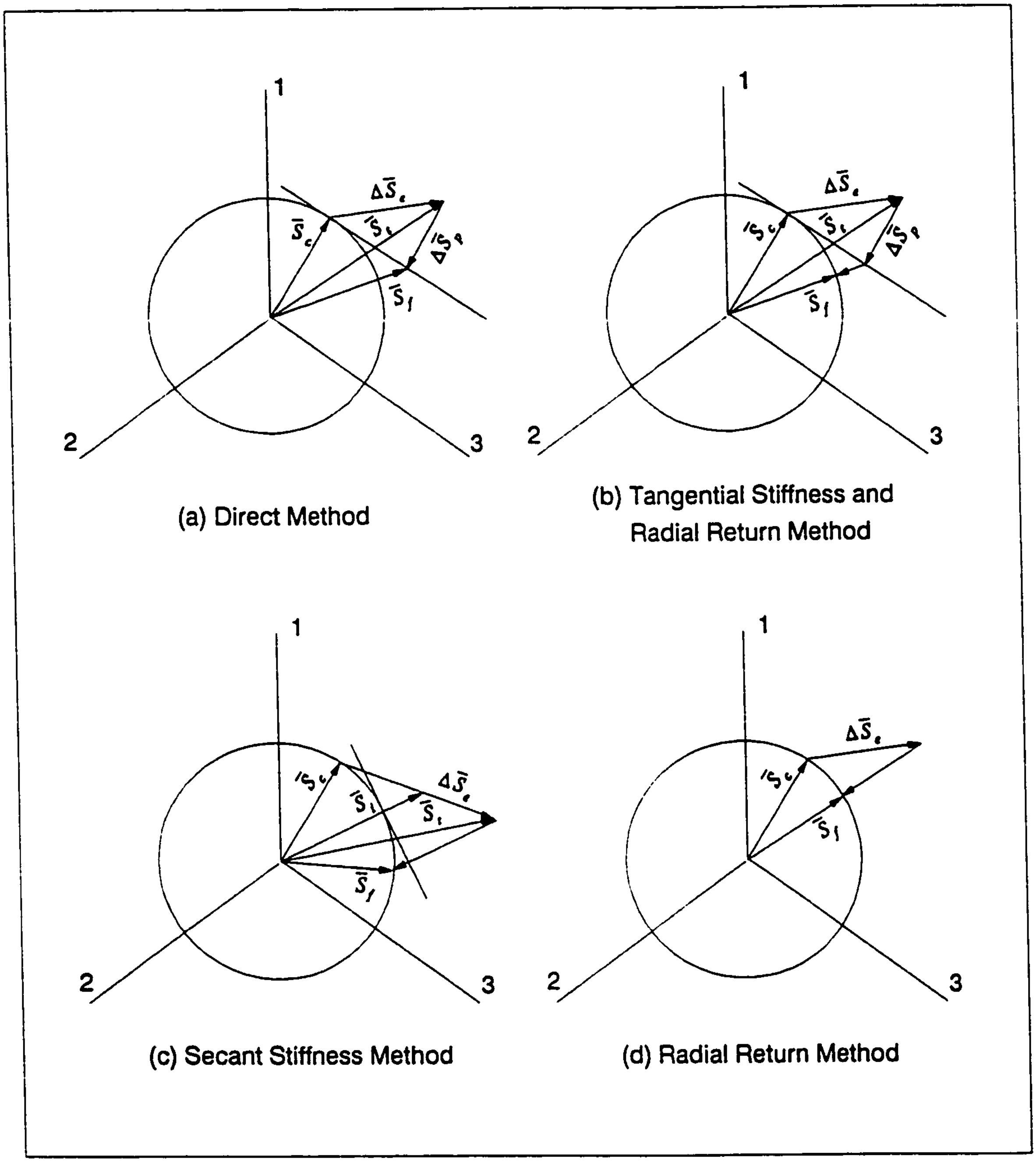

Figure 2.4 Geometrical Interpretation of Constitutive Equation Integration Schemes

not been the purpose of this study to make another judgement. Since it is obvious that the accuracy of the stress increment calculation should be improved by integrating the rate form directly over the time interval [t,t+Δt]:

$$\Delta\bar{S} = \int_{t}^{t+\Delta t} d\bar{S}$$

a multi-step method is adopted in this study. In each substep, tangential stiffness and radial return method is used.

§10 **Modified Newton-Raphson Method** - Residual Force Evaluation

For a nonlinear equation:

$$\bar{R}(\bar{x}) = \bar{\varphi}(\bar{x}) - \bar{f} = \bar{0}$$

if there is an initial approximate solution $\mathbf{x}^{(i)}$ which makes

$$\bar{R}(\bar{x}^{(i)}) = \bar{\varphi}(\bar{x}^{(i)}) - \bar{f} \neq \bar{0}$$

Then the question is how to obtain an improved solution $\mathbf{x}^{(i+1)}=\mathbf{x}^{(i)}+\Delta\mathbf{x}^{(i)}$. According to Taylor's series $\mathbf{R}(\mathbf{x})$ can be approximated in the neighbourhood of $\mathbf{x}^{(i)}$ by

$$\bar{R}(\bar{x}^{(i+1)}) \approx \bar{R}(\bar{x}^{(i)}) + \frac{d\bar{R}(\bar{x}^{(i)})}{d\bar{x}} \Delta\bar{x}^{(i)} = \bar{R}(\bar{x}^{(i)}) + K_T^{(i)} \Delta\bar{x}^{(i)}$$

where

$$K_T^{(i)} = \frac{d\bar{R}(\bar{x}^{(i)})}{d\bar{x}} = \frac{d\bar{\varphi}(\bar{x}^{(i)})}{d\bar{x}}$$

is the tangent stiffness matrix. Therefore,

$$\bar{R}(\bar{x}^{(i+1)}) = \bar{0} \quad \Longrightarrow \quad K_T^{(i)} \Delta\bar{x}^{(i)} = -\bar{R}(\bar{x}^{(i)}) = -\bar{R}^{(i)}$$

where $\mathbf{R}^{(i)}$ is usually called the residual force vector of the *i*th iteration;

$\Delta\mathbf{x}^{(i)}$ is the correction displacement increment in the *i*th iteration.

In numerical implementation of the Newton-Raphson algorithm, it should be particularly emphasized that:

(1) accurate tangent $\mathbf{K}_T$ is seldom a practical choice, because (a) as been discussed in §6, even in the initial formulation, compromise has been made to preserve the symmetry of the stiffness matrix; (b) modified Newton-Raphson is well accepted in the practice, where $\mathbf{K}_T^{(i)}=\mathbf{K}_T^{(0)}$ is only formed once at the first iteration and remains constant in the rest of iterations, because in finite element calculation to update $\mathbf{K}_T^{(i)}$ is usually more expensive than to increase the number of iterations for convergence. Thus, $\Delta\mathbf{x}^{(i)}$ can be solved simply from

$$\mathbf{K}_T^{(0)} \Delta \bar{x}^{(i)} = \bar{R}^{(i)}$$

The implication is that $\mathbf{K}_T$ formulation may have an impact on the efficiency of the numerical iterations but not on the final solution, should an objective residual force evaluation has been correctly implemented and the process converge.

(2) To evaluate the residual force correctly requires to go back to the original nonlinear equation (7) (i.e. the "future virtual work" equation). Based on the currently obtained solution (displacement, strain and stress), (7) now can be fully evaluated, so is the accuracy of the solution. The numerically discretized equation (7) is as follows:

$$\int_{\Omega^{t+\Delta t}} [B_o]\{\sigma^{t+\Delta t}\} d\Omega^{t+\Delta t} = \int_{\Omega^{t+\Delta t}} \rho [N]^T [N]\{\bar{b}^{t+\Delta t}\} d\Omega^{t+\Delta t} + \int_{\Gamma_F^{t+\Delta t}} [N]^T [N]\{\bar{t}^{t+\Delta t}\} d\Gamma_F^{t+\Delta t}$$

Where $[B_o]$ is the conventional small strain matrix but calculated on $\gamma^{t+\Delta t}$ based on the current solution. $\{\sigma^{t+\Delta t}\}=\{\sigma^t\}+\{\Delta\sigma\}$ is Cauchy true stress tensor at time t+Δt. As been discussed in §6, material deformation and rotation are two key factors in updating $\{\sigma^t\}$.

§11 Stress Update Algorithm

Based on the discussion in §5 and §6, a stress tensor updating algorithm is advised as follows:

(1) Using the obtained displacement field $\{\Delta u\}$, calculate the deformation gradient tensor $\mathbf{\Delta F}$;

(2) Polar decomposed $\Delta\mathbf{F}$ into the pre-stretch tensor $\Delta\mathbf{U}$ and the rotation tensor $\Delta\mathbf{R}$;

(3) Using $\Delta\mathbf{U}$-1 as strain increment, calculate the co-rotational stress increment $\Delta\sigma^*$ by a proper stress integration scheme. A multi-step "elastic predictor and radial return method"[8] is adopted in this work;

(4) Update the stress tensor by rotating the reference frame back to the global Cartesian coordinates: $\sigma^{t+\Delta t}=\Delta\mathbf{R}^T\bullet(\sigma^t+\Delta\sigma^*)\bullet\Delta\mathbf{R}$.

§12 Sample Calculations

A computer code based on the discussed large deformation formulation was started in 1991 with the emphasis on the numerical analysis of metal forming processes. Since then, many progresses have been made in terms of element library, interface with other commercial software, friction boundary condition implementation and numerical stability, etc. Various metal forming processes have also been successfully analyzed using the code. Two examples are used here to demonstrate the capability of the code.

§12-1 Cylinder Block Compression

This is a rather standard test for two dimensional situation. The size of the cylinder is ϕ20mmX30mm. The boundary condition on the contact surface is assumed as sticky. The mechanical properties used are as follows: Young's modulus E=200 kN/mm^2, Poisson's ratio $\nu = 0.3$, initial yield strength $\sigma_Y = 0.7$ kN/mm^2, strain hardening $H' = 0.3$ kN/mm^2.

It is well recognised that for elastic-plastic materials the response of finite elements tends to be too stiff in a fully plastic range[16]. This is because of the difficulty for many isoparametric elements to represent the constant volume mode over the entire element area. Therefore, when incompressibility condition is implemented through the constitutive law with a full integration scheme, it tends to be too severe for elements to deform. The element mesh is then volume-locked.

After careful examination of the behaviours of many elements, Nagtegaal *et al*[16] proved a special pattern of four constant strain triangles obtained from the diagonal meet of a quadrilateral to be most advantagious in avoiding the volume locking. This mesh pattern is called 4CST (4 Constant Strain Triangular) elements. Six-node isoparametric element is also mentioned as advantagious for preventing volume locking.

Due to the symmetry of the problem, only a quarter of the block is meshed. As shown in Figure 2.5, both 4CST elements and 6-node elements are used in the this analysis.

Figure 2.6-2.8 show the simulated deformation process from 4CST elements, 6-node with 7-point dquadrature and 6-node with 6-point quadrature. They all display very similar deformation and effective stress distribution patterns, except that 4CST elements seem a little less able to represent the material folding toward the punch surface at the upper righthand corner.

Figure 2.9-2.11 show the normal loading stress distributions on the punch tool interface associated with the previously mentioned cases. Those results show similar patterns, however, six-node elements are stiffer in terms of loading stress values.

Results from 6-point and 7-point integrations are essentially the same. Similar results are also observed for quadrilateral elements. Reduced or selectively reduced integration (2X2 for 8/9-node and 1X1 for 4-node element) can produce very similar results to the full integration if convergence is achieved. Quadrilateral elements are not used in this case

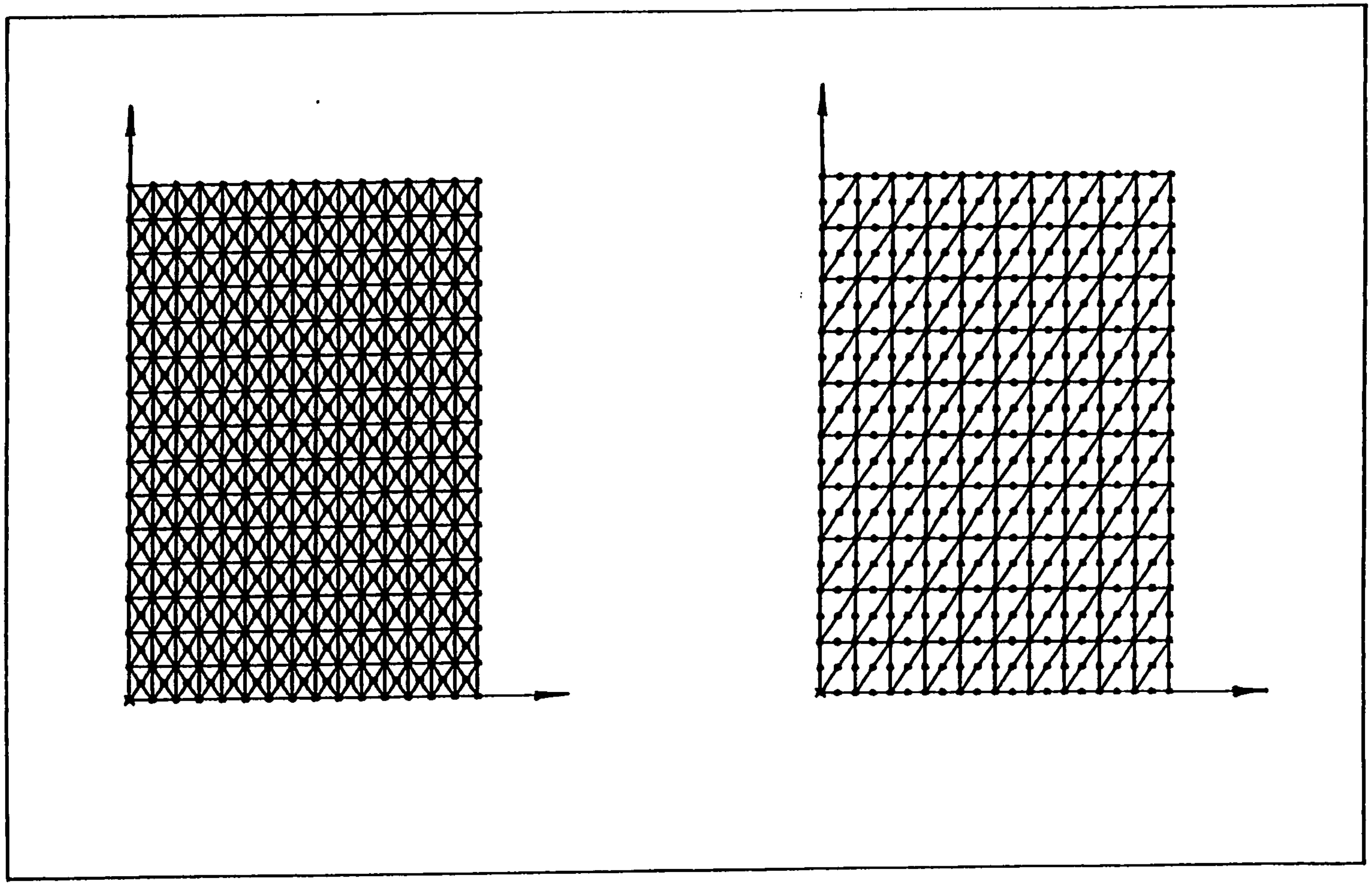

Figure 2.5 Mesh Patterns for Cylindrical Block Compresssion Analysis

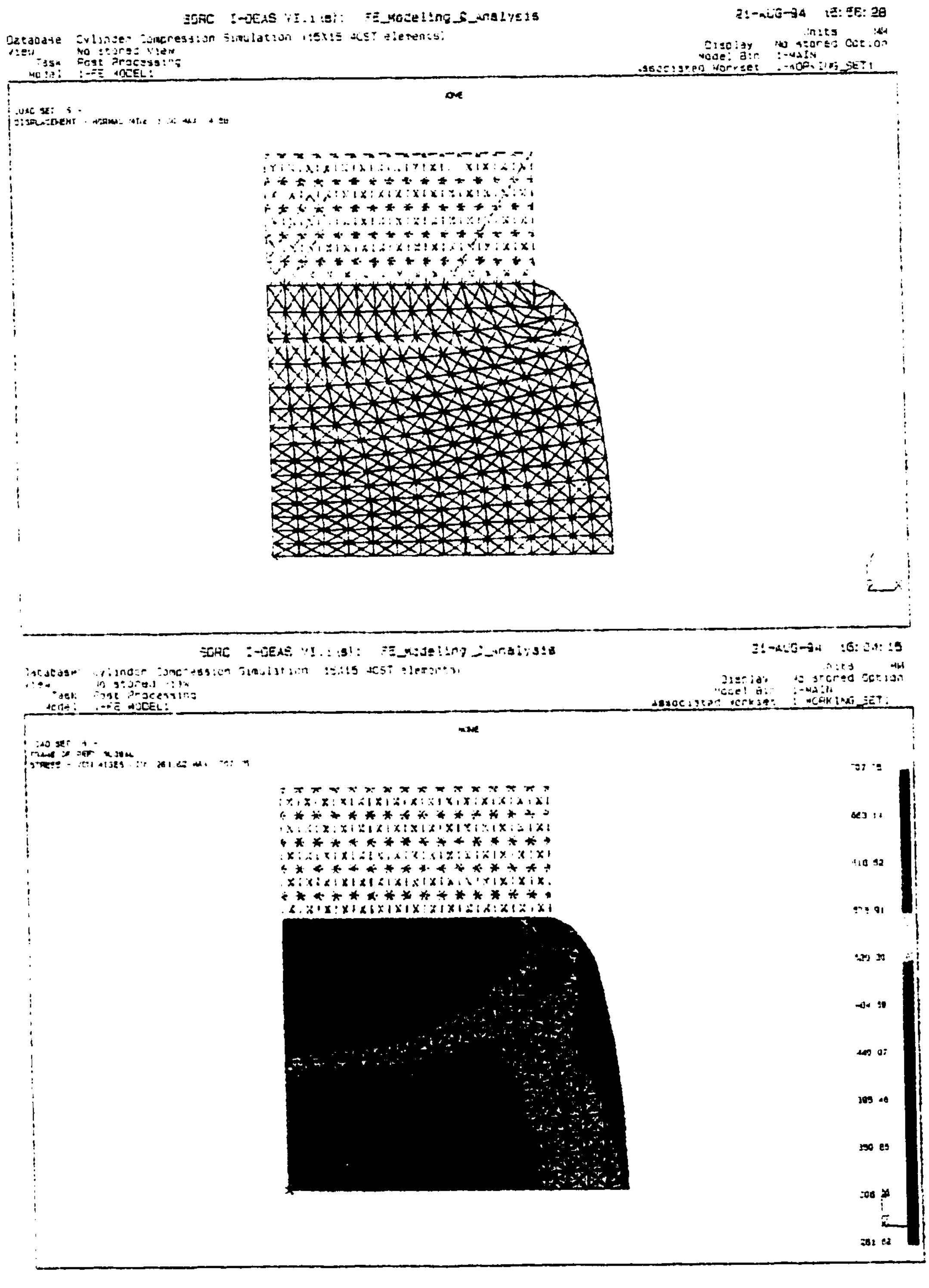

Figure 2.6(a) Cylindrical Block Compression

(4CST elements, 32.5% reduction)

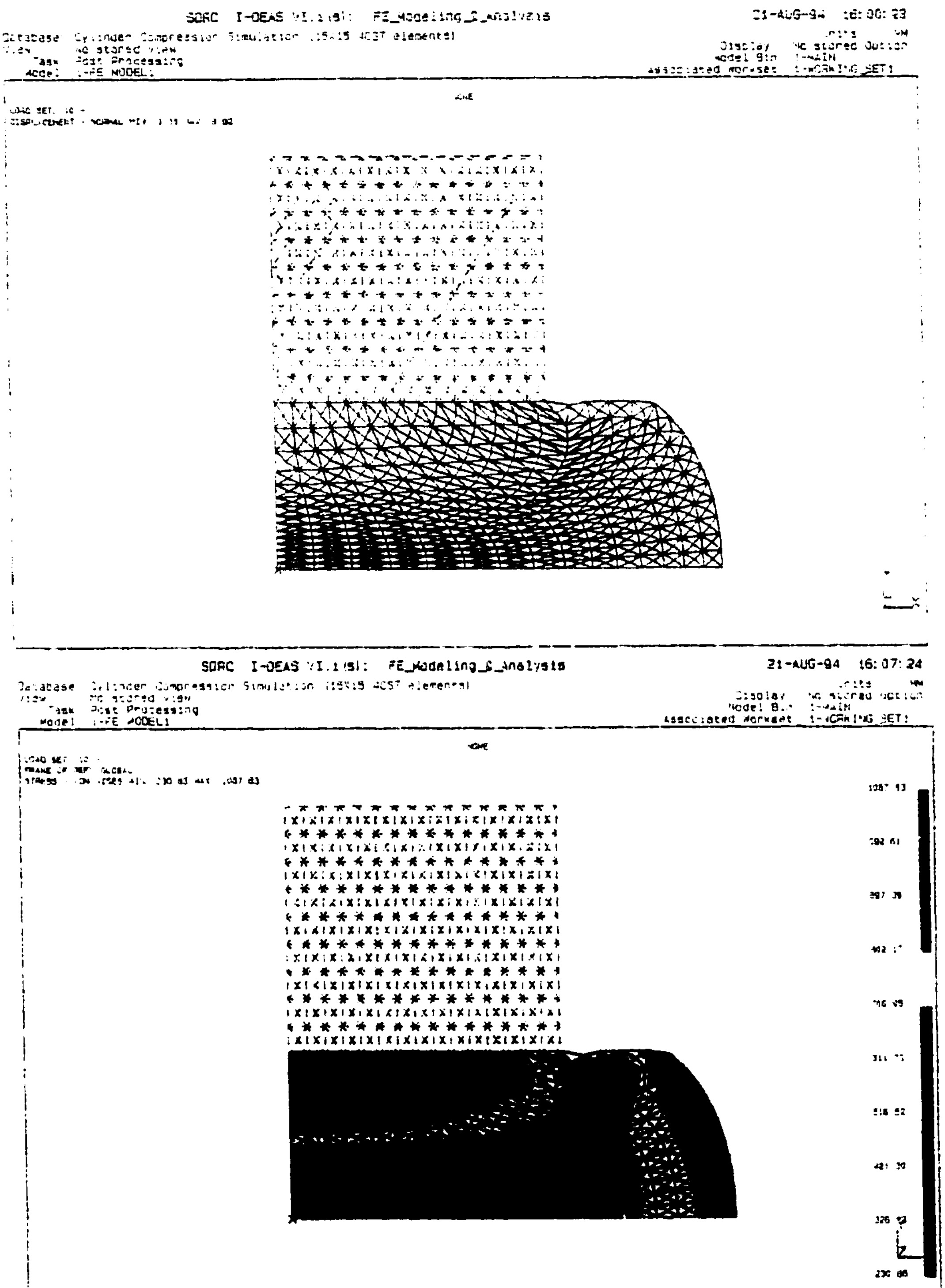

Figure 2.6(b) Cylindrical Block Compression

(4CST elements, 59.4% Reduction)

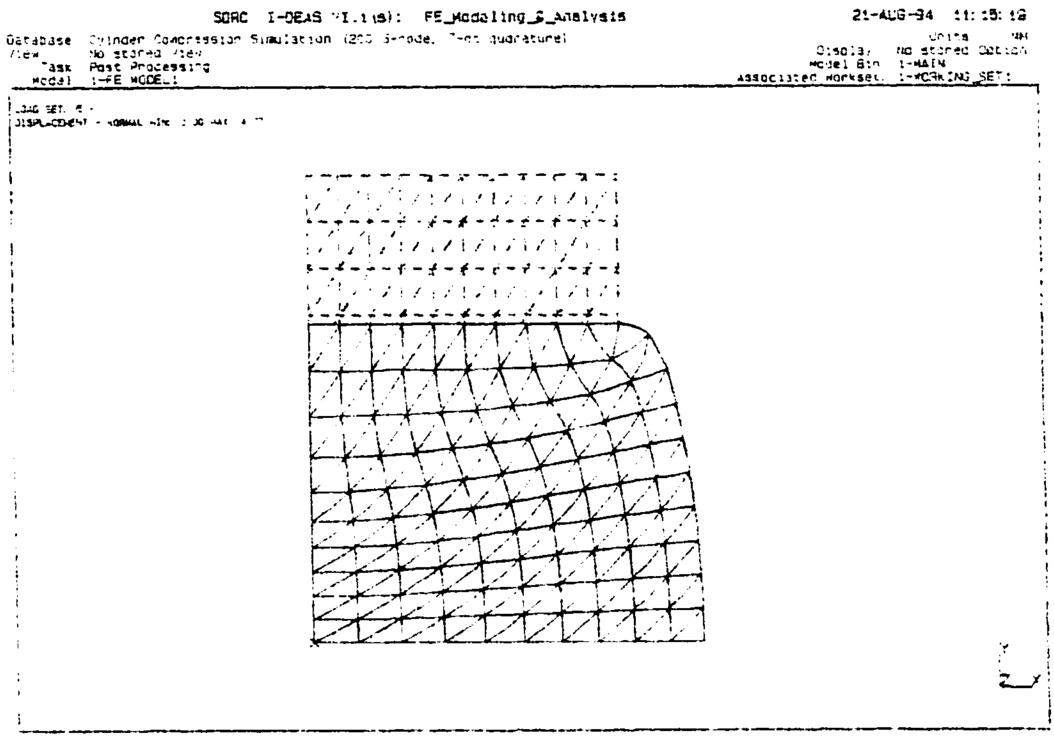

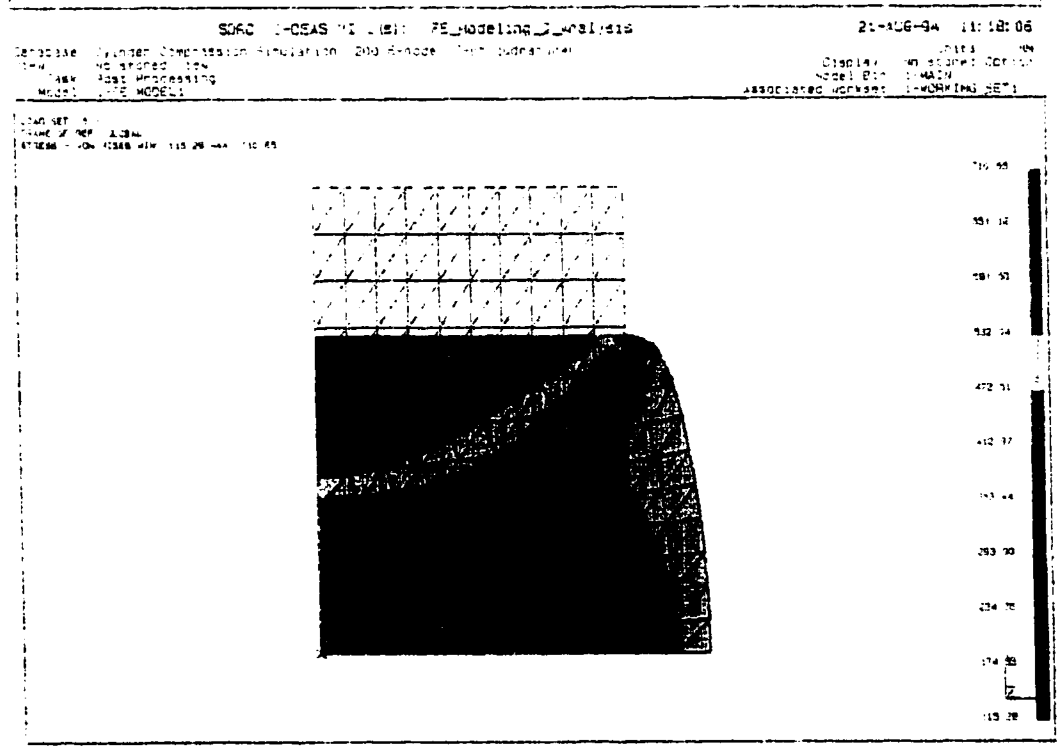

Figure 2.7(a) Cylindrical Block Compression (6-node, 7-pt. quadrature, 31.8% reduction)

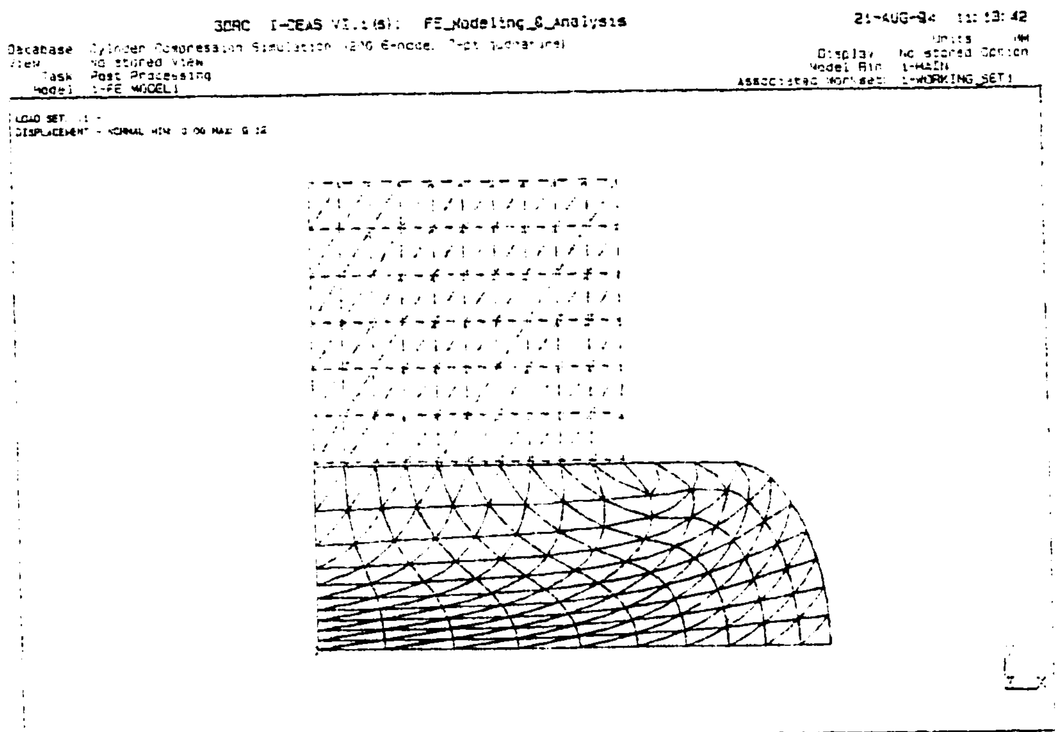

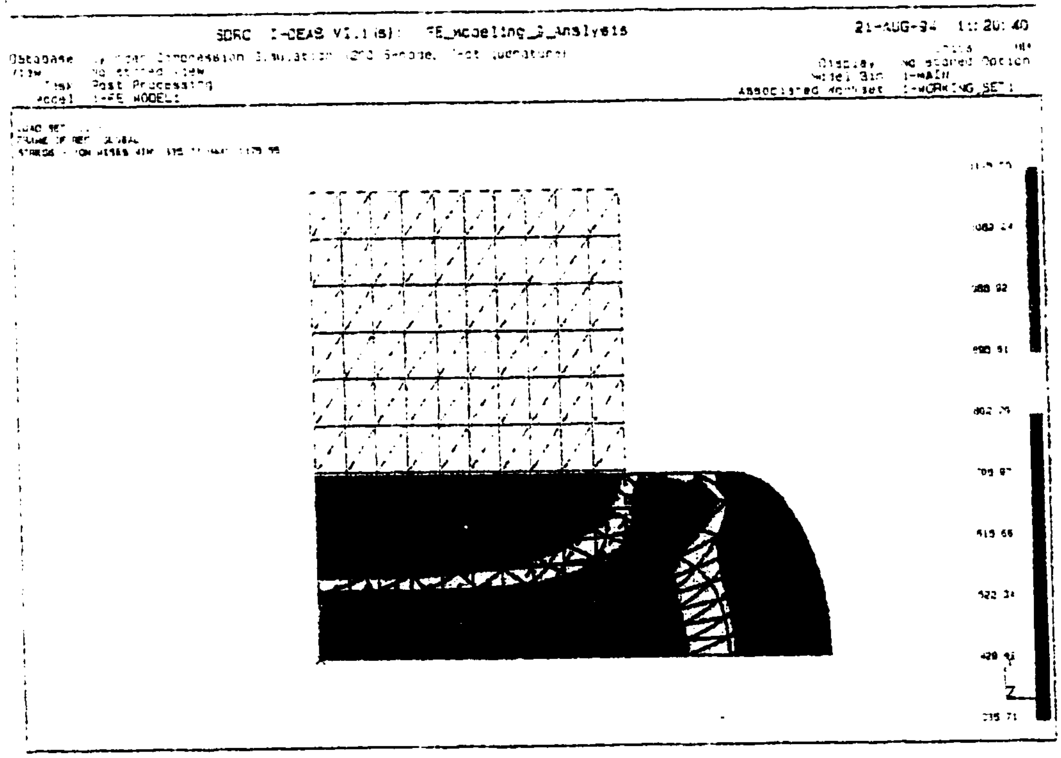

Figure 2.7(b) Cylindrical Block Compression (6-node, 7-pt. quadrature, 60.8% reduction)

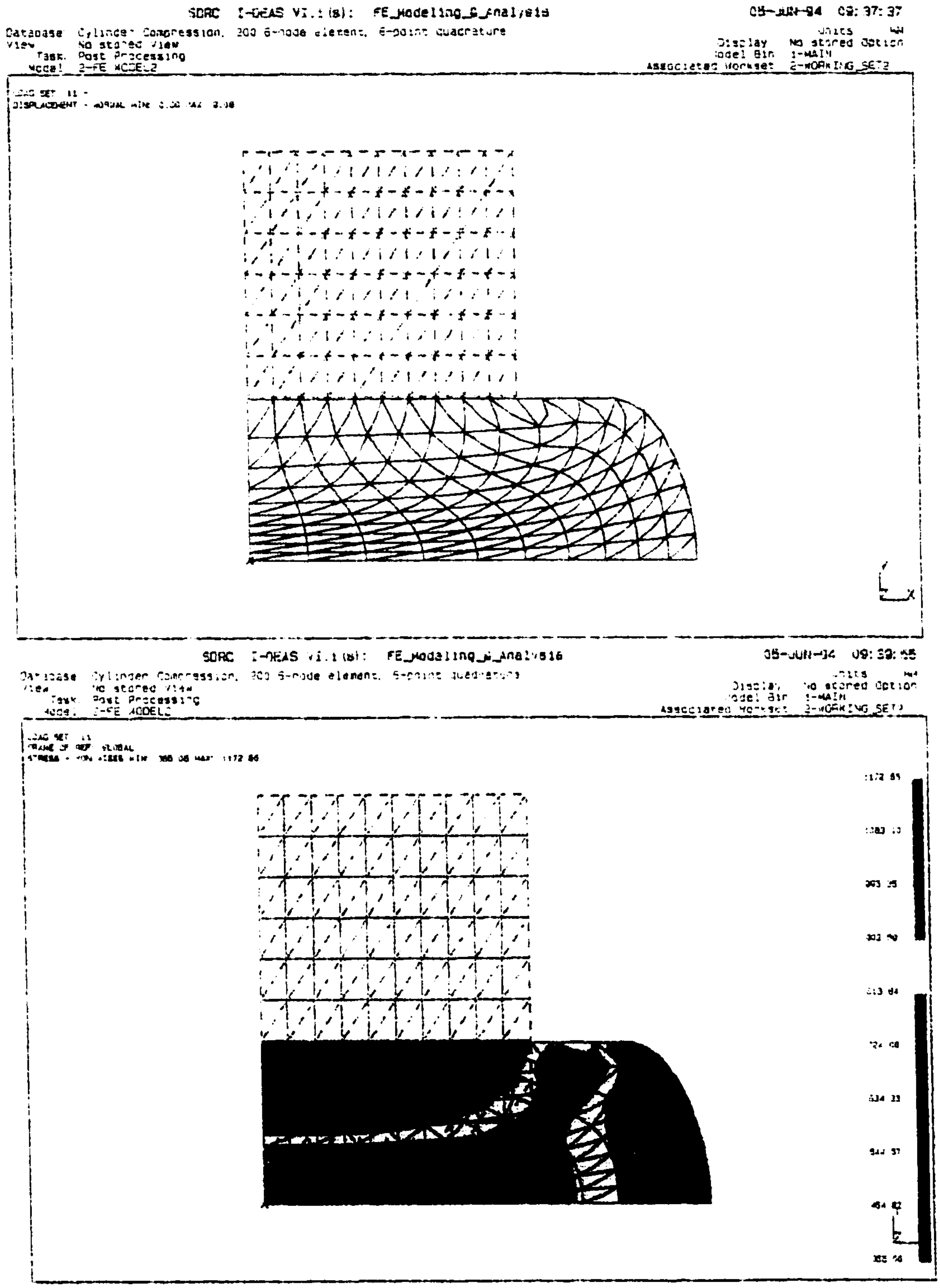

Figure 2.8 Cylindrical Block Compression (6-node, 6-pt. quadrature, 60.5% reduction)

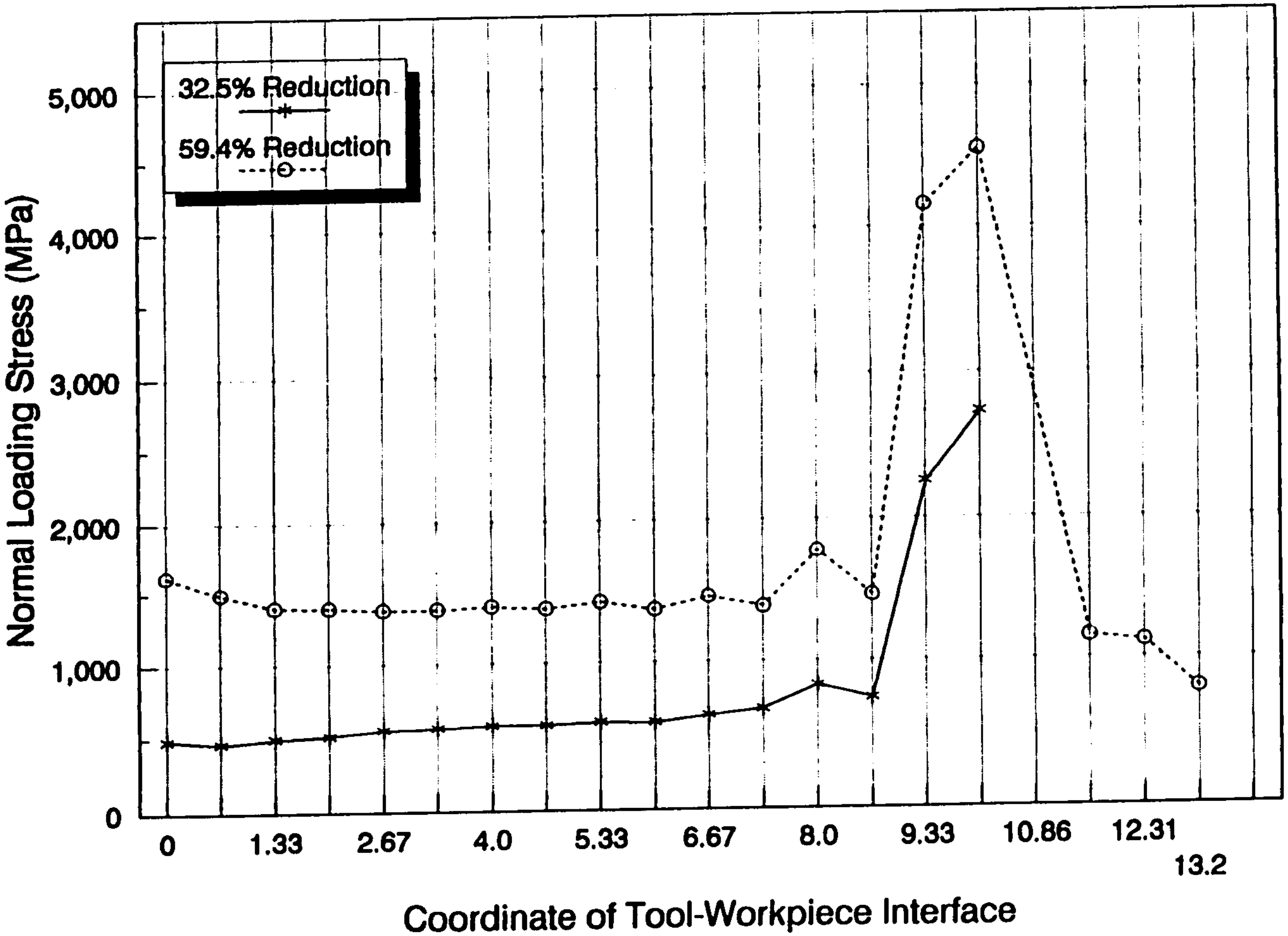

Figure 2.9 Normal loading Stress Distribution on Contact Boundary (4CST elements)

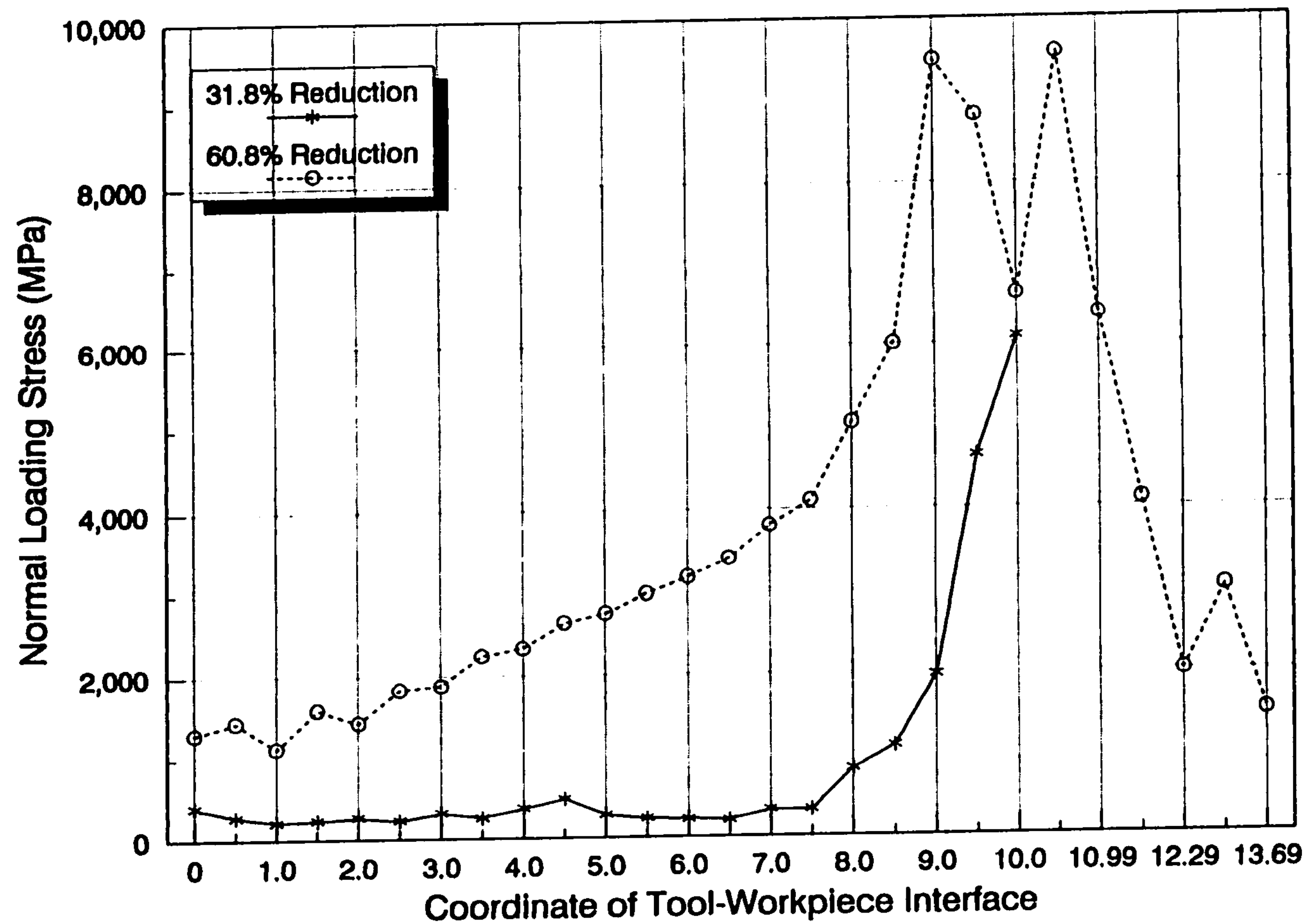

Figure 2.10 Normal loading Stress Distribution on Contact Boundary (6-node, 7-pt. quadrature)

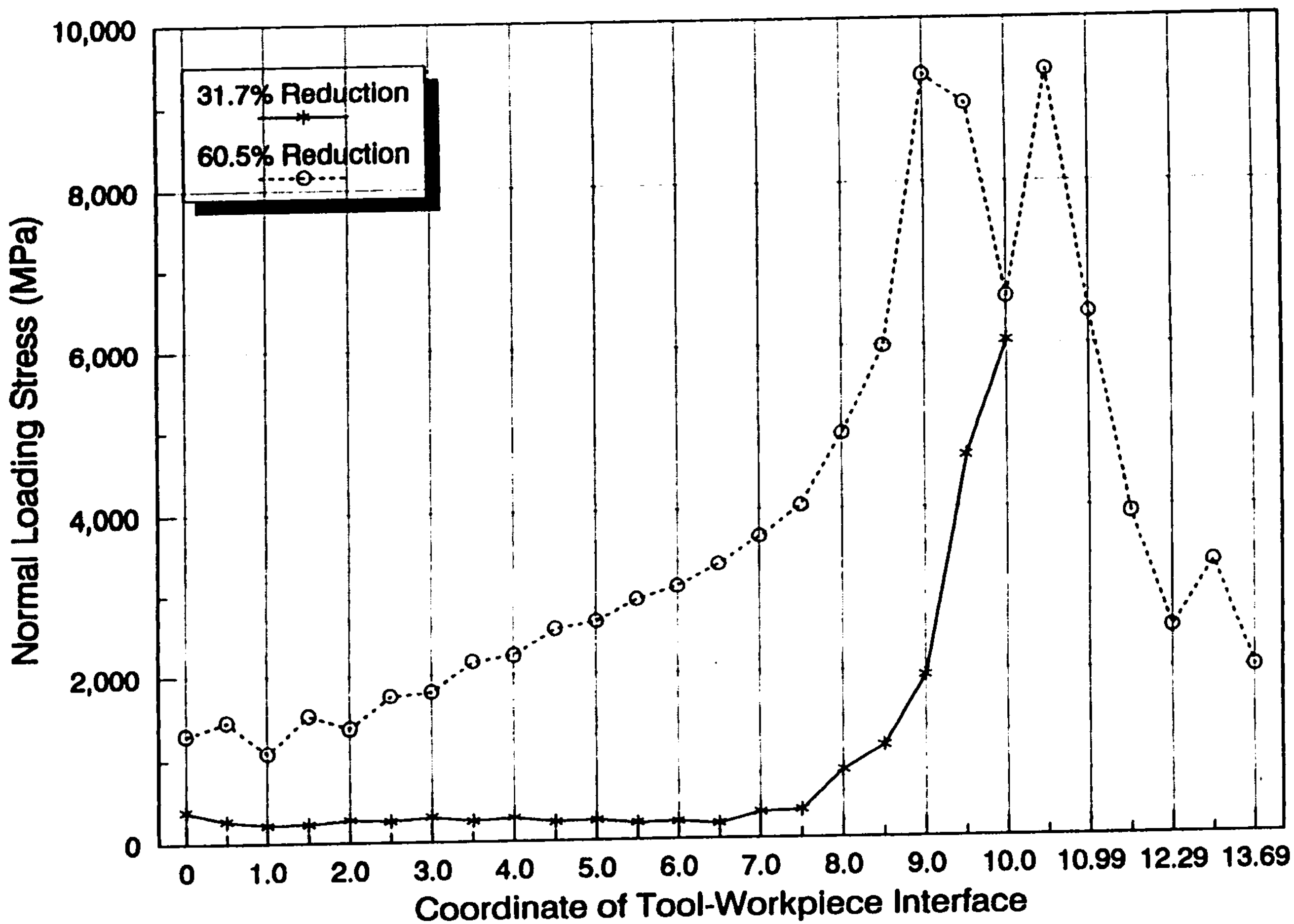

Figure 2.11 Normal loading Stress Distribution on Contact Boundary (6-node, 6-pt. quadrature)

because of their inability to represent the material folding at the corner.

§12-2 Cylinder Head Forging

Cylinder head forging is a practical example which is cited by Kikuchi[18]. The dimension of the process is shown in Figure 2.12. The mesh used for this analysis is also shown in Figure 2.12. The special quadrilateral arrangement of four constant strain triangular elements (4CST-Elements) is used here to avoid the volumn locking. In order to obtain a smooth folding of the material moving toward the tool surface, finer mesh is added at the two corner areas. The boundary condition on all the tool-workpiece interfaces is assumed sticky.

Again, the material properties are specified as follows: Young's modulus E=200 kN/mm^2, Poisson's ratio $v = 0.3$, initial yield strength $\sigma_Y = 0.7$ kN/mm^2, strain hardening $H\_ = 0.3$ kN/mm^2.

As shown in Figure 2.13(a) and (b) (at 18.8% and 69% reduction respectively), the mesh performs quite well in taking the large deformation, including the extraordinary distortion at the top and bottom corner of the head.

The effective stress distribution is in line with the mesh deformation which is that the most severe deformation occurs at the corners and diagonally develops into the center of the head, leaving two less deformed wedges to push into the head from the top and bottom centers of the head. This is a well expected deformation pattern with abundent experimental evidence.

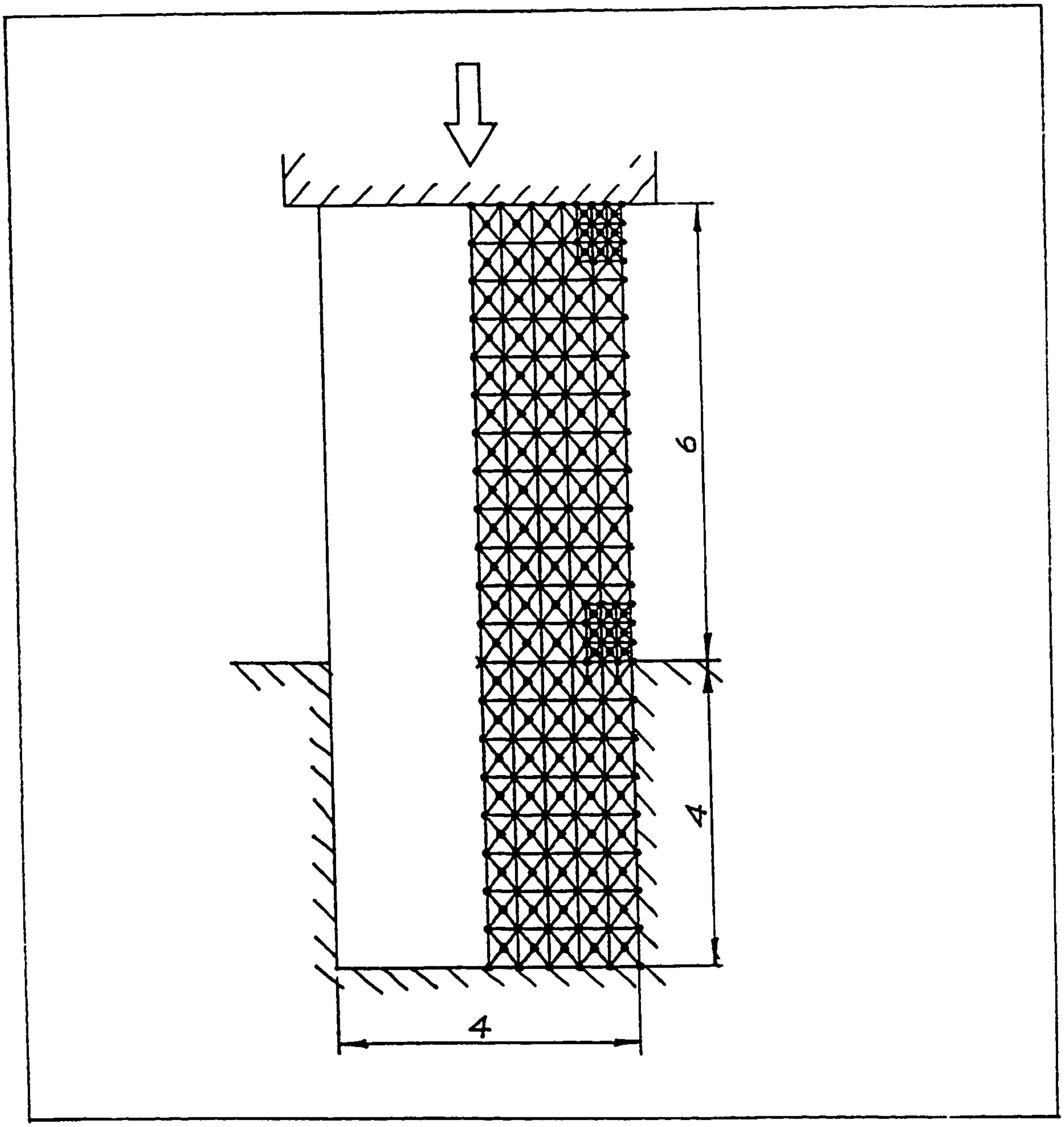

Figure 2.12 The Dimension of The Cylinder Head Forging

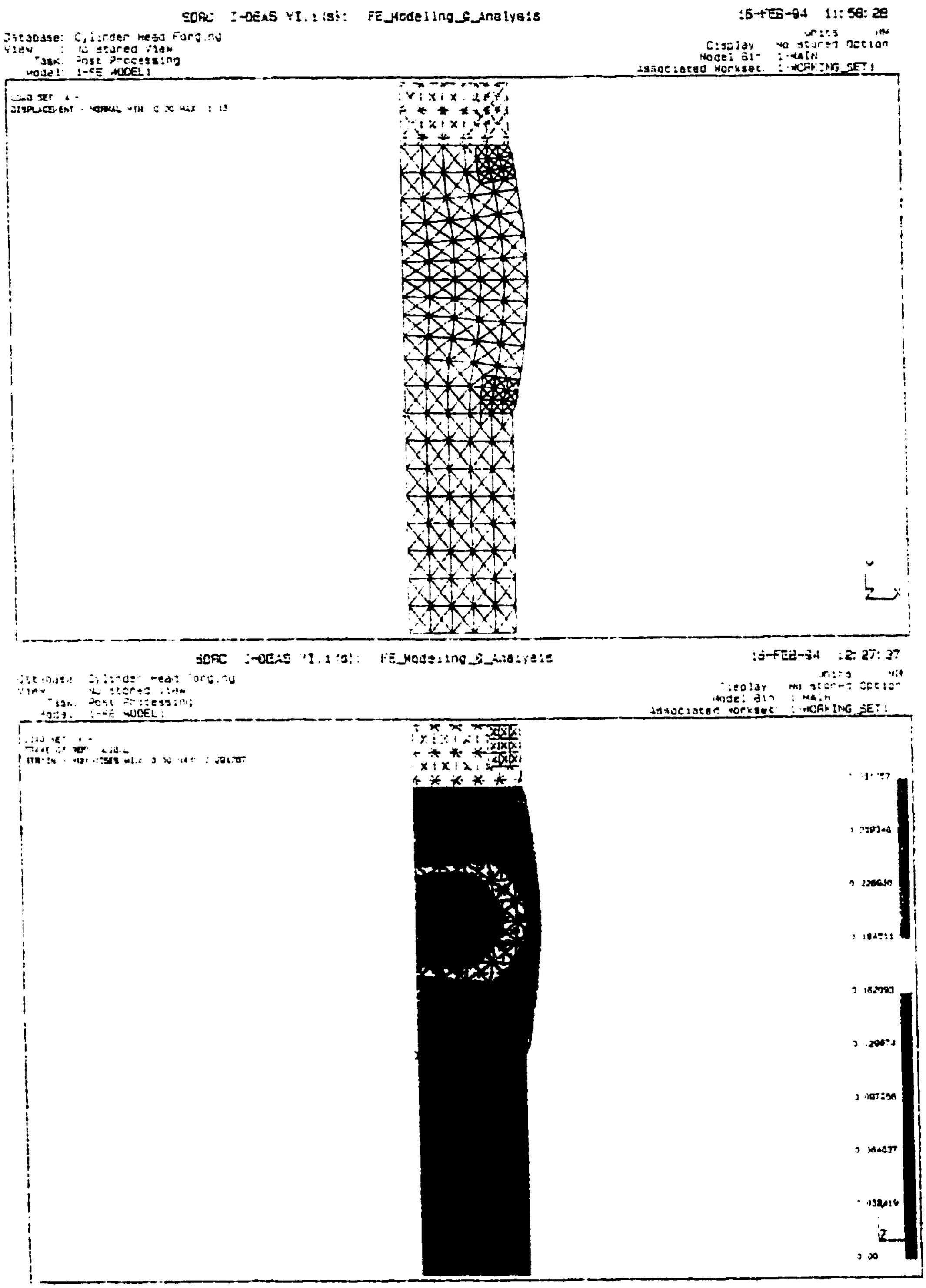

Figure 2.13(a) Simulation of Cylinder Head Forging (18.8% reduction)

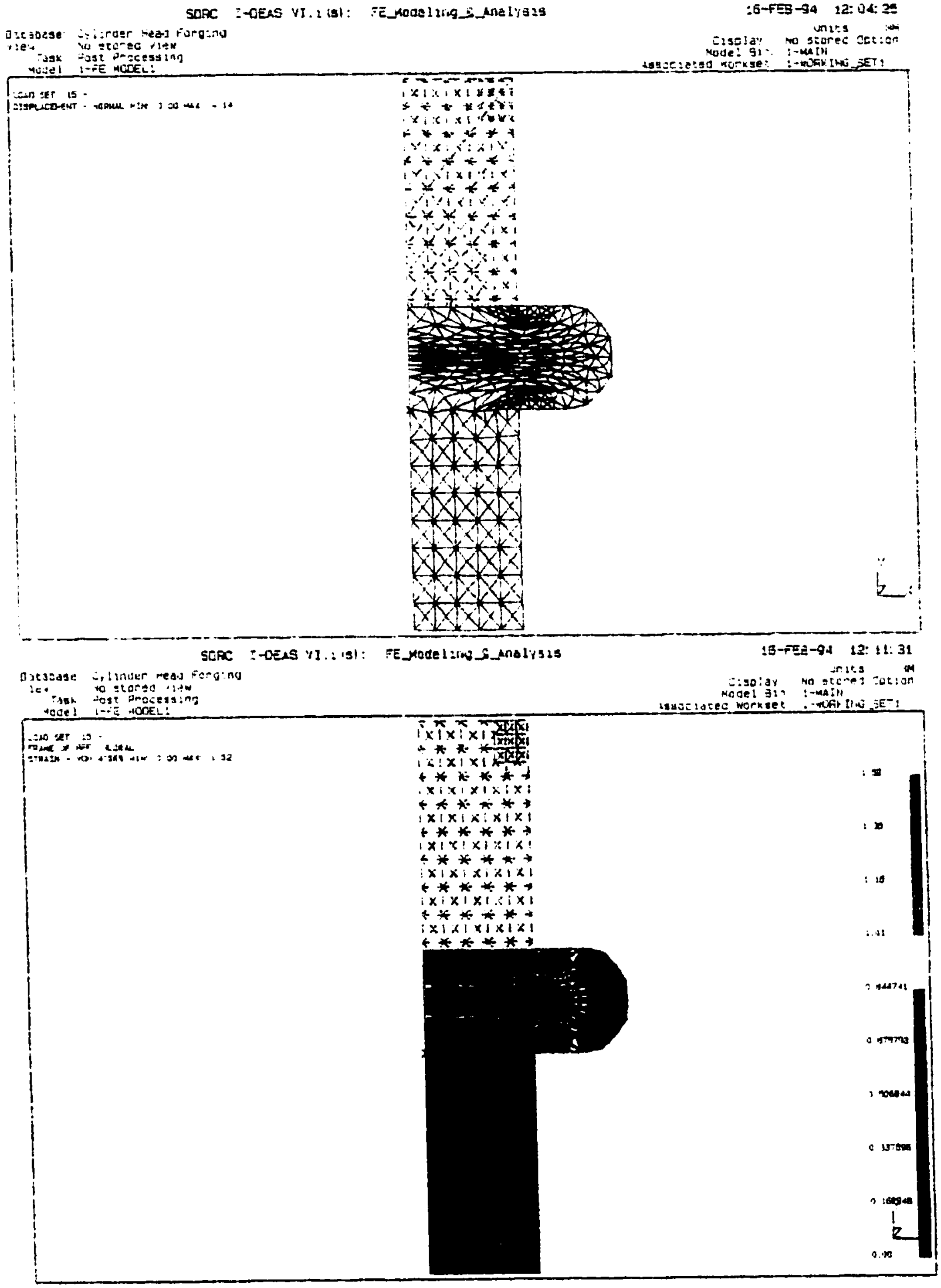

Figure 2.13(b) Simulation of Cylinder Head Forging (69% reduction)

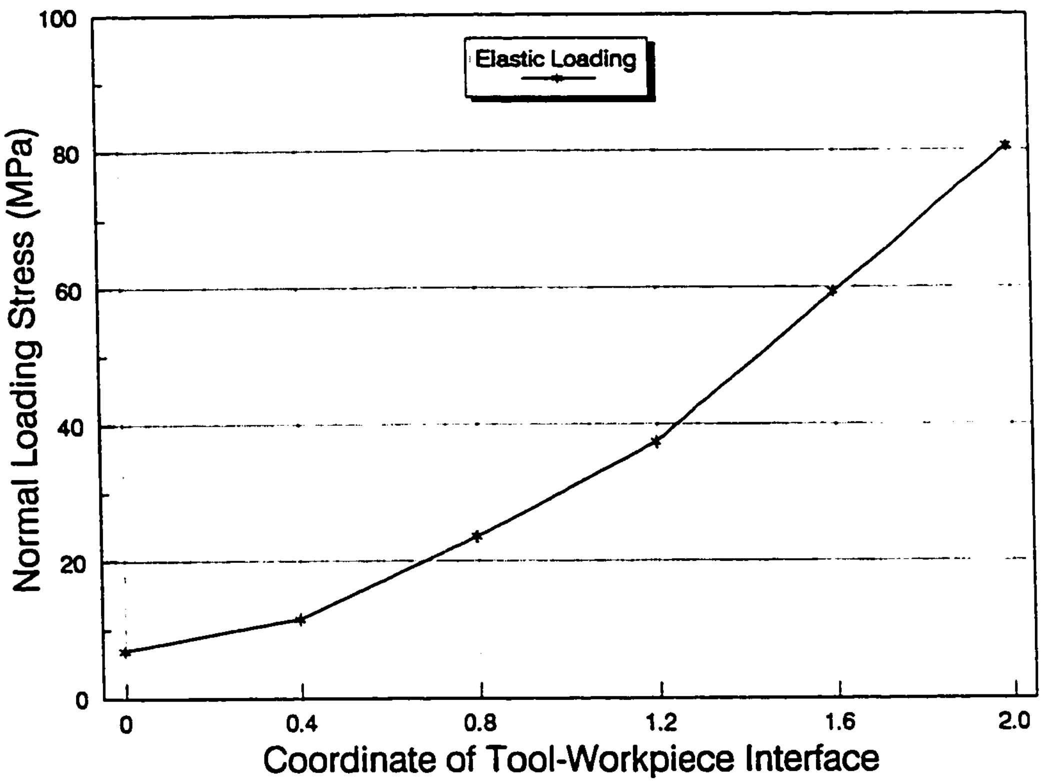

Figure 14(a) Normal Stress Distribution on Contact Surface (0.2% reduction)

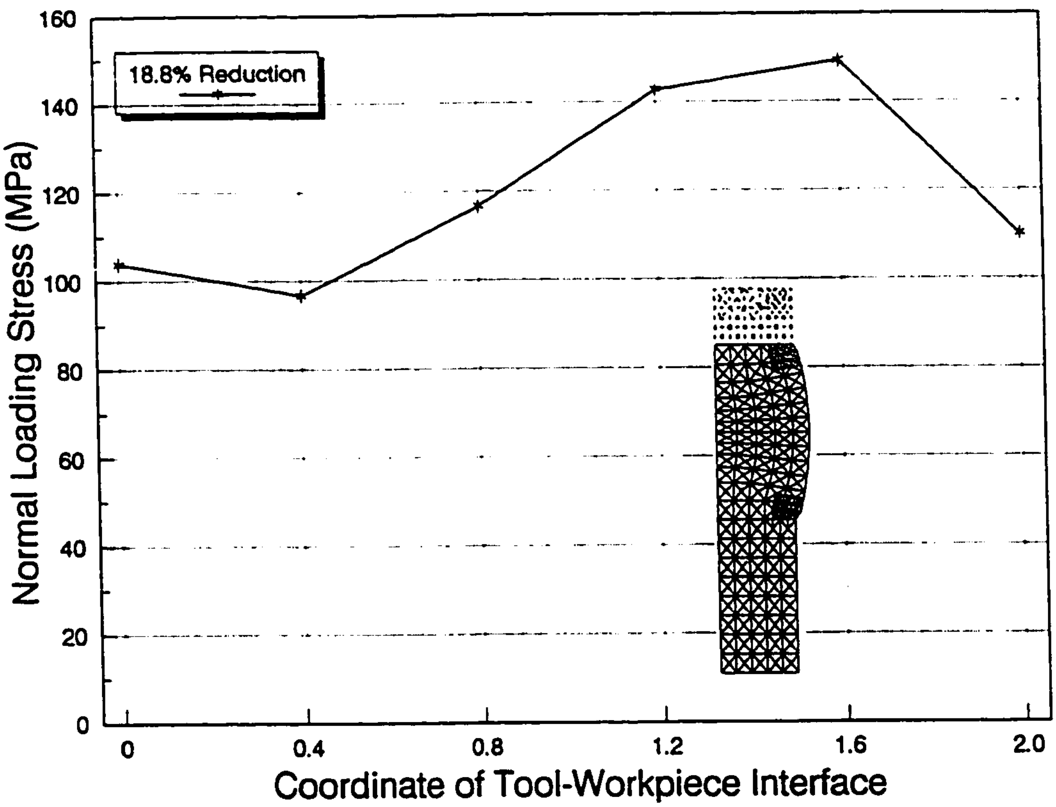

Figure 2.14(b) Normal Stress Distribution on Contact Surface (18.8% reduction)

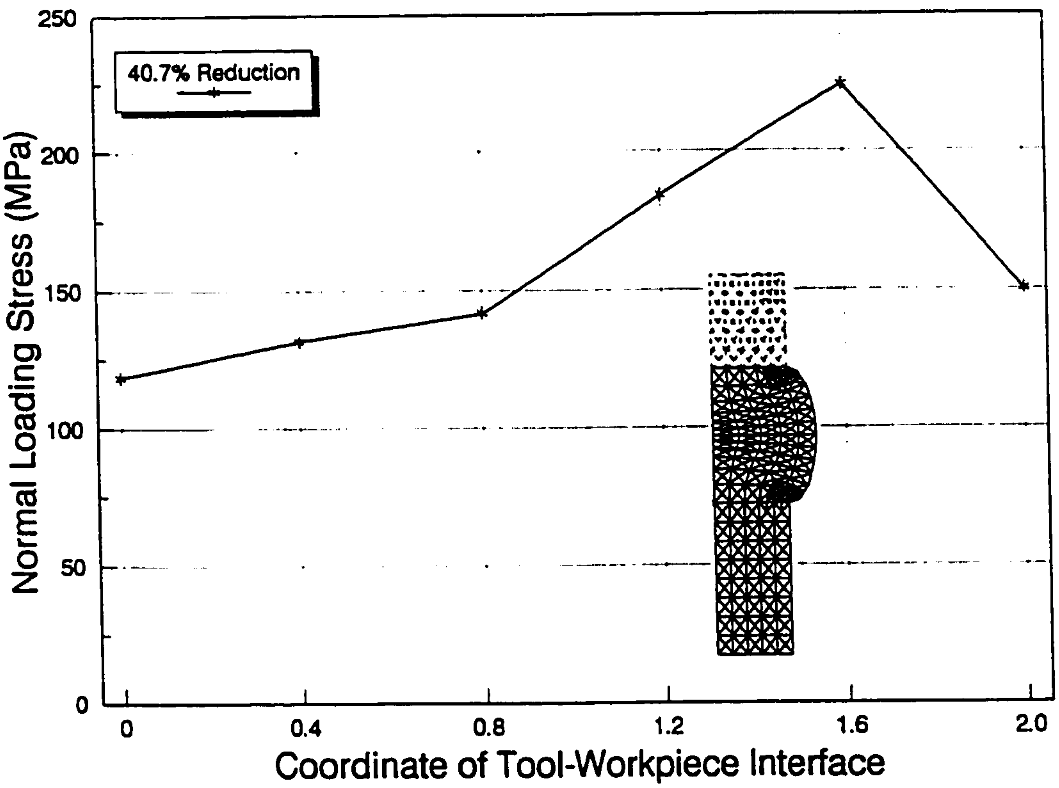

Figure 2.14(c) Normal Stress Distribution on Contact Surface (40.7% reduction)

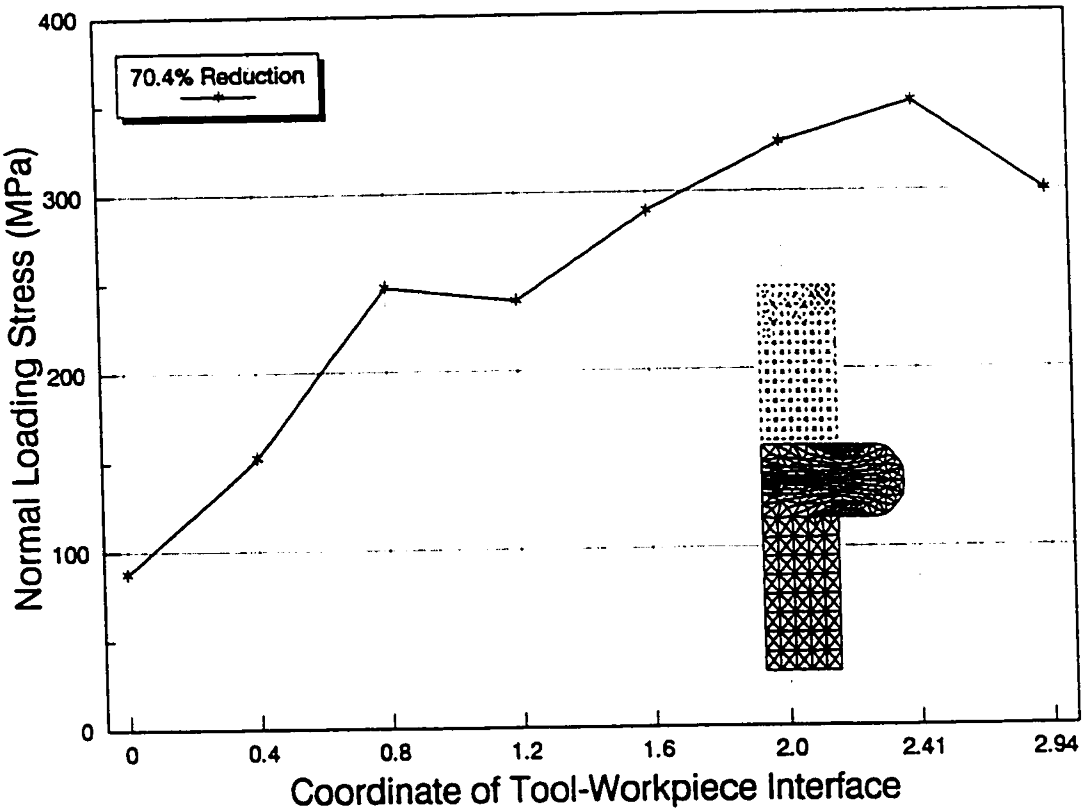

Figure 2.14(d) Normal Stress Distribution on Contact Surface (70.4% reduction)

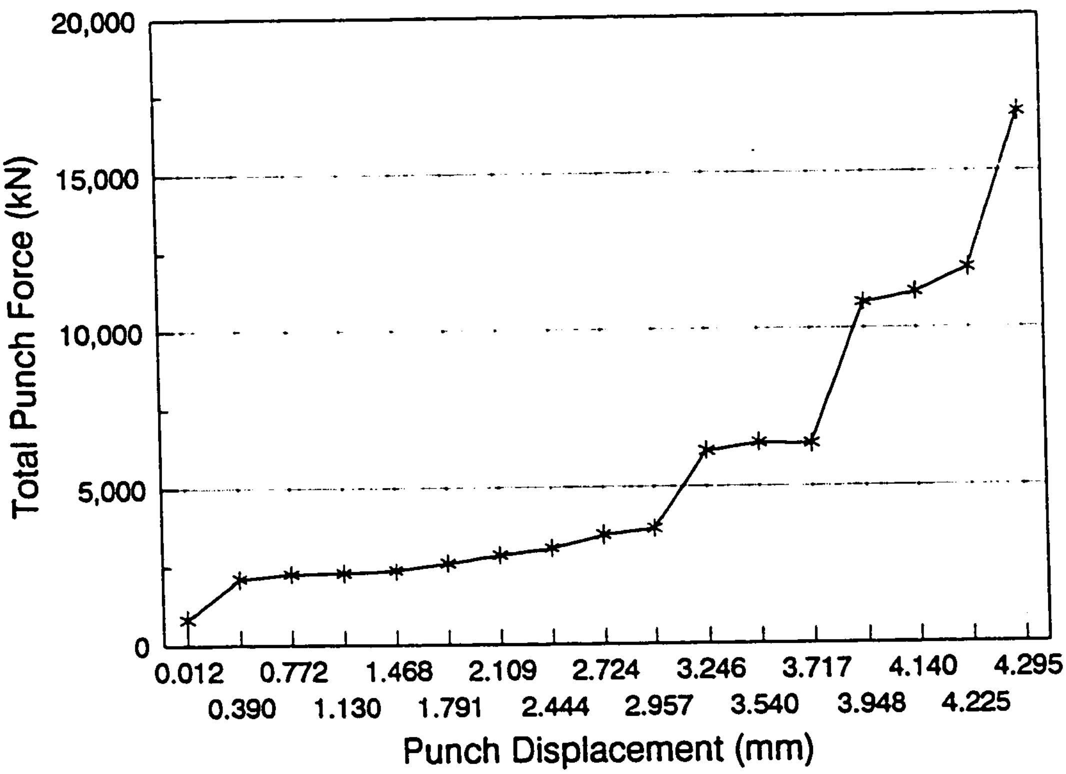

Figure 2.15 Total Punch Force vs Displacement

§13 References

[1] McMeeking, R.M. and Rice, J.R., *Finite element formulations for problems of large elastic-plastic deformation*, Inter. J. Solids Struct., **11** (1975), p601-616.

[2] Hill, R., *The Mathematical Theory of Plasticity*, Clarendon Press, Oxford, 1956

[3] Pillinger, I. Hartley, P. Sturgess, C.E.N. and Rowe, G.W., *A new linearized expression for strain increment in finite element analysis of deformations involving finite rotation*, Int. J. Mech. Sci., **28** (1986), p253-262.

[4] Yamada, Y., Yoshimura, N. and Sakurai, T., *Plastic stress strain matrix and its application for the solution of elastic-plastic problems by the finite element method*, Inter. J. Mech. Sci., **10** (1967), p343-354.

[5] Krieg, R.D., and Krieg, D.B., *Accuracies of numerical solution methods for the elastic-perfectly-plastic model*, J. Pressure Vessel Tech., Trans. ASME, **99** (1977), p510-515.

[6] Schreyer, H.L., Kulak, R.F. and Kramer, J.M., *Accurate numerical solution for elastic-plastic model*, J. Pressure Vessel Tech., **101** (1979), p226-234.

[7] Nagtegaal, J.C., *On the implementation of inelastic constitutive equations with special reference to large deformation problems*, Comp. Meth. Appl. Mech. Engng., **33** (1982), p469-484.

[8] Wu, W., *A unified numerical integration formula for the perfectly plastic Von*

Mises model, Inter. J. Numer. Meths Engng., **30** (1990), p491-504.

[9] Marcal, P.V., *A stiffness method for elastic-plastic problems*, Int. J. Mech. Sci., 7 (1969), p229-238.

[10] Rice, J.R. and Tracy, D.M., *Computational fracture mechanics*, in S. J. Fenves (ed.), Numerical and Computer Methods in Structural Mechanics, Academic Press, New York, 1973, p.885.

[11] Wilkins, M.L., *Calculation of elastic-plastic flow*, in B. Alder *et al* (ed.), Methods of Computational Physics, 3, Academic Press, New York, 1964.

[12] Cheng, W., *Large Deformation FEA and Its Application in Metal Forming*, Ph.D Dissertation, McMaster University, Hamilton, Canada, 1994

[13] Bathe, K. J. *Finite Element Procedures in Engineering Analysis*, Prentice-Hall, 1982.

[14] Zienkiewicz, O.C. and Taylor, R.L. *The Finite Element Method*, 4th Edition, McGraw-Hill, 1989.

[15] Rowe, G.W., *et al*, *Finite Element Plasticity and Metal Forming Analysis*, Cambridge University Press, 1991

[16] Nagtegaal, J. C., Parks, D. M. and Rice, J. R. *On numerical accurate finite element solutions in the fully plastic range*, Comput. Meths. Appl. Mech. Engng. 4 (1974), p153-177.

[17] Kikuchi, N. *Remarks on 4CST-elements for imcompressible materials*, Comput. Metths. Appl. Mech. Engng. 37 (1983), p109-123.

[18] Cheng, J. H. and Kikuchi, N. *An analysis of metal forming processes using large deformation elastic-plastic formulations*, Comput. Meths. Appl. Mech. Engng. 49 (1985), p71-108.

[19] Malvern, L.E., *Introduction To the Mechanics of a Continuous Medium*, Prentice-Hall Inc., 1969

CHAPTER 3

Bond Element Technique in Dealing With Friction Boundary Condition

§1 Introduction

To succeed in the numerical analysis of metal forming processes, apart from correct mathematical description or representation of the geometrical nonlinearity and material nonlinearity, which are fundamentals to a successful code, another rather practically demanding feature is contact boundary with friction. In most metal forming processes, the tool side of contact boundary can be assumed to be rigid, and the friction force along the boundary plays a critical role in both physical and numerical processes.

A major difficulty in considering the friction effect lies in that the direction of friction force is related to the direction of metal flow which is not known beforehand. This nature is best demonstrated by the ring compression test, in which the deformation mode of the compressed ring is sensitive to the friction between the tool and ring surface. As shown in Figure 3.1, when friction is low the inner diameter of the ring increases steadily with reduction in height. However, when friction is high, it decreases, although the outer diameter continues to increase.

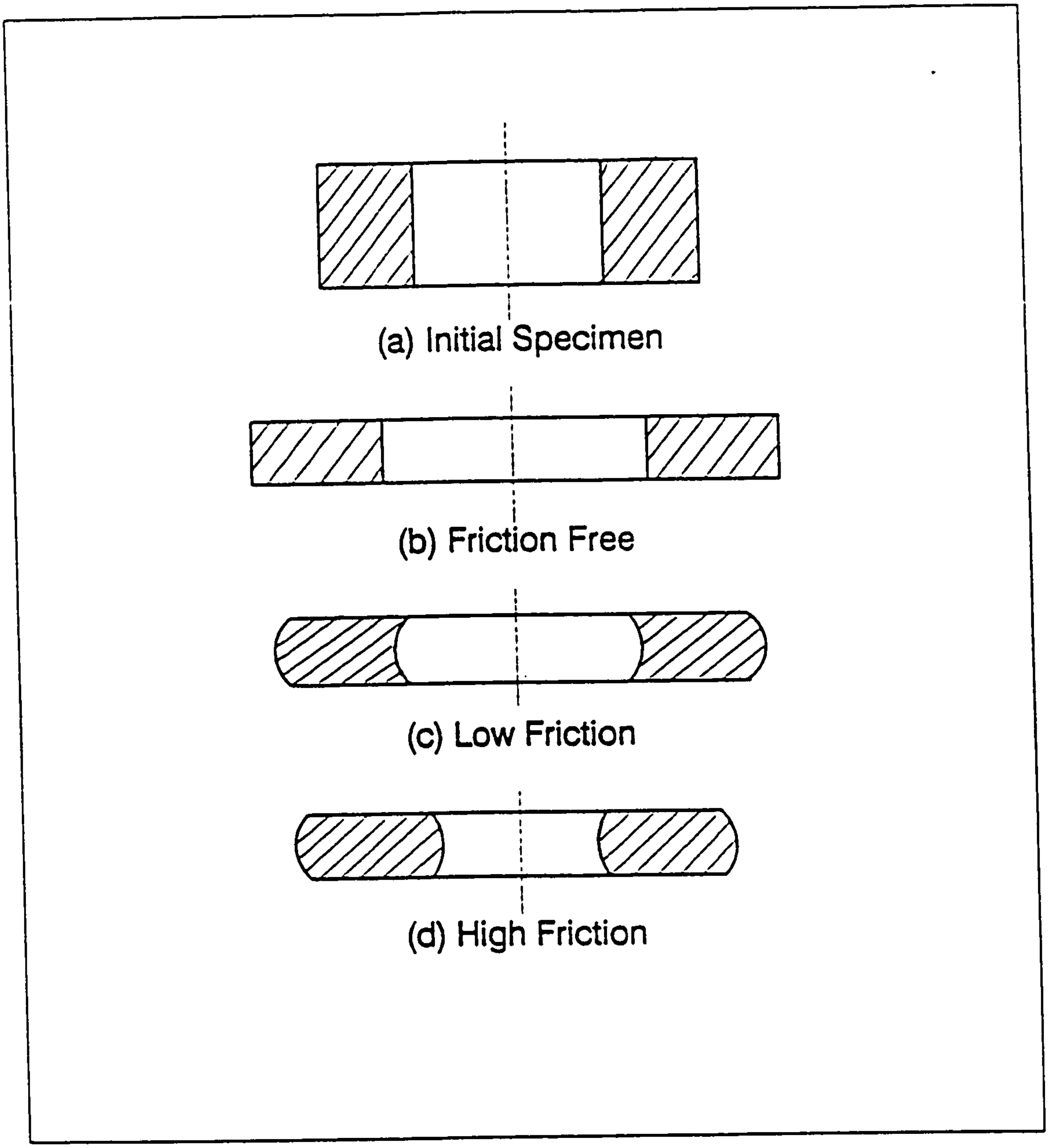

Figure 3.1 Deformation Modes in the Ring Compression Test

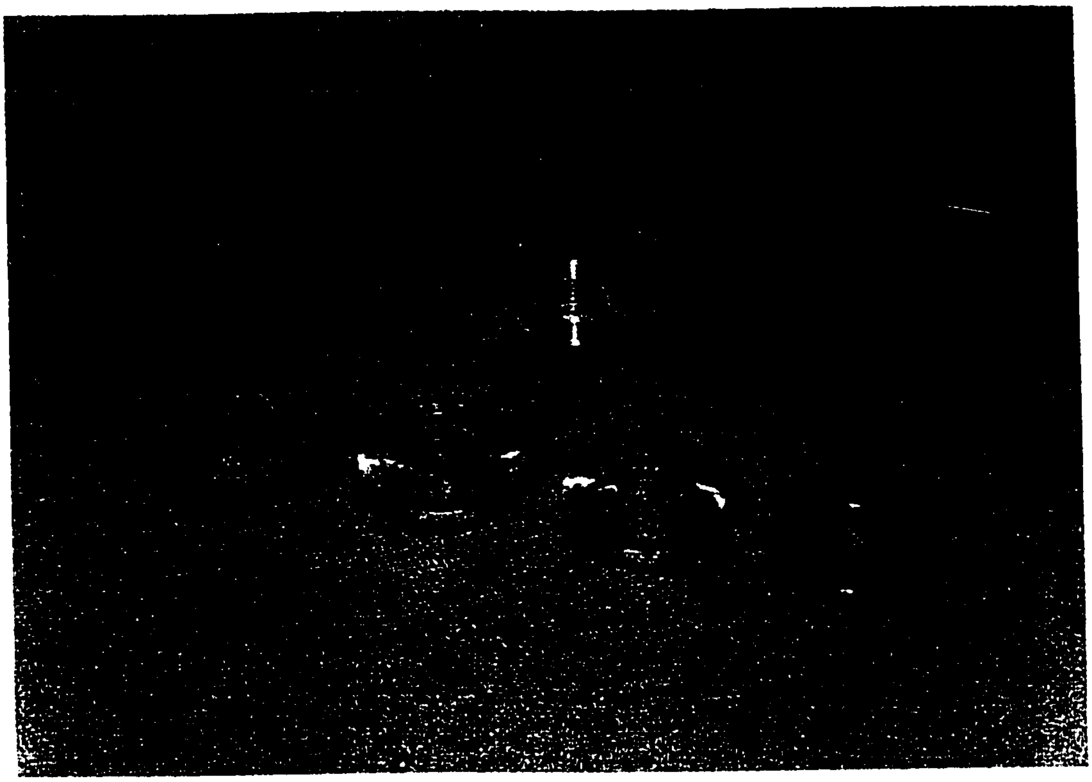

Figure 3.2 Experimentally Compressed Rings

Obviously, this type of boundary condition uncertainty and sensitivity challenges the numerical procedure. The problem has been addressed by several researchers. In 1978, C.C.Chan and Kobayashi ([1]) proposed a variational for rigid plastic formulation to include the friction stress which is dependent on the relative velocity at the die-workpiece interface. A similar approach was generalized by N. Kikuchi (1982,[2]) under the concept of a penalty method to deal with contact boundaries between elastic bodies. Schafer (1975,[3]), and Yamada et al (1979,[4]) proposed a technique using the concept of bond element in dealing with contact problems. All these techniques can be physically interpreted as attaching boundary spring elements between tool and workpiece on their interface.

A numerical technique which is based on the physical instinct rather than mathematics was proposed by P. Hartley et al (1979,[5]) to introduce friction effect into elasto-plastic finite element analysis. The technique has been successfully applied to several other metal forming applications since then (1985,[6] and 1988,[7]).

In this chapter, an incremental form of bond element in tangential directions has been proposed for elasto-plastic formulation. Various numerical aspects on implementing the technique are examined and discussed. To facilitate a better insight of the physical nature of the technique and its influence on the numerical process, the problem is stated in terms of tangential spring.

§2 Fundamentals

As been discussed in Chapter 2, a finite element discretization formulation will end up with an equilibrium equation.

$$[K]\{\delta\} = \{f\} \tag{1}$$

For a nonlinear process such as elasto-plastic analysis, an incremental approach is essential. In each incremental step, the solution is pursued through an incremental form of equilibrium equation

$$[K_T]\{\Delta\delta\} = \{\Delta f\} \tag{2}$$

where $[K_T]$ is the tangential stiffness matrix. It has been a focus for large deformation nonlinear finite element formulations to construct a high-quality and yet low-cost $[K_T]$ to guide solution toward convergence. However, the implementation of modified Newton-Raphson method in the solution process suggests the burden of nonlinearities is actually shared by two parts of the algorithm: one is the formulation of $[K_T]$, the other is the residual force iteration. While $[K_T]$ has to be a good numerical "engine" to drive the solution toward convergence, the residual force evaluation provide feed-back to $[K_T]$ where the solution currently stands. The destination of such a process is to reach an equilibrium state between internal stress and external loading, where the key point is that both internal stress and external load have to be evaluated on the most updated configuration, and in alliance with the assumed nonlinear geometrical, material and frictional relations.

The question here is what kind of ingredient is necessary for $[K_T]$ to achieve good convergency for contact nonlinearity.

§3 A Numerical Example of Ring Compression

To isolate the influence from other nonlinear factors, the calculation is limited in the elastic deformation range.

In this case, to show the effect from friction boundary condition, $[K_T]$ is formulated in a normal way without considering friction. However, in residual force evaluation, we keep updating the external load vector by modifying frictional force based on the updated displacement information on the tool-workpiece interface. In this basically trial and correction way, we hope the solution can eventually converge to a situation in which the internal stress and external load are in equilibrium while the friction stress is in agreement with the specified friction law.

The result is disappointing. It is found that even at very low friction level of m=0.1, the process is difficult to converge. The reason for cases of failure is clear when the friction boundary condition is checked at each iteration. As the theoretical solution suggests, if the boundary condition is started as friction free, then the first iteration will yield a solution where all the tangential displacement along the tool-ring interface is outward (as shown in Figure 3.3a). Therefore the friction stresses on the interface become all inward-pointing for the second iteration, which will overdo the correction and make more nodes than necessary on the interface reverse their displacement directions (as shown in Figure 3.3b). These displacement direction reverse can change the friction condition dramatically. If most of the inward friction force is counter-acted by outward friction force, then the net inward friction force for the third iteration is virtually very small, which may again lead to all outward displacement solution (as shown in Figure 3.3c). Obviously, we are facing an oscillating friction stress solution which converges to nowhere.

So, basically what is observed is that frictional nonlinearity could severely damage the residual force iteration due to the oscillation of friction force direction. To avoid this, $[K_T]$ has to be formulated with an extra consideration of friction effect.

§4 Bond Element

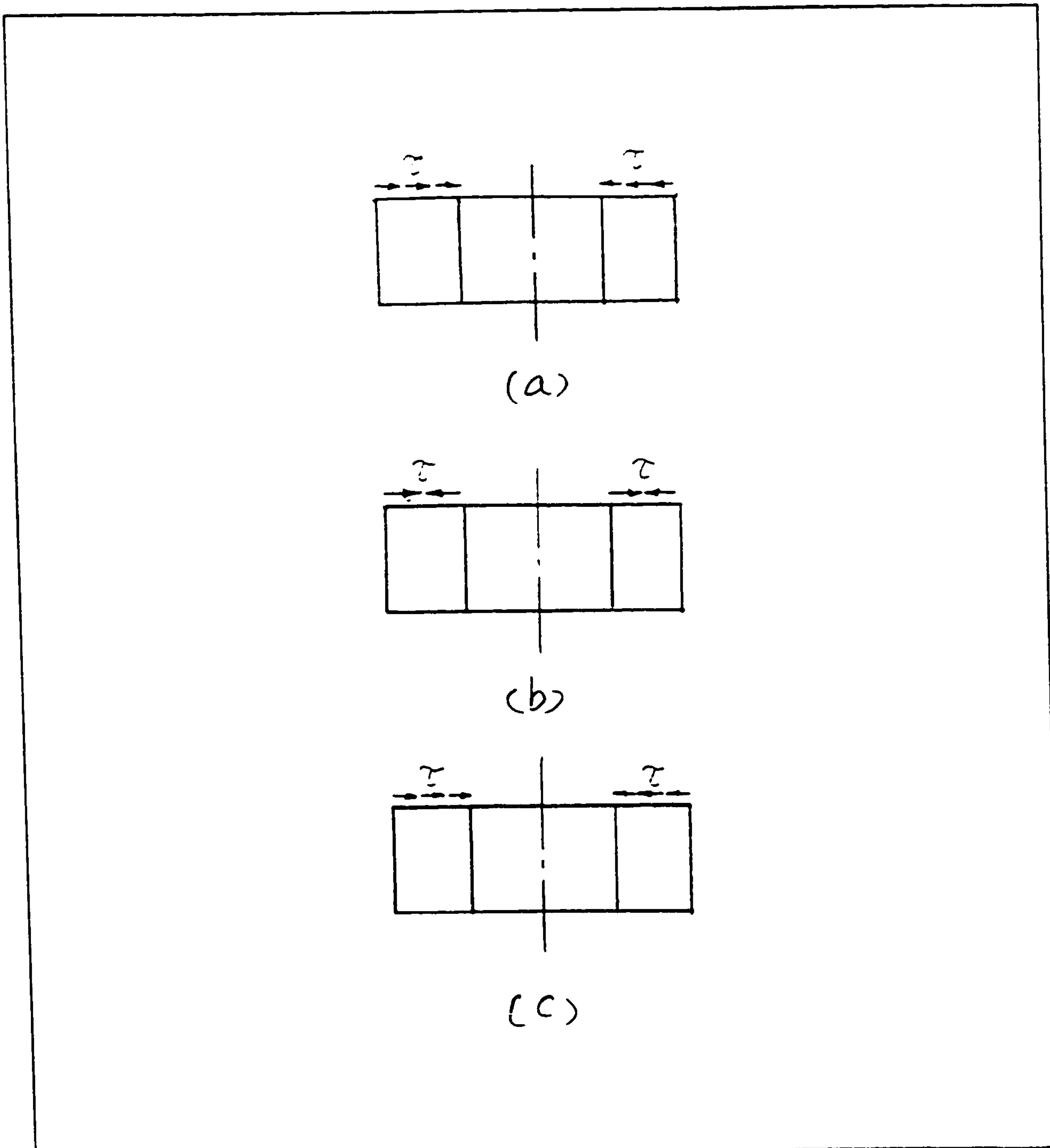

Figure 3.3 Friction Stress Pattern on
(a) 2nd iteration (b) 3rd iteration (c) 4th iteration

A physical interpretation of bond element is shown in Figure 3.4, where the fictitious tangential spring elements are attached between the tool and the workpiece interfaces.

The effect of a tangential spring is characterised in Figure 3.5, where:

B is the node on contact boundary;
k^t_S is the stiffness of tangential spring;
K is the nominal stiffness of workpiece in tangential direction;
Δ_0 is the displacement of neighbouring node;
Δ_B is the displacement of node B;
Δ_S is the relative displacement of the spring ($\Delta_S=\Delta_B$ here).

The purpose of tangential spring is to produce certain amount of resistant force against the motion of node B, and consequently deform body K by an amount of Δ_0-Δ_B. Obviously, the spring force $k^t_S\Delta_S$ has a similar effect with friction force. Final equilibrium solution requires the internal force $K(\Delta_0-\Delta_B)$ be equal to a prescribed friction force, to meet this goal, there are two ways:

1) choose right k^t_S to make $k^t_S\Delta_S=K(\Delta_0-\Delta_B)=F_\tau$

2) put an additional external force F_B on node B to achieve an effect of $K(\Delta_0-\Delta_B) = k^t_S\Delta_S+ F_B= F_\tau$. This procedure can be handily fitted into the residual force iteration.

A practical procedure is the combination of the two choices. Due to the nonlinear nature of the process, a perfect completion of choice (1) is impossible. However, an even partially fulfilled (1) will enhance the ability of $[K_T]$ to handle the nonlinearity of friction boundary condition. The rest of error is left for choice (2) to correct. Numerical practice demonstrates this method is very effective in dealing with the problem at a fractional

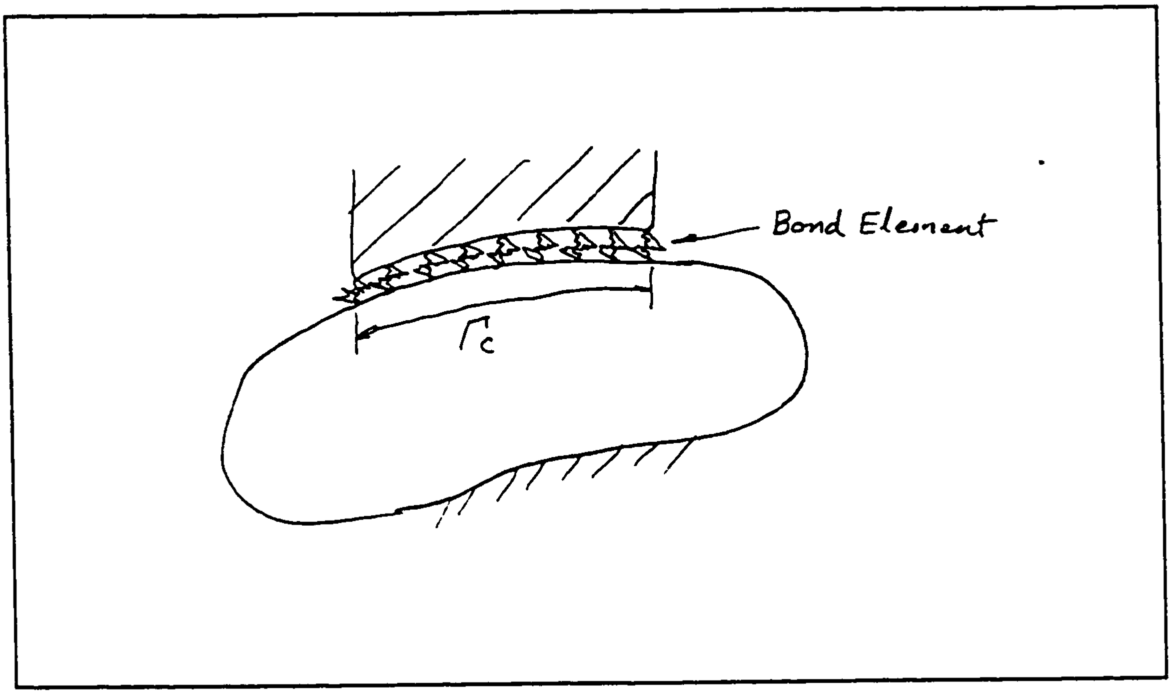

Figure 3.4 The Physical Interpretation of a Bond Element

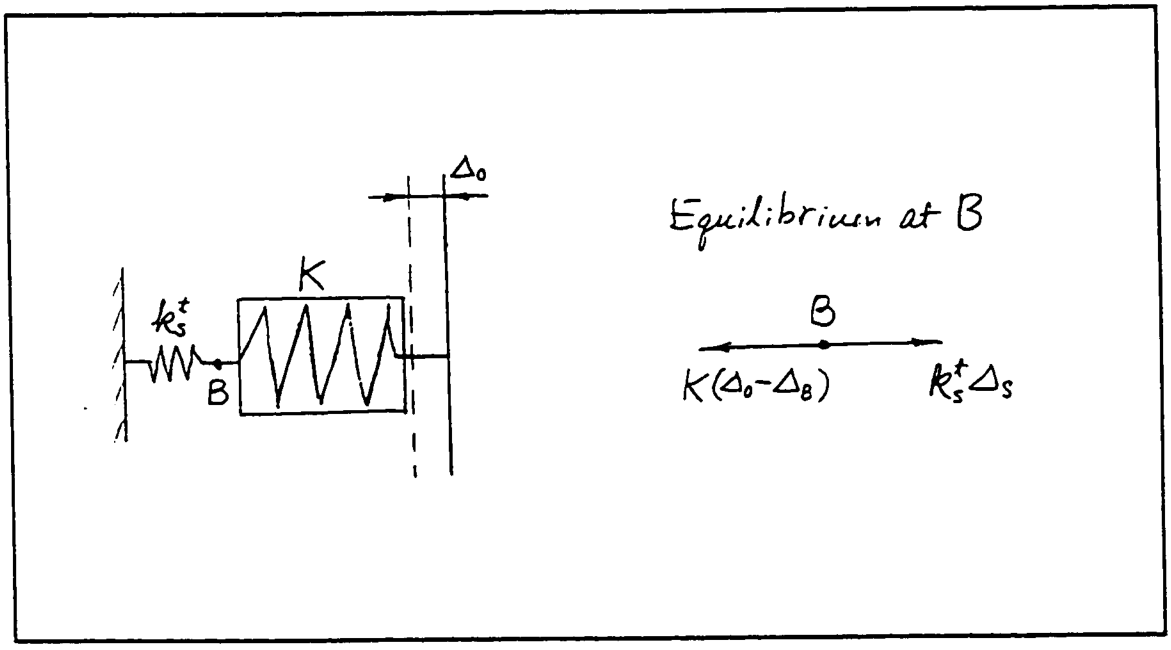

Figure 3.5 The Effect of a Tangential Spring Element

numerical cost.

§5 Formulation

The formulation of tangential spring bond element contribution into the main element stiffness matrix is straightforward.

As shown in Figure 3.6, the application of virtual work principle on the sample element yield:

$$\begin{aligned}\{F\}^e &= \int_{\Omega^e}[B]^T\{\sigma\}d\Omega + \int_{\Gamma}[N]^T[k_S][N](\{u\}^e - \{u_o\}^e)d\Gamma \\ &= ([K_T] + [K_S])\{u\}^e - [K_S]\{u_o\}^e\end{aligned} \tag{3}$$

where

$\{u\}^e$ is the nodal displacement of the element;

$\{u_o\}^e$ is the nodal displacement of tool surface;

$\{F\}^e$ is the external loading force vector;

$[K_T]$ is the ordinary tangential stiffness matrix;

and

$$[K_S] = \int_{\Gamma}[N]^T\begin{bmatrix} k_s^n & 0 \\ 0 & k_s^t \end{bmatrix}[N]\,d\Gamma \tag{4}$$

is the contribution matrix from the bond element.

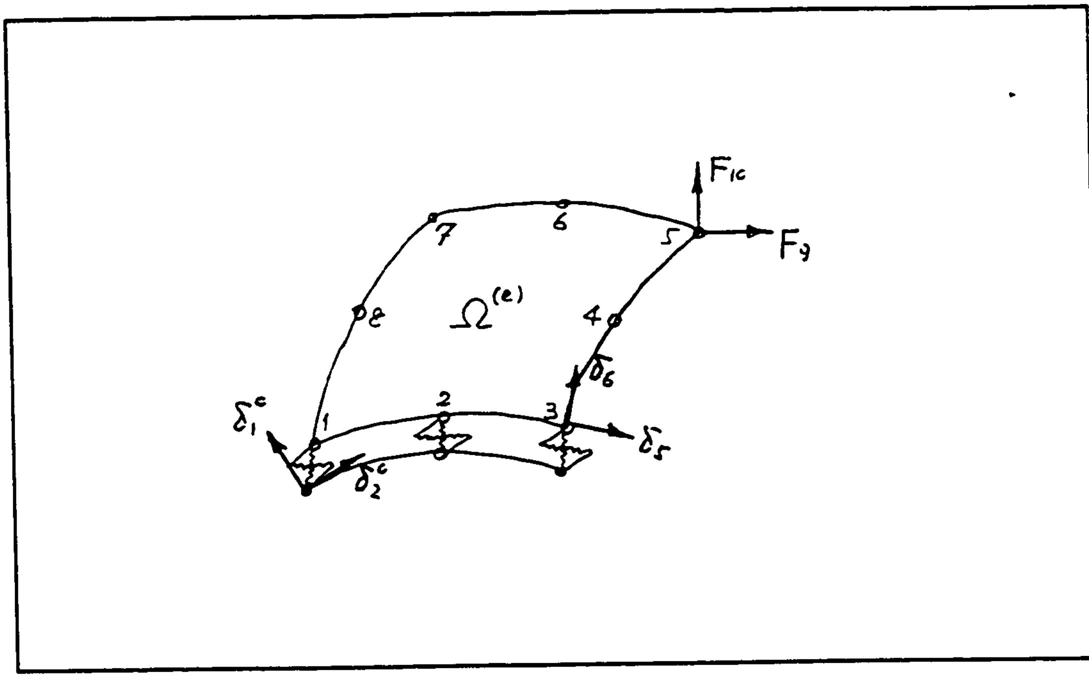

Figure 3.6 The Elementary Formulation of Bond Element

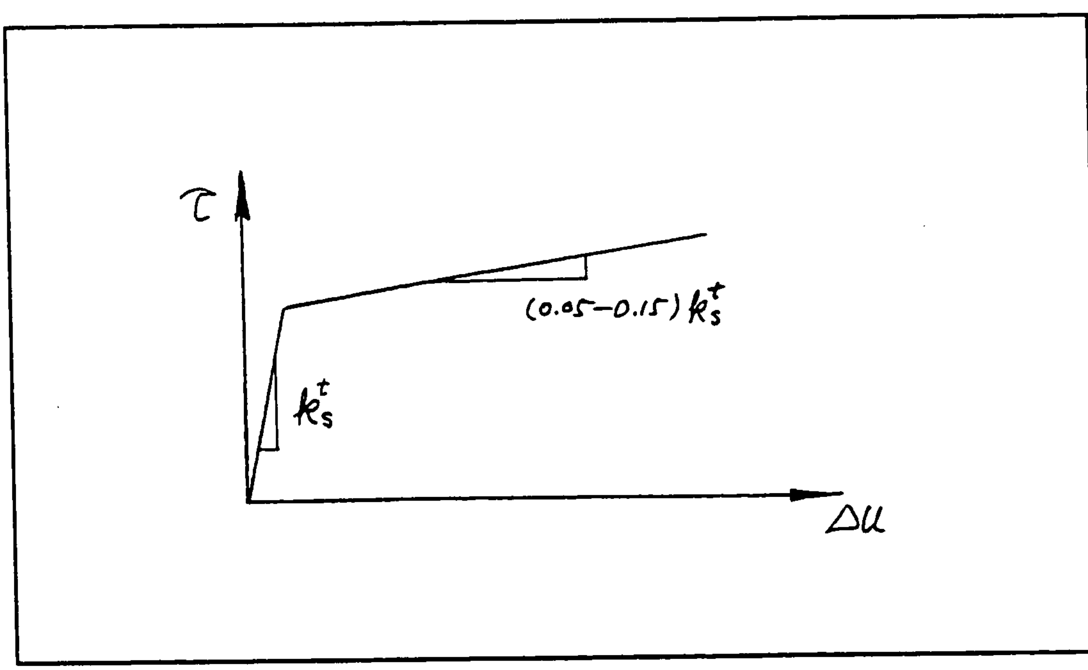

Figure 3.7 $\tau-\Delta u$ curve

The final form of the elementary equilibrium equation is

$$\{F^*\}^e = [K_T^*]\{u\}^e \tag{5}$$

where

$\{F^*\} = \{F\}^e + [K_S]\{u_o\}^e$ is the pseudo external force vector;

$[K_T^*] = [K_T] + [K_S]$ is the new tangential stiffness matrix.

The determination of k_S^t is based on the assumptueous $\tau-\Delta u$ curve. For example, two most accepted friction model in metal forming are Coulumb $\tau=\mu p_n$ and the constant shear stress $\tau=mk$. They share similar $\tau-\Delta u$ curves (as shown in Figure 3.7). The initial k_S^t is determined in such a manner that the friction stress is fully exerted on the interface after the first increment load. Afterward, k_S^t should be considerably softened, because the friction stress needs only to be adjusted according to the increase of p_n or k.

Again, an accurate number of k_S^t is not pursued. The purpose of k_S^t is to build stabilizing components into $[K_T]$, a desired stress solution can only be accomplished through residual force iteration. In this study, a softening factor of 0.05-0.15 is used after the first loading increment.

§6 Numerical Results

A standard ring (with a ratio of 6:3:2 for outer diameter, inner diameter and height) test is simulated under different friction condition. As been mentioned in [11], the numerical process failed to converge when friction coefficient m>0.3 without using bond element technique.

Based on the symmetry of the structure, a quarter of the ring is meshed by 5X10 4CST elements. The mechanical properties specified are as follows: Young's modulus E=200 kN/mm^2, Poisson's ratio $\nu = 0.3$, initial yield strength $\sigma_Y = 0.7$ kN/mm^2, strain hardening $H' = 0.3$ kN/mm^2.

Numerical stability is achieved at all friction levels tested. Figure 3.8-3.12 show the simulation results at different friction levels. All deformation modes mentioned in Figure 3.1 have been demonstrated.

Figure 3.13 gives the friction coefficient calibration curves based on the results from the cases shown in Figure 3.8-3.12. They are well comparable with published experimental and numerical results[5,8-10].

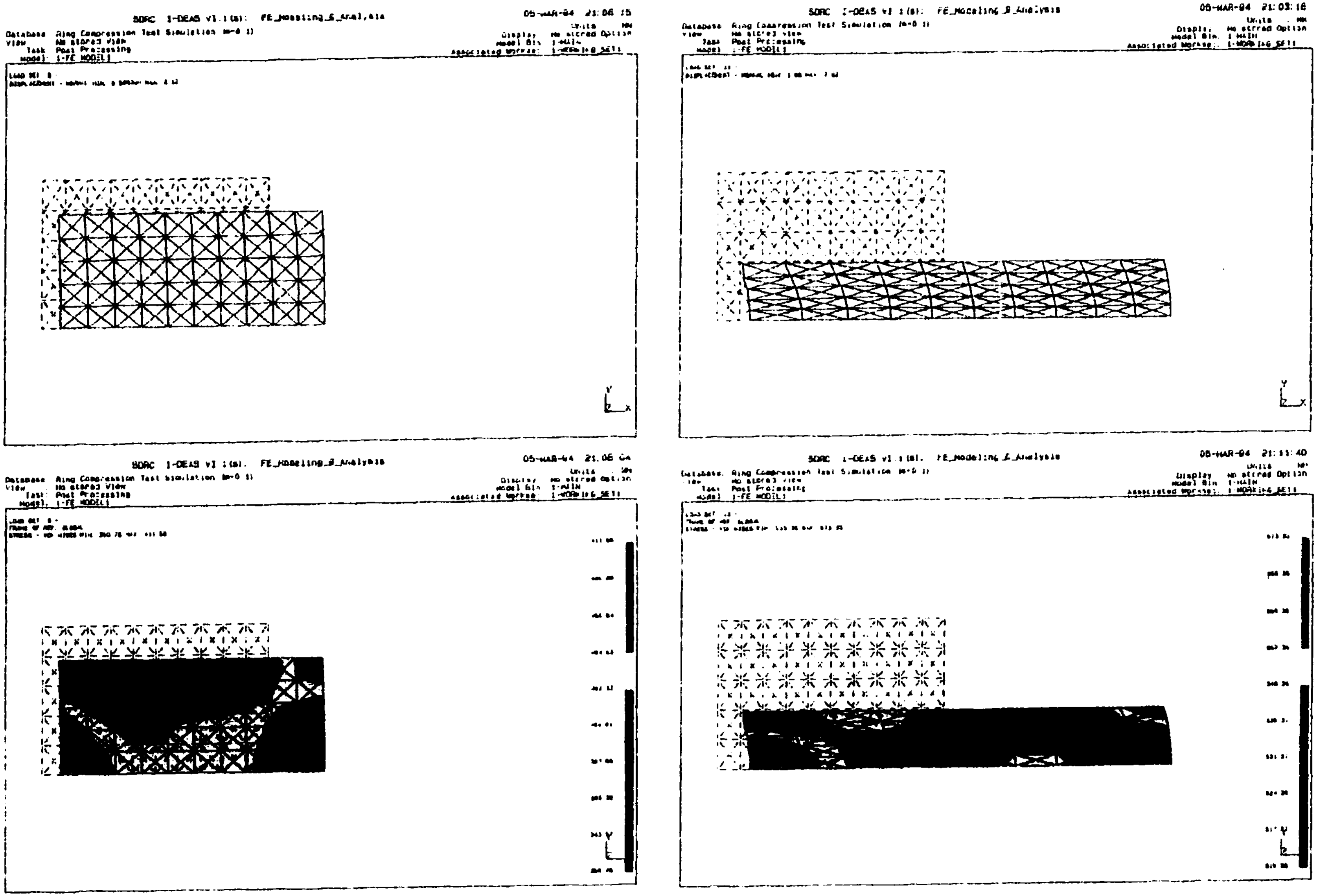

Figure 3.8 Simulation of Ring Compression Test at m=0.1

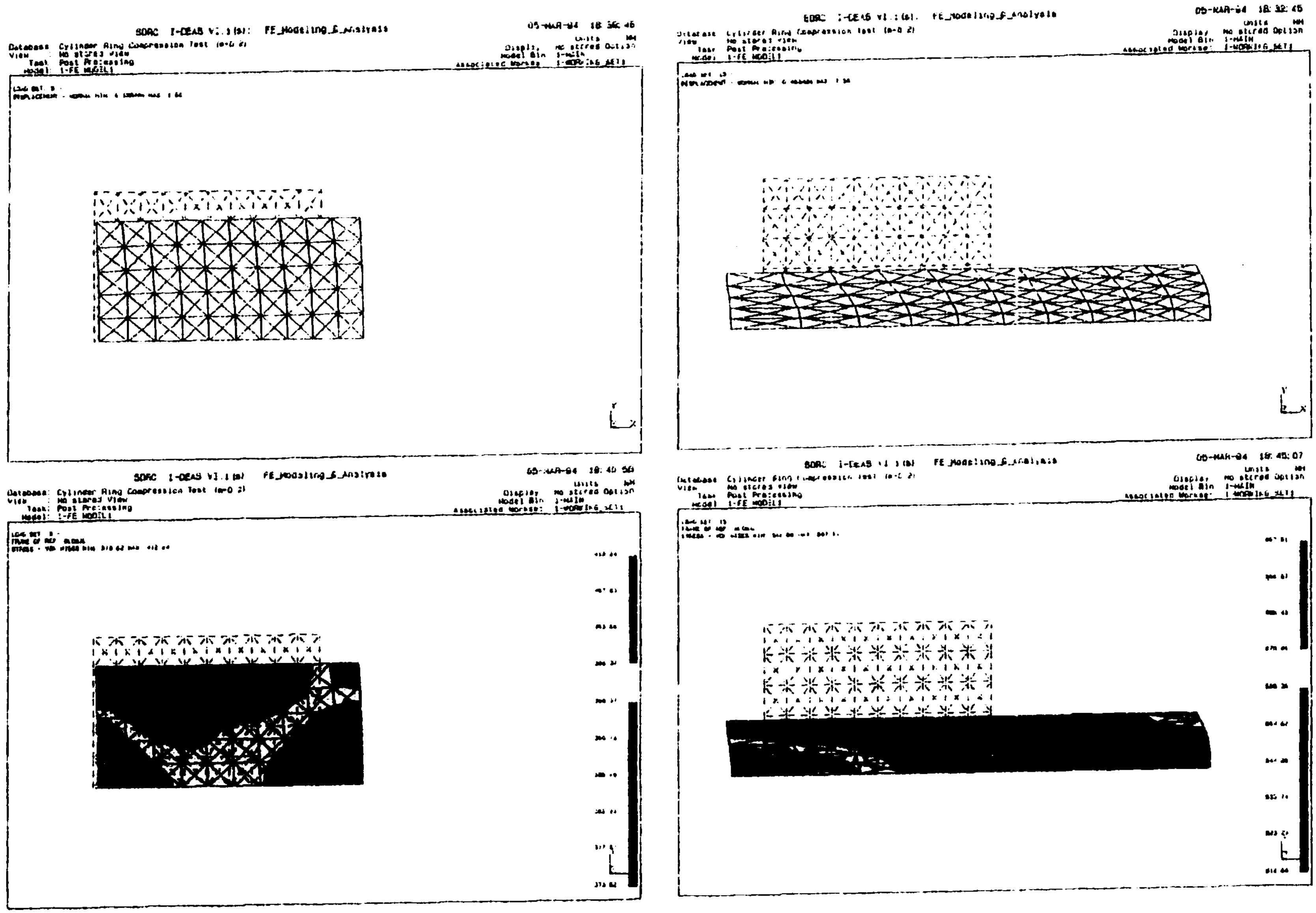

Figure 3.9 Simulation of Ring Compression Test at m=0.2

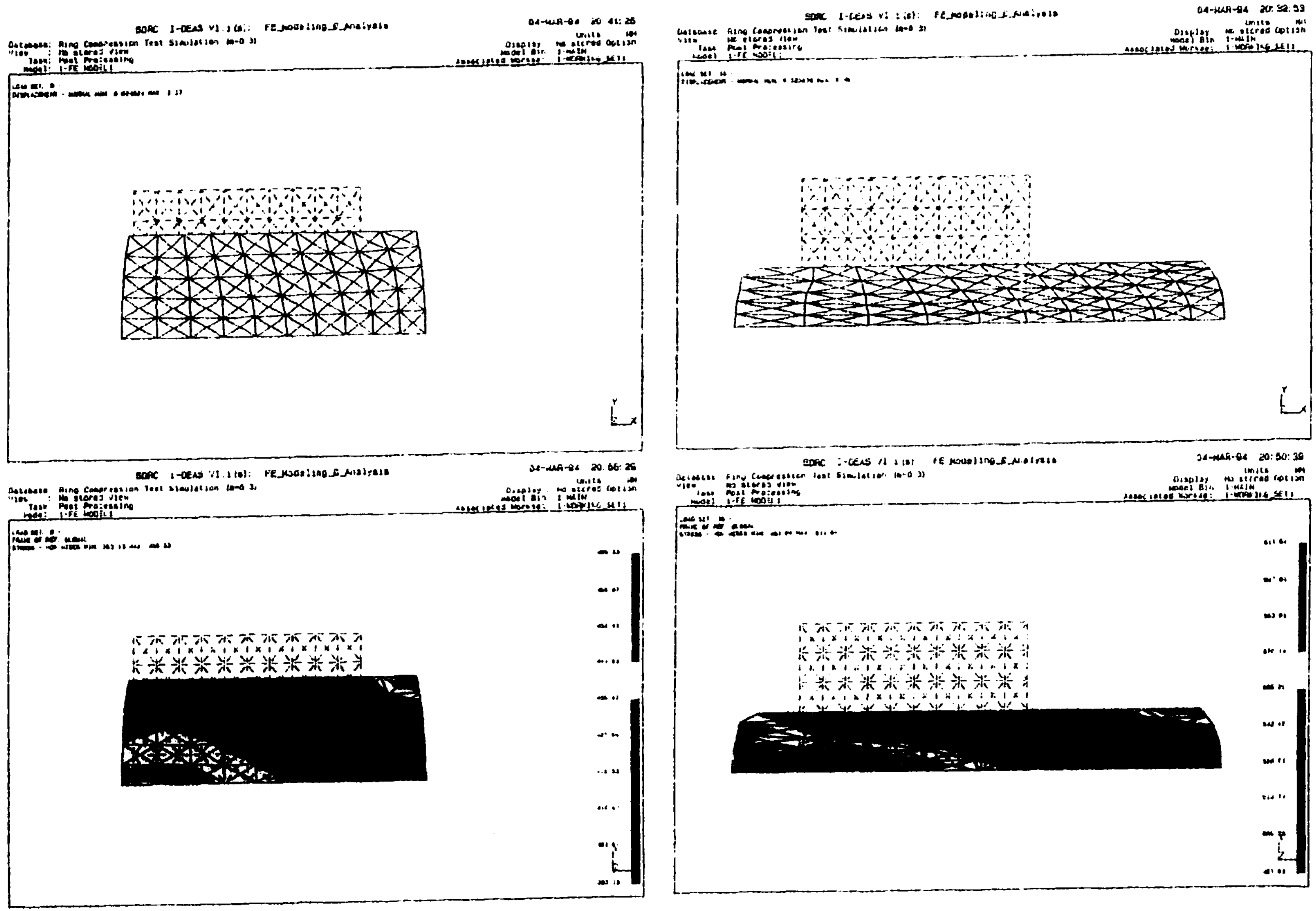

Figure 3.10 Simulation of Ring Compression Test at m=0.3

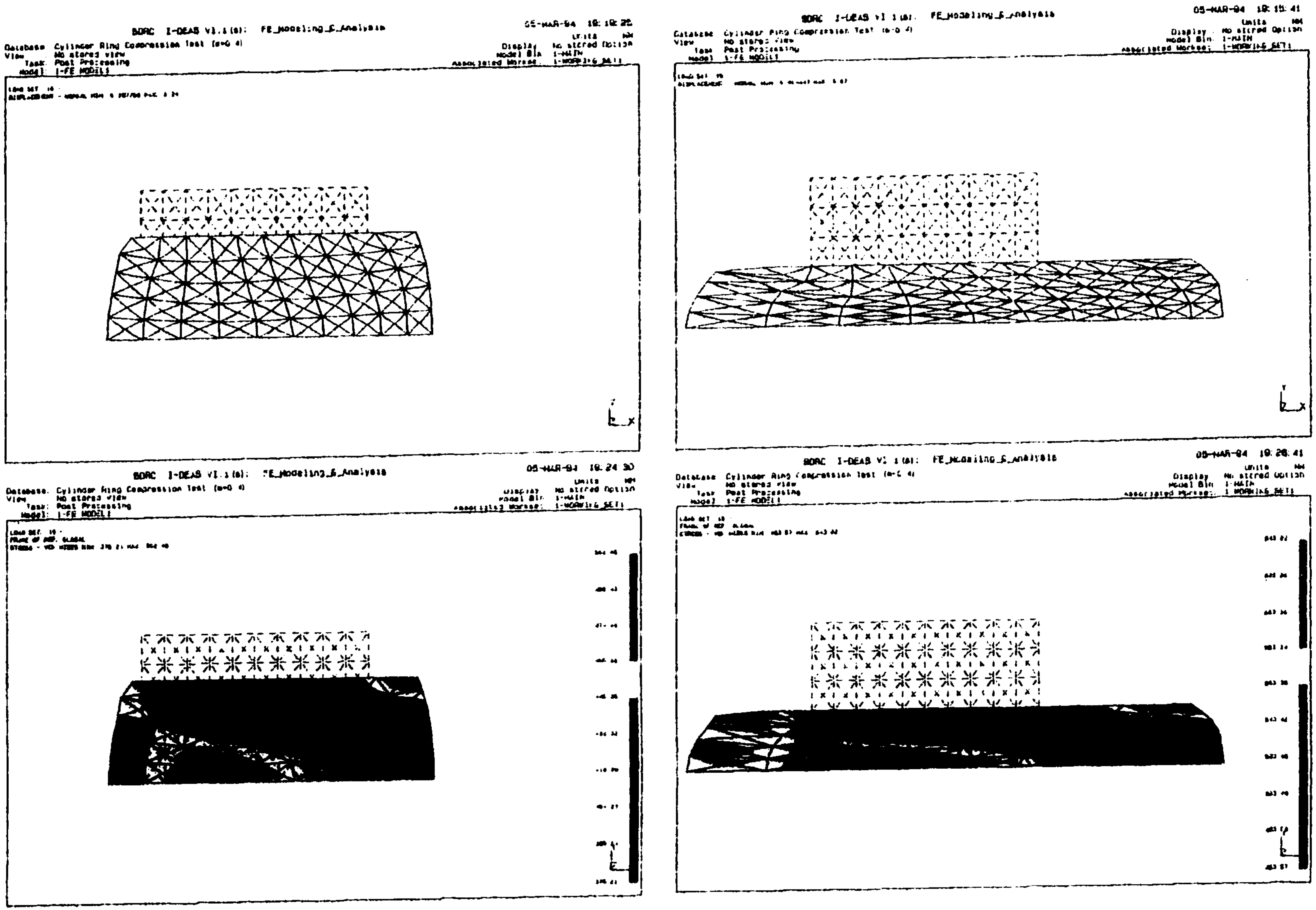

Figure 3.11 Simulation of Ring Compression Test at m=0.4

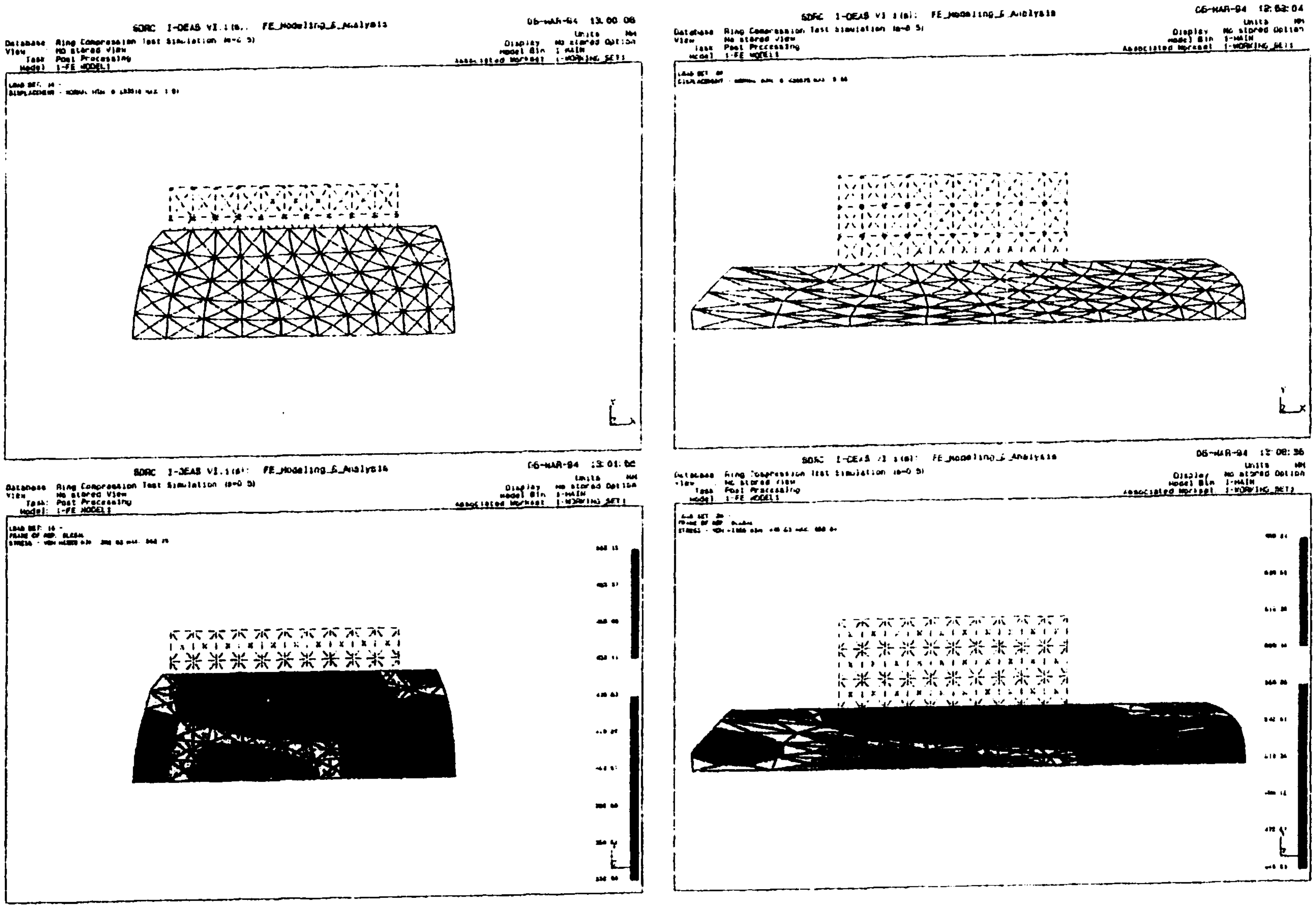

Figure 3.12 Simulation of Ring Compression Test at m=0.5

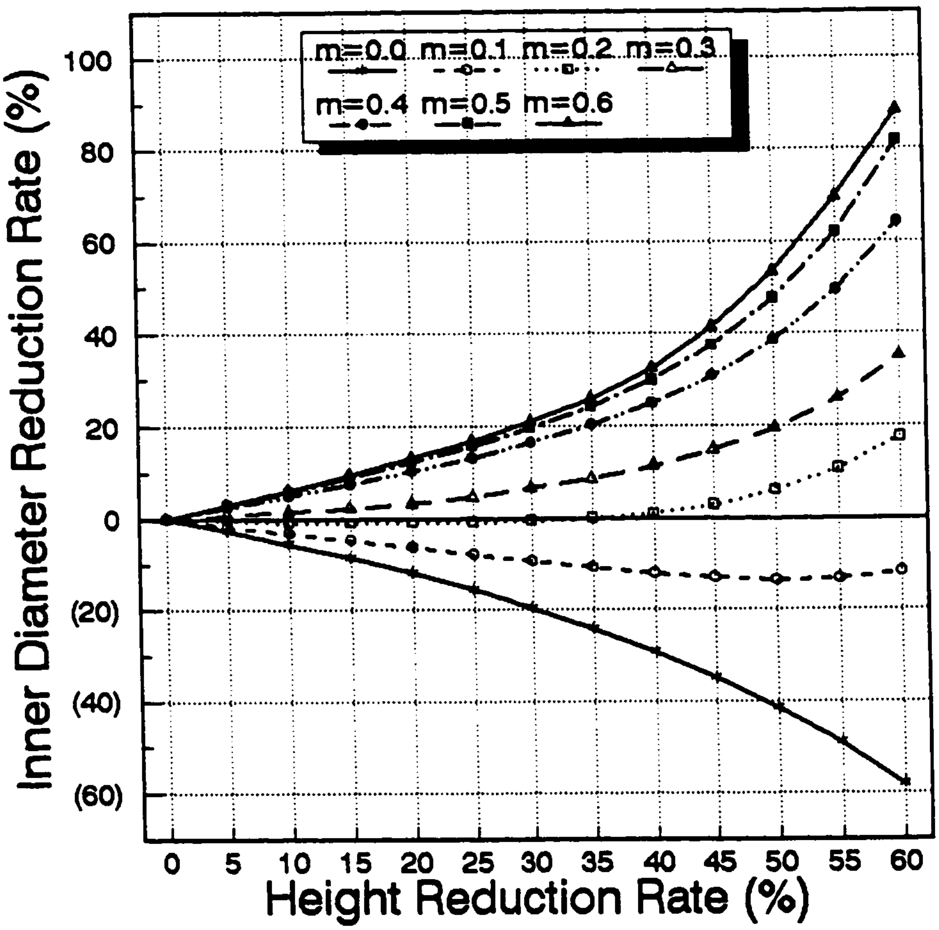

Figure 3.13 The Calculated Friction Calibration Curves

§7 Reference

[1] Chen, C.C. and Kobayashi, S., *Rigid Plastic Finite Element Analysis of Ring Compression*, ASME-AMD, 1978, Vol.28, 163-174

[2] Kikuchi, N., *Penalty/Finite Element approximations of A Class of Unilateral Contact Problems*, in: J.N. Reddy eds. Penalty Method in Finite Element Methods. ASME, 1982, 87-108

[3] Schäfer, H., *A Contribution to The Solution of Contact Problems with The Aid of Bond Elements*, Comput. Meths. Appl. Mech. Engng., 1975, Vol.6, 335-354

[4] Yamada, Y. et al, *Handy Incorporation of Bond and Singular Elements in Finite Element Solution Routine*, Trans. 5th Internat. Conf. on SMIRT, 1979

[5] Hartley, P., et al, *Friction in Finite Element Analysises of Metalforming Processes*, Int. J. Mech. Sci., 1979, Vol.21, 301-311

[6] Liu, C., et al, *Elastic-Plastic Finite Element Modelling of Cold Rolling of Strip*, Int. J. Mech. Sci., 1985, Vol.27, 531-541

[7] Liu, C., et al, *Analysis of Stress and Strain Distributions in Slab Rolling Using an Elastic-Plastic Finite Element Method*, Int. J. Numer. Meths. Engng., 1988, Vol.25, 55-66

[8] Avitzur, B., *Forging of hollow discs*, Israel J. Tech., **2** (1964), p295-304.

[9] Male A.T., *Variations in friction coefficients of metals during compressive*

deformation, J. Inst. of Metals, **94** (1966), p121-125.

[10] Male A.T. and DePierre V., *The validity of mathematical solutions for determining friction from the ring compression test*, J. Lubrication Tech., Trans. ASME, **92** (1970), p389-397.

[11] Cheng Wan, *Large Deformation FEA and its Applications in Metal Forming Processes*, M. Eng. Desertation, McMaster University, 1991

CHAPTER 4

A Large Deformation Shell Element Formulation And Its Application in Sheet metal Stamping

§1 Introduction

A 3D degenerated shell element formulation is presented based on the consistent large deformation formulation presented in Chapter 2. A special penalty method is devised to enforce the Kirchhoff constraint which has been missing in the degenerated shell element discretization. The method has successfully prevented a variety of elements from shear locking. Simulating and analyzing sheet metal stamping process have been the purpose of this research. Results for simulating square cup deep drawing are presented and discussed in this chapter.

§2 Basic Concepts in 3D Curvilinear Coordinates

§2-1 Geometrical Description

As is always assumed, the coordinate transformation is given in the form of

$$\bar{x} = \bar{x}(\xi,\eta,\zeta) = x_k(\xi,\eta,\zeta)\,\bar{e}_k$$

Then, we have:

(1) Covariant Base vectors

The covariant base vectors of the curvilinear coordinate are defined as

$$\bar{g}_i = \frac{\partial \bar{x}}{\partial \xi_i} = x_{j,\xi_i}\,\bar{e}_j \qquad i.e. \qquad \begin{Bmatrix} \bar{g}_1 \\ \bar{g}_2 \\ \bar{g}_3 \end{Bmatrix} = \begin{bmatrix} x_{1,\xi} & x_{2,\xi} & x_{3,\xi} \\ x_{1,\eta} & x_{2,\eta} & x_{3,\eta} \\ x_{1,\zeta} & x_{2,\zeta} & x_{3,\zeta} \end{bmatrix} \begin{Bmatrix} \bar{e}_1 \\ \bar{e}_2 \\ \bar{e}_3 \end{Bmatrix} = [J] \begin{Bmatrix} \bar{e}_1 \\ \bar{e}_2 \\ \bar{e}_3 \end{Bmatrix} \tag{1}$$

where [J] represents the Jacobian matrix which transforms the global Cartesian base vectors $\{e_j\}$ into the covariant base vectors $\{g_i\}$ in the equation.

(2) Metric Tensor

The contravariant components of the metric tensor is given by

$$g_{ij} = \bar{g}_i \bullet \bar{g}_j = x_{k,\xi_i} x_{k,\xi_j} \qquad i.e. \qquad \left[g_{ij}\right]_{3\times3} = [J][J]^T \tag{2}$$

and the covariant component of the metric tensor is therefore given by

$$\left[g^{ij}\right]_{3\times3} = \left[g_{ij}\right]^{-1}_{3\times3} = [J]^{-T}[J]^{-1} \tag{3}$$

(3) Contravariant Base Vectors

Using $[g^{ij}]_{3X3}$, the contravariant base vectors can be obtained as

$$\begin{Bmatrix} \bar{g}^1 \\ \bar{g}^2 \\ \bar{g}^3 \end{Bmatrix} = [g^{ij}]_{3\times 3} \begin{Bmatrix} \bar{g}_1 \\ \bar{g}_2 \\ \bar{g}_3 \end{Bmatrix} = [J]^{-T}[J]^{-1} \begin{Bmatrix} \bar{g}_1 \\ \bar{g}_2 \\ \bar{g}_3 \end{Bmatrix} \tag{4}$$

(4) Transformation between different base sets

Based on Equation (1)-(4), following relations can be built up

$$\begin{Bmatrix} \bar{g}^1 \\ \bar{g}^2 \\ \bar{g}^3 \end{Bmatrix} = [J]^{-T} \begin{Bmatrix} \bar{e}_1 \\ \bar{e}_2 \\ \bar{e}_3 \end{Bmatrix} \tag{5}$$

$$\begin{Bmatrix} \bar{e}_1 \\ \bar{e}_2 \\ \bar{e}_3 \end{Bmatrix} = [J]^{-1} \begin{Bmatrix} \bar{g}_1 \\ \bar{g}_2 \\ \bar{g}_3 \end{Bmatrix} = [J]^{T} \begin{Bmatrix} \bar{g}^1 \\ \bar{g}^2 \\ \bar{g}^3 \end{Bmatrix} \tag{6}$$

$$\begin{Bmatrix} \bar{g}_1 \\ \bar{g}_2 \\ \bar{g}_3 \end{Bmatrix} = [g_{ij}]_{3\times 3} \begin{Bmatrix} \bar{g}^1 \\ \bar{g}^2 \\ \bar{g}^3 \end{Bmatrix} = [J][J]^{T} \begin{Bmatrix} \bar{g}^1 \\ \bar{g}^2 \\ \bar{g}^3 \end{Bmatrix} \tag{7}$$

§2-2 Different Expressions for Displacement Gradient Tensor **u** in Curvilinear Coordinates

In curvilinear coordinate, displacement vector $\bar{\mathbf{u}}$ is often presented as

$$\bar{u} = \bar{u}(\xi,\eta,\zeta) = u_k(\xi,\eta,\zeta)\,\bar{e}_k$$

Therefore

$$\bar{\bar{u}} = \frac{\partial \bar{u}}{\partial \bar{x}} = \left(\bar{g}^i \frac{\partial}{\partial \xi_i}\right)\left(u_j \bar{e}_j\right) = \bar{g}^i \frac{\partial u_j}{\partial \xi_i}\bar{e}_j = \left\{\bar{g}^1\ \bar{g}^2\ \bar{g}^3\right\}\begin{bmatrix} u_{1,\xi} & u_{2,\xi} & u_{3,\xi} \\ u_{1,\eta} & u_{2,\eta} & u_{3,\eta} \\ u_{1,\zeta} & u_{2,\zeta} & u_{3,\zeta} \end{bmatrix}\begin{Bmatrix} \bar{e}_1 \\ \bar{e}_2 \\ \bar{e}_3 \end{Bmatrix} \qquad (8)$$

Using relations listed in §2-1, it is straightforward to resolve **u** in different frames:

(1) <u>In Cartesian Frame</u> $\{e_i\}$

$$\bar{\bar{u}} = u_{ij}\bar{e}_i\bar{e}_j = \left(\bar{e}_1\ \bar{e}_2\ \bar{e}_3\right)[J]^{-1}\left[\frac{\partial u_j}{\partial \xi_i}\right]_{3\times 3}\begin{Bmatrix} \bar{e}_1 \\ \bar{e}_2 \\ \bar{e}_3 \end{Bmatrix} \quad or \quad \left[u_{ij}\right] = \left[\frac{\partial u_j}{\partial x_i}\right] = [J]^{-1}\left[\frac{\partial u_j}{\partial \xi_i}\right] \qquad (9)$$

(2) <u>In Contravariant Frame</u> $\{g^\alpha\}$

$$\bar{\bar{u}} = u_{\alpha\beta}\bar{g}^{\alpha}\bar{g}^{\beta} = \left(\bar{g}^1\ \bar{g}^2\ \bar{g}^3\right)\left[\frac{\partial u_j}{\partial \xi_i}\right][J]^T\begin{Bmatrix}\bar{g}^1\\ \bar{g}^2\\ \bar{g}^3\end{Bmatrix} = \left(\bar{g}^1\ \bar{g}^2\ \bar{g}^3\right)\begin{bmatrix}\bar{u}_{,\xi}\\ \bar{u}_{,\eta}\\ \bar{u}_{,\zeta}\end{bmatrix}\bullet\left[\bar{x}_{,\xi}\ \bar{x}_{,\eta}\ \bar{x}_{,\zeta}\right]\begin{Bmatrix}\bar{g}^1\\ \bar{g}^2\\ \bar{g}^3\end{Bmatrix} \quad (10a)$$

That is

$$u_{\alpha\beta} = \bar{u}_{,\xi_\alpha}\bullet\bar{x}_{,\xi_\beta} = \frac{\partial\bar{u}}{\partial\xi_\alpha}\bullet\bar{g}_\beta \quad (10b)$$

which is the most commonly cited expression due to its simplicity and explicitness. However, $u_{\alpha\beta}$ is hardly a good choice in physical sense because $\{g^{\alpha}\}$ is usually not illustrative in presenting shell geometry.

(3) <u>In Covariant Frame</u> $\{g_\alpha\}$

$$\bar{\bar{u}} = u^{\alpha\beta}\bar{g}_\alpha\bar{g}_\beta = \left\{\bar{g}_1\ \bar{g}_2\ \bar{g}_3\right\}\left[g^{ij}\right]\begin{bmatrix}u_{1,\xi}\ u_{2,\xi}\ u_{3,\xi}\\ u_{1,\eta}\ u_{2,\eta}\ u_{3,\eta}\\ u_{1,\zeta}\ u_{2,\zeta}\ u_{3,\zeta}\end{bmatrix}\left[J\right]^{-1}\begin{Bmatrix}\bar{g}_1\\ \bar{g}_2\\ \bar{g}_3\end{Bmatrix} \quad (11)$$

$$i.e. \quad \left[u^{\alpha\beta}\right]_{3\times3} = \left[g^{ij}\right]_{3\times3}\left[\frac{\partial u_j}{\partial\xi_i}\right]_{3\times3}\left[J\right]^{-1}_{3\times3} = \left[g^{ij}\right]_{3\times3}\left[u_{\alpha\beta}\right]_{3\times3}\left[g^{ij}\right]_{3\times3}$$

Since g_1 and g_2 are tangential vectors of shell surface, $u^{\alpha\beta}$ are better components physically, though mathematically more complex.

§3 Ahmad Degenerated Shell Elements

Thin-shelled structure analysis using shell elements is important task of finite element research because of its large industrial application. Since it was introduced in 1970 by Ahmad[1], the degenerated shell element approach has received continued popularity because of its generality, simplicity and efficiency. Its major advantage has been the independence of any particular shell theory.

Employing the similar assumptions used for Mindlin plate elements:

(1) "Normal" to the middle surface before deformation remain straight after deformation;

(2) The normal stress component perpendicular to the mid-surface is neglected.

Ahmad degenerated a 3D brick element to a general curved shell element which has nodes only at the mid-surface. As a result of the simplification, deformation variations in the thickness direction of the shell are simply represented by two rotation angles of the shell "normal" vector (Figure 4.1).

§3-1 Coordinate Systems

There are four coordinate systems used in degenerated shell element formulation (see Figure 4.2). They are defined as follows.

(1) *Global Cartesian Coordinate System (x,y,z)*:

This system is used to define nodal coordinates and displacements, as well as the global stiffness matrix and applied force vectors.

(2) *Curvilinear Coordinate System* (ξ, η, ζ):

As will be shown in the next section, variables (ξ, η, ζ) in the isoparametric shape functions are naturally chosen as the curvilinear coordinates. The mid-surface of the shell element is defined by ξ and η. It is assumed that ξ, η and ζ vary between -1 and +1 on the respective faces of the element, depending on the type of element used.

(3) *Local Convected Cartesian Coordinate System (x', y', z'):*

This system is designed to define a local Cartesian frame at any point within the shell element to reveal the in-plane and transverse physical components of the local stress and strain tensors. The definition of such a frame is as follows:

The unit vector e_1' in the x' direction is taken to coincide with the tangent to the ξ direction, so that

$$\bar{e}_1' = \frac{\dfrac{\partial \bar{x}}{\partial \xi}}{\left\| \dfrac{\partial \bar{x}}{\partial \xi} \right\|} = \frac{\bar{g}_1}{\left\| \bar{g}_1 \right\|}$$

The unit vector e_3' in the z' direction is taken to be normal to the surface ζ=*constant*, so that

$$\bar{e}_3' = \frac{\dfrac{\partial \bar{x}}{\partial \xi} \times \dfrac{\partial \bar{x}}{\partial \eta}}{\left\| \dfrac{\partial \bar{x}}{\partial \xi} \times \dfrac{\partial \bar{x}}{\partial \eta} \right\|} = \frac{\bar{g}_1 \times \bar{g}_2}{\left\| \bar{g}_1 \times \bar{g}_2 \right\|}$$

Then, the unit vector e_2' in the y' direction is obtained by the cross product of e_3' and e_1' so that $\{e_i'\}$ form a right hand orthonormal base set:

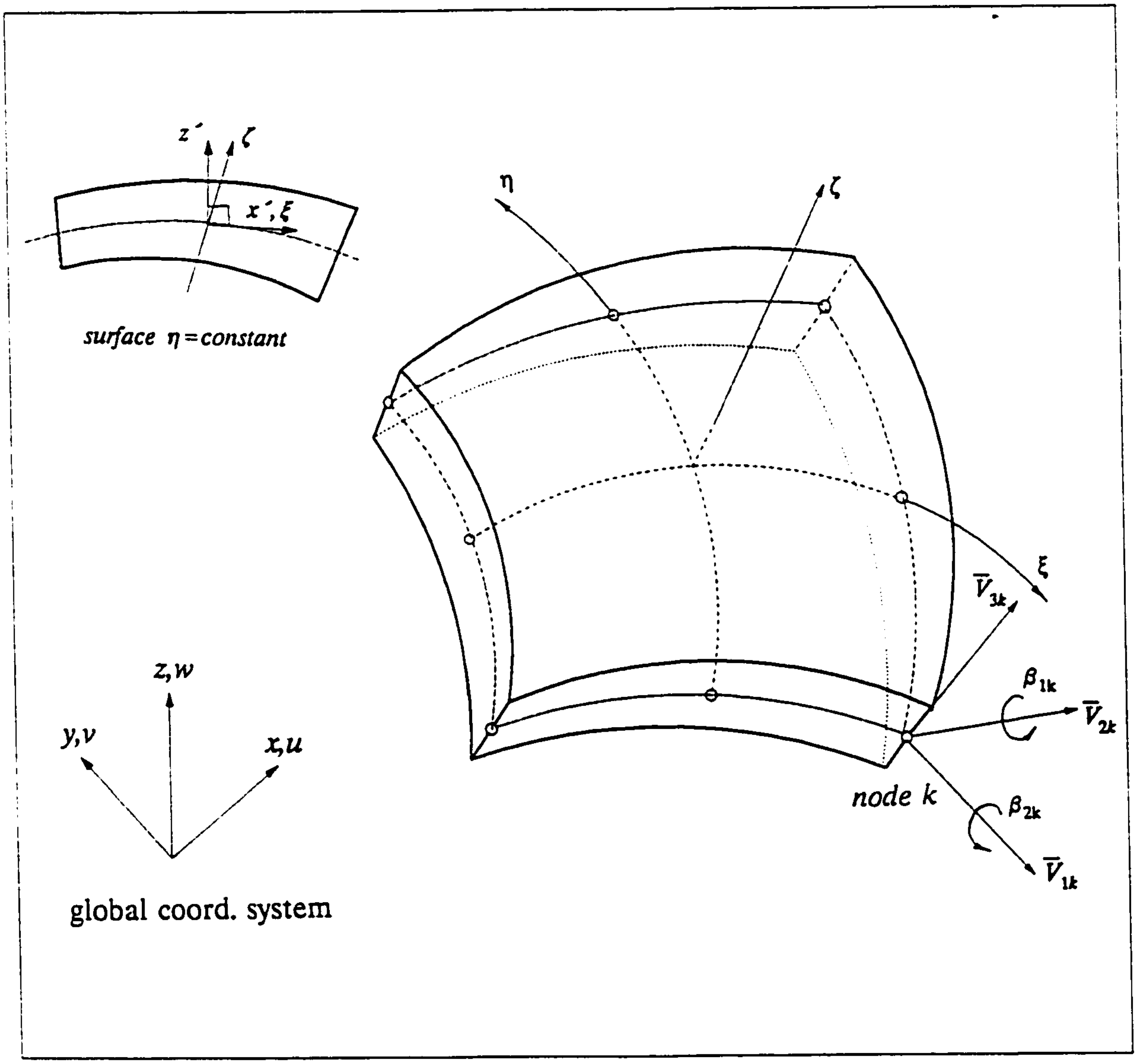

Figure 4.1 Geometrical Description of Ahmad Degenerated Shell Element

$$\bar{e}_2' = \bar{e}_3' \times \bar{e}_1'$$

The direction cosine matrix between this local Cartesian frame and the global Cartesian frame is defined as:

$$[\theta]_{3\times3} = \left[\bar{e}_1'\ \bar{e}_2'\ \bar{e}_3'\right]$$

so that

$$\begin{Bmatrix} \bar{e}_1' \\ \bar{e}_2' \\ \bar{e}_3' \end{Bmatrix} = [\theta]^T \begin{Bmatrix} \bar{e}_1 \\ \bar{e}_2 \\ \bar{e}_3 \end{Bmatrix} \tag{12}$$

(4) *Nodal Cartesian Coordinate System* $(\mathbf{V}_{1k}, \mathbf{V}_{2k}, \mathbf{V}_{3k})$

The purpose of this system is to have an unique Cartesian frame at each node of the finite element mesh to resolve the rotation vector so that the continuity of the rotation variables between elements is secured.

Following definitions are devised to make such a frame be independent of the geometry of the elements which contain the node:

The system has its origin at the shell mid-surface and unit vector $\mathbf{V}_{3k}$ is defined in the ζ direction which is constructed from the nodal coordinates of the top and bottom surface at the node k:

$$\overline{V}_{3k} = \frac{\overline{x}_k^{top} - \overline{x}_k^{bot}}{\left\| \overline{x}_k^{top} - \overline{x}_k^{bot} \right\|}$$

The unit vector $\mathbf{V}_{1k}$ is perpendicular to $\mathbf{V}_{3k}$ and parallel to the global xz-plane:

$$\overline{V}_{1k} = \left[\frac{V_{3k}^{z}}{\sqrt{\left(V_{3k}^{z}\right)^2 + \left(V_{3k}^{x}\right)^2}} \ , \ 0 \ , \ \frac{-V_{3k}^{x}}{\sqrt{\left(V_{3k}^{z}\right)^2 + \left(V_{3k}^{x}\right)^2}} \right]^T$$

or, if $\mathbf{V}_{3k}$ is coincident with the y direction ($V_{3k}^{x}=V_{3k}^{z}=0$), then

$$\overline{V}_{1k} = \left[\frac{-V_{3k}^{y}}{|V_{3k}^{y}|} \ , \ 0 \ , \ 0 \right]^T$$

The unit vector $\mathbf{V}_{2k}$ is perpendicular to the plane defined by $\mathbf{V}_{3k}$ and $\mathbf{V}_{1k}$, therefore:

$$\overline{V}_{2k} = \overline{V}_{3k} \times \overline{V}_{1k}$$

In summary, the vector $\mathbf{V}_{3k}$ defines the direction of the "normal" at node k, which is not necessarily perpendicular to the mid-surface at node k. Vector $\mathbf{V}_{1k}$ and $\mathbf{V}_{2k}$ define the rotations β_{2k} and β_{1k} respectively (see Figure 4.1).

§3-2 <u>Element Geometry</u>

The global coordinates of pairs of points on the top and bottom surface at each node are basic input to define element geometry. In the isoparametric formulation the coordinates of a point within the element is expressed as:

$$
\begin{aligned}
\bar{x} = \bar{x}(\xi,\eta,\zeta) &= \sum_{k=1}^{n} N_k(\xi,\eta)\frac{1-\zeta}{2}\bar{x}_k^{top} + \sum_{k=1}^{n} N_k(\xi,\eta)\frac{1-\zeta}{2}\bar{x}_k^{bot} \\
&= \sum_{k=1}^{n} N_k(\xi,\eta)\bar{x}_k^{mid} + \sum_{k=1}^{n} N_k(\xi,\eta)\frac{h_k\zeta}{2}\bar{V}_{3k} \qquad (13) \\
&= \bar{x}^{mid}(\xi,\eta) + \bar{z}(\xi,\eta,\zeta)
\end{aligned}
$$

where n is the number of nodes per element;

$N_k(\xi,\eta)$ are element shape functions corresponding to the surface of ζ=*const*;

h_k is the shell "thickness" at node k, i.e. the length of $\boldsymbol{x}_k^{top}$-$\boldsymbol{x}_k^{bot}$;

ξ,η,ζ are the curvilinear coordinates of the point under consideration;

$\boldsymbol{x}^{mid}$ is the global position vector of the point on the mid-surface (ζ=0);

z is the relative position vector of the point along the pseudonormal $\mathbf{V}_{3k}$ to the corresponding point on the mid-surface (see Figure 4.2a).

§3-3 Element Displacement Field

The element displacement field can be expressed as:

$$
\bar{u} = \begin{Bmatrix} u \\ v \\ w \end{Bmatrix} = \bar{u}^{mid} + \bar{u}^{rot} = \sum_{k=1}^{n} N_k(\xi,\eta)\begin{Bmatrix} u_k \\ v_k \\ w_k \end{Bmatrix} + \sum_{k=1}^{n} N_k(\xi,\eta)\frac{h_k\zeta}{2}\left[\bar{V}_{1k}, -\bar{V}_{2k}\right]_{3\times 2}\begin{Bmatrix} \beta_{1k} \\ \beta_{2k} \end{Bmatrix} \qquad (14)
$$

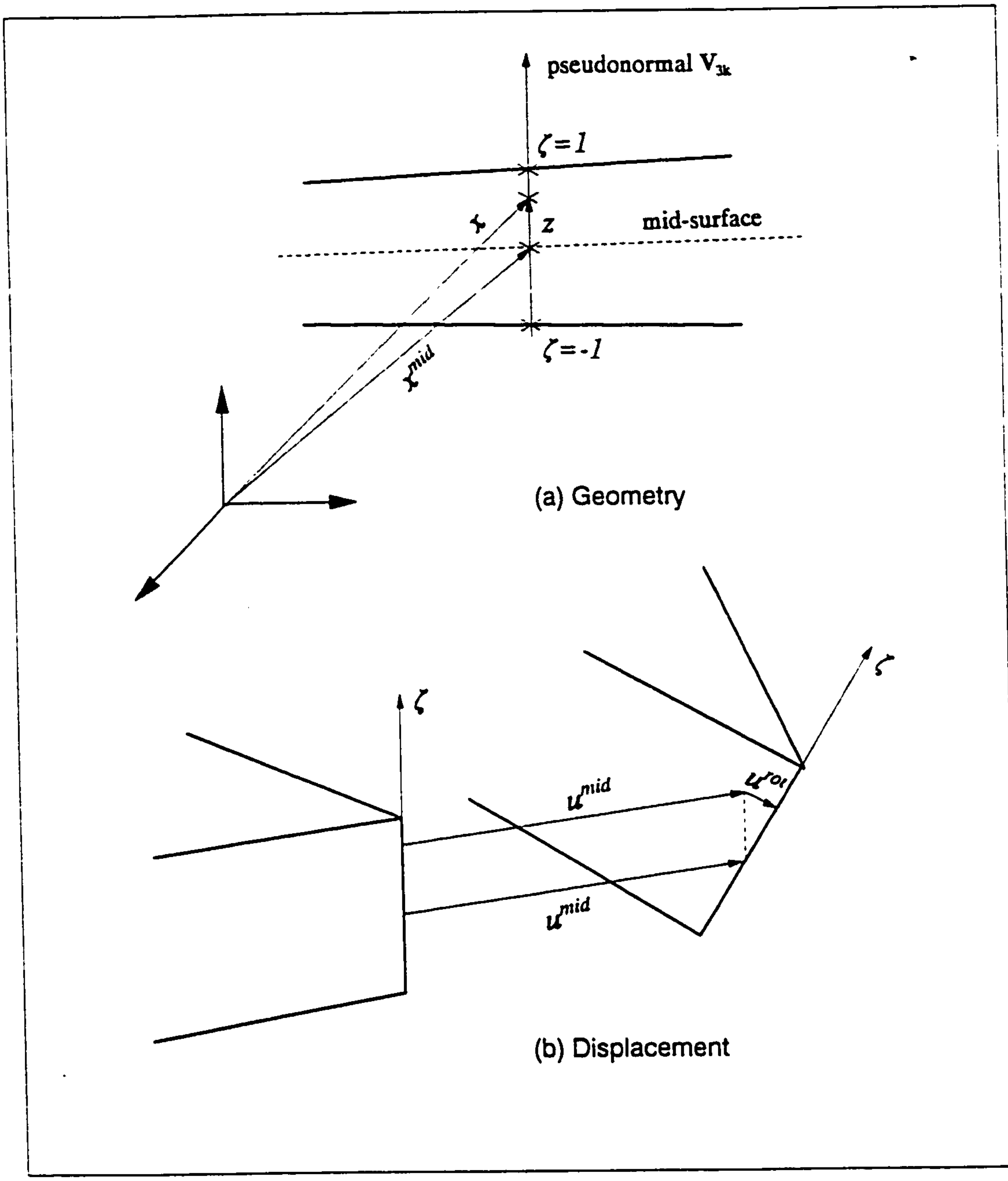

Figure 4.2 Element Geometry and Kinematics of Ahmad Shell

which is the sum of the displacement $\boldsymbol{u}^{\mathrm{mid}}$ of the point of the mid-surface and the displacement $\boldsymbol{u}^{\mathrm{rot}}$ caused by the pseudonormal rotation (as shown in Figure 4.2b).

§4 Calculations of Deformation Tensors

Using the given element geometry and displacement field in Equation (13) and (14), deformation tensors can be evaluated based on the relations discussed in §2.

A fundamental difference between 3D brick element and shell element is that, in shell element, local convective frame has to be used to describe strain and stress tensors to reflect the nature of shell structure. In this study, the local Cartesian frame $\{\boldsymbol{e}_i'\}$ is constantly used to resolve all the deformation tensors and establishing direct linkage between the nodal displacement vector and the resolved components of the deformation tensors. The reasons are twofold: (1) Being an orthonormal frame among three convective local frames, $\{\boldsymbol{e}_i'\}$ is the only frame which can reveal the true physical components of the deformation tensors; (2) The advantage of using true physical components is that the rest of the formulation is fully compatible with standard 3D large deformation FEA formulation and therefore benefits coding.

§4-1 Displacement Gradient Tensor u

Using Equation (14) and (9), we have:

$$\bar{\bar{u}} = \frac{\partial \bar{u}}{\partial \bar{x}} = \bar{e}_i \frac{\partial u_j}{\partial x_i} \bar{e}_j = \begin{pmatrix} \bar{e}_1 & \bar{e}_2 & \bar{e}_3 \end{pmatrix} [J]^{-1} \begin{bmatrix} u_{1,\xi} & u_{2,\xi} & u_{3,\xi} \\ u_{1,\eta} & u_{2,\eta} & u_{3,\eta} \\ u_{1,\zeta} & u_{2,\zeta} & u_{3,\zeta} \end{bmatrix} \begin{Bmatrix} \bar{e}_1 \\ \bar{e}_2 \\ \bar{e}_3 \end{Bmatrix}$$

$$= \{\bar{e}_1 \;\; \bar{e}_2 \;\; \bar{e}_3\}[J]^{-1}\{\sum_{k=1}^{n}(u_k^{mid}\begin{bmatrix} N_{k,\xi} & 0 & 0 \\ N_{k,\eta} & 0 & 0 \\ 0 & 0 & 0 \end{bmatrix} + v_k^{mid}\begin{bmatrix} 0 & N_{k,\xi} & 0 \\ 0 & N_{k,\eta} & 0 \\ 0 & 0 & 0 \end{bmatrix} + w_k^{mid}\begin{bmatrix} 0 & 0 & N_{k,\xi} \\ 0 & 0 & N_{k,\eta} \\ 0 & 0 & 0 \end{bmatrix}$$

$$- \frac{h_k}{2}\beta_{1k}\begin{bmatrix} \zeta N_{k,\xi}V_{2k}^x & \zeta N_{k,\xi}V_{2k}^y & \zeta N_{k,\xi}V_{2k}^z \\ \zeta N_{k,\eta}V_{2k}^x & \zeta N_{k,\eta}V_{2k}^y & \zeta N_{k,\eta}V_{2k}^z \\ N_k V_{2k}^x & N_k V_{2k}^y & N_k V_{2k}^z \end{bmatrix} + \frac{h_k}{2}\beta_{2k}\begin{bmatrix} \zeta N_{k,\xi}V_{1k}^x & \zeta N_{k,\xi}V_{1k}^y & \zeta N_{k,\xi}V_{1k}^z \\ \zeta N_{k,\eta}V_{1k}^x & Z N_{k,\eta}V_{1k}^y & \zeta N_{k,\eta}V_{1k}^z \\ N_k V_{1k}^x & N_k V_{1k}^y & N_k V_{1k}^z \end{bmatrix})\}\begin{Bmatrix} \bar{e}_1 \\ \bar{e}_2 \\ \bar{e}_3 \end{Bmatrix}$$

where Jacobian matrix [J] can be obtained from element geometry (13).

Now, transforming the coordinates from the global Cartesian frame $\{e_i\}$ to the local Cartesian frame $\{e_i'\}$ by equation (12) yields:

$$\begin{bmatrix} \frac{\partial u'}{\partial x'} & \frac{\partial v'}{\partial x'} & \frac{\partial w'}{\partial x'} \\ \frac{\partial u'}{\partial y'} & \frac{\partial v'}{\partial y'} & \frac{\partial w'}{\partial y'} \\ \frac{\partial u'}{\partial z'} & \frac{\partial v'}{\partial z'} & \frac{\partial w'}{\partial z'} \end{bmatrix} = [\theta]\begin{bmatrix} \frac{\partial u}{\partial x} & \frac{\partial v}{\partial x} & \frac{\partial w}{\partial x} \\ \frac{\partial u}{\partial y} & \frac{\partial v}{\partial y} & \frac{\partial w}{\partial y} \\ \frac{\partial u}{\partial z} & \frac{\partial v}{\partial z} & \frac{\partial w}{\partial z} \end{bmatrix}[\theta]^T$$

$$= \sum_{k=1}^{n}(u_k^{mid}[\theta][J]^{-1}\begin{bmatrix} N_{k,\xi} & 0 & 0 \\ N_{k,\eta} & 0 & 0 \\ 0 & 0 & 0 \end{bmatrix}[\theta]^T + v_k^{mid}[\theta][J]^{-1}\begin{bmatrix} 0 & N_{k,\xi} & 0 \\ 0 & N_{k,\eta} & 0 \\ 0 & 0 & 0 \end{bmatrix}[\theta]^{-1} + w_k^{mid}[\theta][J]^{-1}\begin{bmatrix} 0 & 0 & N_{k,\xi} \\ 0 & 0 & N_{k,\eta} \\ 0 & 0 & 0 \end{bmatrix}[\theta]^T \tag{15}$$

$$- \frac{h_k}{2}\beta_{1k}[\theta][J]^{-1}\begin{bmatrix} \zeta N_{k,\xi}V_{2k}^x & \zeta N_{k,\xi}V_{2k}^y & \zeta N_{k,\xi}V_{2k}^z \\ \zeta N_{k,\eta}V_{2k}^x & \zeta N_{k,\eta}V_{2k}^y & \zeta N_{k,\eta}V_{2k}^z \\ N_k V_{2k}^x & N_k V_{2k}^y & N_k V_{2k}^z \end{bmatrix}[\theta]^T + \frac{h_k}{2}\beta_{2k}[\theta][J]^{-1}\begin{bmatrix} \zeta N_{k,\xi}V_{1k}^x & \zeta N_{k,\xi}V_{1k}^y & \zeta N_{k,\xi}V_{1k}^z \\ \zeta N_{k,\eta}V_{1k}^x & Z N_{k,\eta}V_{1k}^y & \zeta N_{k,\eta}V_{1k}^z \\ N_k V_{1k}^x & N_k V_{1k}^y & N_k V_{1k}^z \end{bmatrix}[\theta]^T)$$

Define a vector form of the displacement gradient tensor as:

$$\left\{\overline{\overline{u}}\right\}_{9\times1} = \left[\left\{\overline{u}'_{,x'}\right\}^T, \left\{\overline{u}'_{,y'}\right\}^T, \left\{\overline{u}'_{,z'}\right\}^T\right]^T$$

where

$$\left\{\overline{u}'_{,x_i'}\right\}_{3\times1} = \left[\frac{\partial u'}{\partial x_i'}\ \frac{\partial v'}{\partial x_i'}\ \frac{\partial w'}{\partial x_i'}\right]^T = \begin{Bmatrix} u'_{,x_i'} \\ v'_{,x_i'} \\ w'_{,x_i'} \end{Bmatrix}$$

Then, by rearranging (15), a standard finite element G matrix form is obtained:

$$\left\{\overline{\overline{u}}\right\}_{9\times1} = \left[G\right]_{9\times5n}\left\{\tilde{u}\right\}_{5n\times1} \tag{16}$$

where n is the number of nodes per element, and

$$\left\{\tilde{u}\right\}_{5n\times1} = \left[\ \cdots\ u_k^{mid}\ v_k^{mid}\ w_k^{mid}\ \beta_{1k}\ \beta_{2k}\ \cdots\ \right]^T$$

is the nodal degree of freedom vector. The merit of (15) is that it has actually implied a scheme to calculate $[G]_{9X5n}$[2].

§4-2 Small Strain Tensor ε

The vector form of the small strain tensor ε is defined as:

$$\{\varepsilon'\}_{5\times1} = \begin{Bmatrix} \varepsilon_{x'} \\ \varepsilon_{y'} \\ \gamma_{x'y'} \\ \gamma_{y'z'} \\ \gamma_{x'z'} \end{Bmatrix} = \begin{Bmatrix} u'_{,x'} \\ v'_{,y'} \\ u'_{,y'}+v'_{,x'} \\ v'_{,z'}+w'_{,y'} \\ u'_{,z'}+w_{,x'} \end{Bmatrix} \tag{17}$$

$\varepsilon_{z'}$ is not listed due to the plane stress assumption ($\sigma_{z'}$=0). However, $\varepsilon_{z'}$ will be used in updating the thickness change of the shell element.

Based on (17), a $[B_o]$ matrix can be constructed from [G] matrix. Thus

$$\{\varepsilon\}_{5\times1} = [B_o]_{5\times5n}\{\tilde{u}\}_{5n\times1} \tag{18}$$

§4-3 Green-Lagrangian Strain Tensor **E**

Similarly, the vector form of the tensor is defined as:

$$\{E\}_{5\times1} = \begin{Bmatrix} E_{x'} \\ E_{y'} \\ 2E_{x'y'} \\ 2E_{y'z'} \\ 2E_{x'z'} \end{Bmatrix} = \{\varepsilon\} + \{\varepsilon_L\}$$

where

$$\{\varepsilon_L\} = \frac{1}{2}\begin{Bmatrix} \bar{u}'_{,x'}\bullet\bar{u}'_{,x'} \\ \bar{u}'_{,y'}\bullet\bar{u}'_{,y'} \\ 2\bar{u}'_{,x'}\bullet\bar{u}'_{,y'} \\ 2\bar{u}'_{,y'}\bullet\bar{u}'_{,z'} \\ 2\bar{u}'_{,z'}\bullet\bar{u}'_{,z'} \end{Bmatrix} = \frac{1}{2}\begin{bmatrix} \bar{u}'^{T}_{,x'} & 0 & 0 \\ 0 & \bar{u}'^{T}_{,y'} & 0 \\ \bar{u}'^{T}_{,y'} & \bar{u}'^{T}_{,x'} & 0 \\ 0 & \bar{u}'^{T}_{,z'} & \bar{u}'^{T}_{,y'} \\ \bar{u}'^{T}_{,z'} & 0 & \bar{u}'^{T}_{,x'} \end{bmatrix}_{6\times 9} \{\bar{\bar{u}}\}_{9\times 1} = \frac{1}{2}[A]_{6\times 9}[G]_{9\times 3n}\{\bar{u}\}_{3n\times 1} \tag{19}$$

is the nonlinear part of the Green-Lagrangian strain. By employing this strain, we have actually introduced second order ingredients into the formulation. Define:

$$[B_L]_{5\times 3n} = \frac{1}{2}[A]_{5\times 9}[G]_{9\times 3n}$$

then

$$\{E\} = ([B_o] + [B_L])\{\bar{u}\} = [\bar{B}]\{\bar{u}\} \tag{20}$$

§5 Tangent Stiffness Matrix in Shell Element Formulation

The linearized incremental form of the equilibrium equation used in this study is:

$$\begin{aligned} &\int_{\Omega^t}\left[(\Delta\bar{\bar{\sigma}}^{*} - 2\bar{\bar{\varepsilon}}_t\bullet\bar{\bar{\sigma}}^t):\delta\bar{\bar{\varepsilon}}^t + (\bar{\bar{\sigma}}^t\bullet\bar{\bar{u}}_t):\delta\bar{\bar{u}}^t\right]d\Omega^t \\ &= \int_{\Omega^t}\rho^t\Delta\bar{b}\bullet\delta\bar{u}^t d\Omega^t + \int_{\Gamma_F^t}\Delta\bar{t}\bullet\delta\bar{u}^t d\Gamma_F^t \end{aligned} \tag{21}$$

With the preliminary work done so far, equation (21) is directly applicable to the shell element formulation. The finite element equations required for solving large deformation shell problems are as follows:

$$\{\delta\bar{u}\}^{(e)T}\left([K_o]^{(e)} + [K_\varepsilon]^{(e)} + [K_u]^{(e)}\right)\{\Delta\bar{u}\}^{(e)} = \{\delta\bar{u}\}^{(e)T}\{\Delta R\}^{(e)} \tag{22}$$

The element "tangent stiffness matrix" in (22) is

$$[K]^{(e)} = [K_o]^{(e)} + [K_\varepsilon]^{(e)} + [K_u]^{(e)} \tag{23}$$

where, when $\Delta\sigma^*_{ij}=D^{ep}_{ijkl}\Delta E_{kl}$ and $\Delta\sigma^*:\delta\varepsilon \approx \Delta\sigma^*:\delta E$ is assumed

$$\left[K_o\right]^{(e)}_{5n\times 5n} = \int_{\Omega^{(e)t}} \left[\overline{B}\right]^{(e)T}_{5n\times 5} \left[D_{ep}\right]^{(e)}_{5\times 5} \left[\overline{B}\right]^{(e)}_{5\times 5n} \, d\Omega^{(e)t} \tag{24}$$

and

$$\left[K_\varepsilon\right]^{(e)}_{5n\times 5n} = \int_{\Omega^{(e)t}} \left[B_o\right]^{(e)T}_{5n\times 5} \left[S\right]^{(e)}_{5\times 5} \left[B_o\right]^{(e)}_{5\times 5n} \, d\Omega^{(e)t} \tag{25}$$

and

$$\left[K_u\right]^{(e)}_{5n\times 5n} = \int_{\Omega^{(e)t}} \left[G\right]^{(e)T}_{5n\times 9} \left[T\right]^{(e)}_{9\times 9} \left[G\right]^{(e)}_{9\times 5n} \, d\Omega^{(e)t} \tag{26}$$

$[D_{ep}]$, $[S]$ and $[T]$ matrix need to be modified to meet the "plane stress" ($\sigma_z=0$) condition assumed for degerated shell element and is detailed in Appendix 2.

§6 Stress Update in Shell Element Formulation

The stress update algorithm discussed in Chapter 2 for conventional 3D finite elements must be modified to meet the nature of the shell element formulation, where the strain and stress tensors are constantly resolved on the convective local Cartesian frame $\{e_i'\}$ instead of the fixed global Cartesian frame $\{e_i\}$.

Assuming the rotation between the convective local Cartesian frame $\{e_i'\}_t$ (at time t) and $\{e_i'\}_{t+\Delta t}$ (at time $t+\Delta t$) for the same material point is given by

$$\left(\bar{e}_i'\right)_{t+\Delta t} = \bar{\bar{T}} \bullet \left(\bar{e}_j'\right)_t$$

which is not necessarily equal to $\mathbf{\Delta R}$ from the polar decomposition of $\mathbf{\Delta F}$, then a modified stress update scheme for shell element formulation is as follows:

(1) Using the obtained displacement field $\{\Delta u\}$, calculate the deformation gradient tensor $\mathbf{\Delta F}$;

(2) Polar decomposed $\mathbf{\Delta F}$ into the pre-stretch tensor $\mathbf{\Delta U}$ and the rotation tensor $\mathbf{\Delta R}$;

(3) Using $\mathbf{\Delta U}$-1 as strain increment, calculate the co-rotational stress increment $\Delta\sigma^*$ by a proper stress integration scheme. A multi-step "elastic predictor and radial return method" is adopted in this work;

(4) Update the stress tensor by rotating the reference frame to the new local Cartesian frame $\{e_i'\}_{t+\Delta t}$: $\sigma^{t+\Delta t}=\mathbf{T}\bullet\mathbf{\Delta R}^T\bullet(\sigma^t+\Delta\sigma^*)\bullet\mathbf{\Delta R}\bullet\mathbf{T}^T$.

Numerical calculations shows that the difference between $\mathbf{T}$ and $\mathbf{\Delta R}$ is nominal, which indicates a direct update of $\sigma^{t+\Delta t}=\sigma^t+\Delta\sigma^*$ can be a good approximation for shell element formulation.

§7 Numerical Stability of Shell Element

When 8-node quadratic 3D degenerated shell element were first introduced by Ahmad et al., 3X3 integration was used for all energy terms, i.e. shear, membrane and flexure. It was considered to be appropriate as the minimum order of integration required to produce exact results for the element at the time. However, the results obtained were found to be reasonable only for thick shells. In the case of moderately thick and thin shells, results departed from the analytical solutions. The discrete computational model was observed to be too stiff and show very slow convergency rate, or even diverge in problems with highly constrained boundaries. This phenomenon was generally called "locking". Thereafter, the development of efficient shell elements has attracted significant research interest.

§7-1 Locking and Reduced Integration

Zienkiewicz *et al.*[3] proposed the use of the so called reduced integration technique to tackle this difficulty. A 2X2 integration was used to replace 3X3 integration for shear stress term. As a result, improvement was seen on moderately thin shells. Further improvement in results was obtained by reducing the order of integration for both the membrane stress and shear stress terms. The method was first considered and used as a "trick" before it was observed that the stiffening of the structure was due to shear and membrane locking.

The shear and membrane locking which inhibits the convergence of results in the case of thin shells occurs because of the inability of the degenerated shell elements to model deformed states in which the transverse shear and membrane strains vanished throughout the element. For example, degenerated shell element can not bend without stretching or generating transverse shearing. The existence of even a small membrane or transverse shear strains may cause the membrane or shear energy to overshadow the bending energy, so that the stiffness of the shell appears artificially high. The reduced order of integration for the shear and membrane terms underestimates their erroneous energies, thus the bending energy is recovered as the major constituent of the total strain energy.

In some simple situations, reduced integration technique can be clearly demonstrated for its rationality and effectiveness. In 1977, T.J.R. Hughes[4] published a detailed study about the numerical locking of a beam and plate element, and the impact of reduced integration technique in those situations. The work and many subsequent studies[5-6] basically triggered the enthusiasm in this field later on.

§7-2 Rank Deficiency and Hourglass Control

The reduced integration technique for degenerated shell elements gains significant popularity with widespread applications, not only because it helps to prevent locking but also saves a great amount of computational cost. However, the reduced integration technique actually yields stiffness matrices which are rank deficient. In other words, by using the technique a singular structural stiffness matrix is obtained, which, in the absence of proper displacement boundary conditions, may result in disproportionately large displacements. Since some of these deformation modes are delivered without any output to the strain energy, they are called spurious modes (zero energy modes). The order of numerical integration of various terms has a direct effect on the number of zero energy modes: the lower the integration order, the higher the number of such energy modes. A through study of those

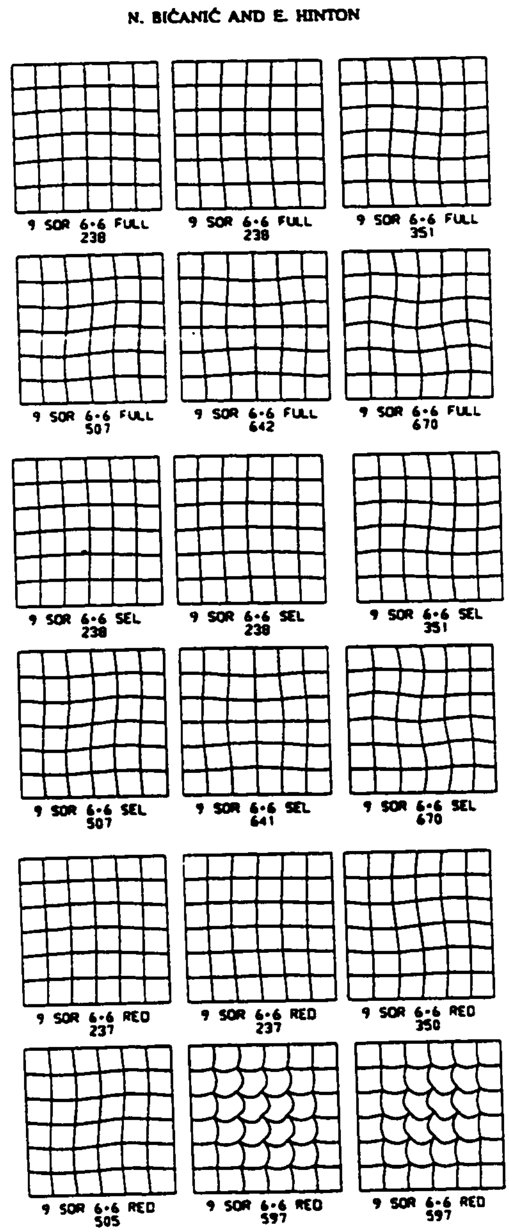

Figure 4.3 Spurious Mode and the Effects on the Mesh Deformation[7]

spurious modes on various elements can be found in the literature [7]. Figure 4.3 shows some of those modes and their possible effects on element patches (mesh). Since the deformation modes cause no energy increase in the structure, they can be easily exaggerated.

Therefore, the reduce-integrated elements are always accompanied by certain spurious mode control (often called hourglass control) schemes. Those works have been largely reflected in many of T. Belytschko's studies[9-13].

As the results of the mentioned studies, some of the reduce-integrated elements have become very popular now, especially for nonlinear finite element analysis. A typical example is the 4-node quadrilateral element with only one integration point, which has been continuously explored by Belytschko, et al[14] for years. The numerical advantage is so obvious. It is only about one quarter of the cost of the conventional 4-node element, yet it prevents various locking behaviours.

However, it must be cautioned about using these reduce-integrated elements, especially for nonlinear analysis. A fundamental reason for this is that the theories of reduced integration and hourglass control are only well discussed in terms of regular element shape. For metal forming analysis, element distortion is common.

§7-3 Mixed Strain Component Interpolation

In sheet metal forming practices, thin shells with highly constrained boundary conditions are often encountered. In these cases, selective or reduced integration procedures may still fail to guarantee the convergence[11].

Some other techniques have also been intensively studied to overcome locking, particularly for shear locking. The focus here has been the numerical controversy of isoparametric shell element using the same shape function to interpolate both displacement variables and the pesudonormal rotation variables. Because of this fundamantal nature, the Kirchhoff-Love hypothesis for thin shells is very difficult to be approximated on degenerated shells.

Based on this understanding, Bathe, K. J. *et al.* and Huang & Hinton studied other approaches: mixed strain component interpolations.

Bathe & Dvorkin[16] proposed a 4-node element with different integration schemes for the in-plane strain and transverse shear strain components. The main idea was the transverse shear strain components, which is directly affected by the pesudonormal rotation variable interpolation are separated from the in-plane components, and re-interpolated with lower ordered shape functions. A variational with lagrange multiplier constrains was advised to formulate the element. Later on, the approach was extended to a 8-node shell element as well[17]. Huang and Hinton[18-19] employed a much similar approach to construct a 9-node degenerated shell element.

A most recent work was reported by Boisse *et al.*[20,21]. They devised a simple isoparametric 3-node shell element with mixed strain component interpolation and employed the element in the analysis of sheet metal stamping process successfully. Indications of similar usage of the mixed interpolation are also found in ABAQUS's theory manual[22].

§7-4 A New Penalty Method

Observations made by the author in implementing the degenerated shell elements in sheet metal stamping analysis have been that the failure of numerical processes are mostly accompanied by the sudden occurrence of excessive of transverse shear strain components, and therefore due to shear locking.

In sheet metal stamping, very thin shell structures are common, where the Kirchhoff-Love condition should tend to dominate, so that

$$\begin{Bmatrix} \theta_{x'} - \omega'_{,y'} \\ \theta_{y'} + \omega'_{,x'} \end{Bmatrix} \dashrightarrow \begin{Bmatrix} 0 \\ 0 \end{Bmatrix} \tag{27}$$

However, the condition can hardly be rendered by the degenerated shell elements because of the use of different interpolations for $\{\theta_{x'}, \theta_{y'}\}$ and $\{w'_{,x'}, w'_{,y'}\}$.

In this study, the objective is to develop a remedy to avoid the artificial occurrence of the excessive transverse shear strains, at the same time, without breaking the consistency in the current process of implementing large deformation theory in degenerated shell element. Under such a consideration, an additional simple penalty term is advised as:

$$\int_{\Omega^{(e)t}} C_p \delta\left(\theta_{x'} - w'_{,y'} \quad \theta_{y'} + w'_{,x'}\right) \begin{Bmatrix} \theta_{x'} - w'_{,y'} \\ \theta_{y'} + w'_{,x'} \end{Bmatrix} d\Omega^{(e)t} \tag{28}$$

which yields an additional term in the element stiffness matrix formulation:

$$\left[K_p\right]^{(e)}_{5n\times 5n} = \int_{\Omega^{(e)t}} C_p \left[B_p\right]^{(e)T}_{5n\times 2} \left[B_p\right]^{(e)}_{2\times 5n} d\Omega^{(e)t} \tag{29}$$

where C_p is the penalty parameter. The magnitude of C_p controls the degree for which condition (27) need to be implemented;

$[B_p]$ is the matrix which relates the nodal degrees of freedom to the terms in (27) and derived in Appendix 3.

It should be mentioned that the use of condition (27) is limited in the formulation of "tangential stiffness matrix". That is the residual force evaluation continues to be conducted in the normal way as before. Therefore, as far as the solution converges, no change is expected with the solution from using the additional term. The only difference lies in that a much greater stability is achieved by the method.

Another important fact about the method proposed here is it is independent of the methods mentioned before. Therefore it is possible to combine this penalty method with any of others to achieve a secured stability.

§8 Numerical Examples

Two stamping cases are chosen to verify the effectiveness of the discussed large deformation shell element formulation with the penalty term. To isolate the test from influence of other factors, the penalty method is the only measure taken to overcome shear locking.

Two examples are illustrated in Figure 4.4. Both examples use the same 100X100X0.8 mm mild steel square blank. The first example concerns a square punch. The punch is 50X50mm with a 4mm shoulder radius and a 10mm corner radius, and the die 54X54mm with a 4mm shoulder radius and 11.5mm corner radius (as shown in Figure 4.4a). The second example involves a ϕ50mm cylindrical punch with a 4mm shoulder radius and a ϕ54mm die with a 9mm shoulder radius (see Figure 4.4b). Figure 4.5 shows the

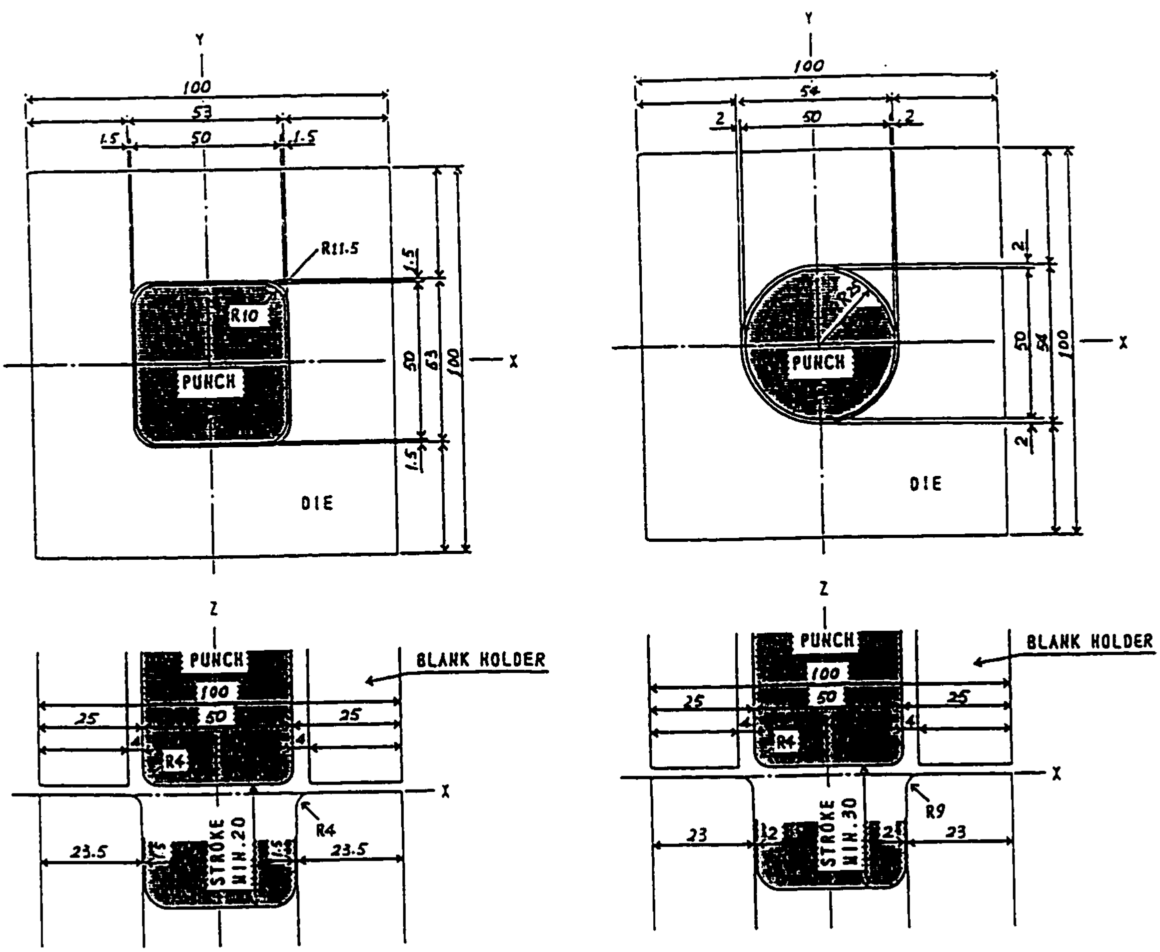

(a) Square Punch

(b) Cylindrical Punch

Figure 4.4 Geometrical Dimensions for Two Square Cup Drawing Processes

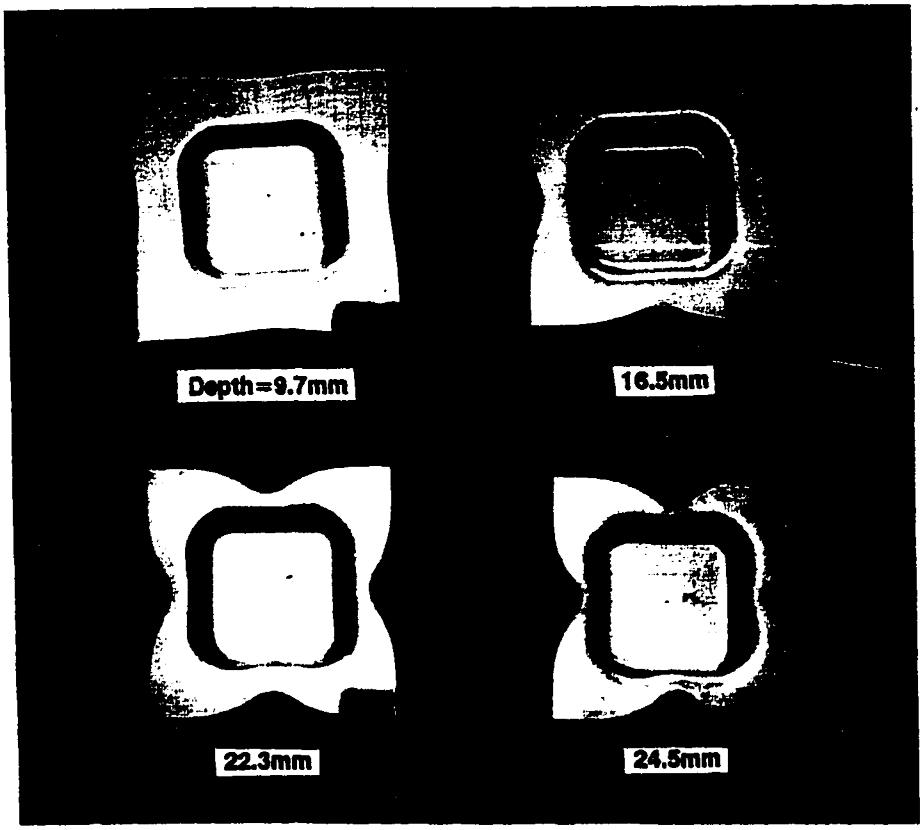

Figure 4.5(a) Experimental Samples Stamped by Square Punch

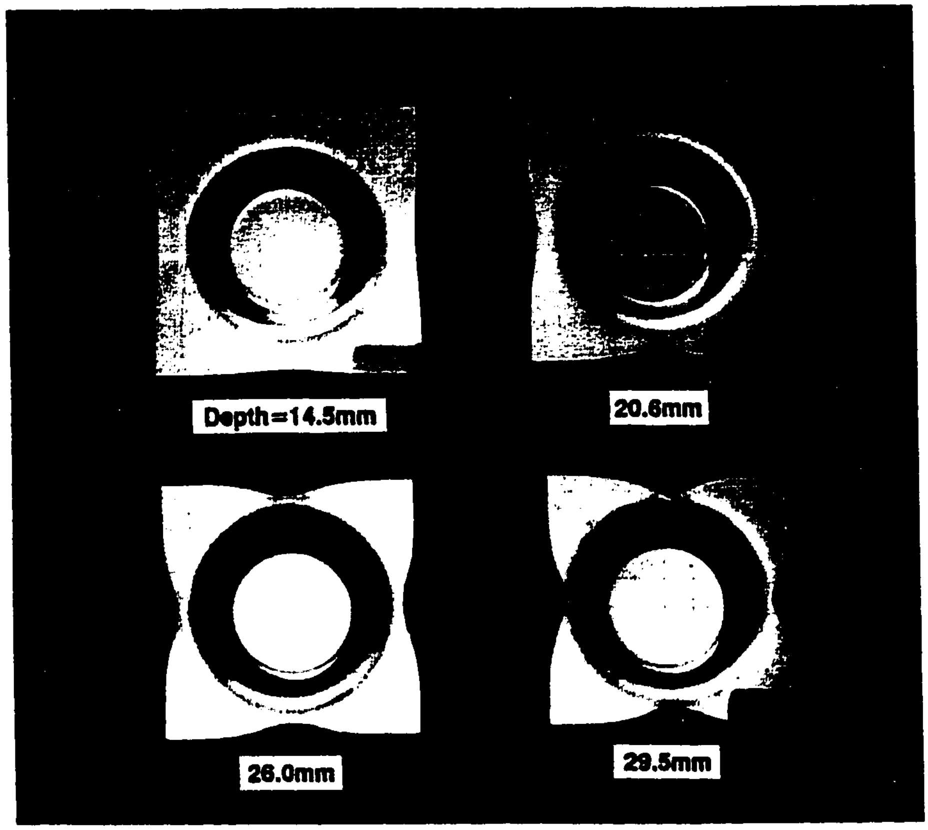

Figure 4.5(b) Experimental Samples Stamped by Cylindrical Punch

experimental samples of the above mentioned stamping process.

The material properties are specified as follows: E=2100000 MPa, ν=0.3, $\sigma=565.32(0.007117+\varepsilon_p)^{0.2589}$

Different elements and mesh are tested in the analysis, which include 3-node constant strain element, 4-node bilinear quadrilateral, 6-node triangle, and 8/9-node quadrilaterals. Without the penalty term, all the elements failed to converge within the initial few increments. Penalty term improved the situation dramatically. For higher order elements (6/8/9-noded), the cup can be successfully drawn to about 10mm of depth, but still fails in later increments. The two lower order elements (3/4-node), the processes were carried through to the end of the analysis without divergency. Those results are discussed as follows.

Figure 4.6 and 4.7 show the simulation results of the square punch case with 3-node linear triangle elements and 4-node bilinear quadrilateral elements respectively. They have shown very much similar deformation pattern in terms of flange shape and thickness strain distribution. The most significant thichening occurs in the central area of the flange, while the thinning occurs in the corner area of the cup wall. Those features agree well with the experimental observation. Two thickening regions on the flange which are symmetrical to the diaggonal line are shown on both results which agree with the wrinkling tendency observed on experimental sample in the same area.

However, similar to what mentioned in 2D examples in Chapter 2, the strain numbers from two meshes do differ to certain degree. For example, the maximum thickening strain for the triangular mesh is +42% with a comparison of 62% for the 4-node element mesh (see Figure 4.6(d) and 4.7(d)). Interestingly, the 4-node element also shows a larger thining strain, i.e. -27.8% vs -17% from triangular element. Those results show the fact that, though large deformation nonlinear finite element does offer a useful tool for analyzing the forming

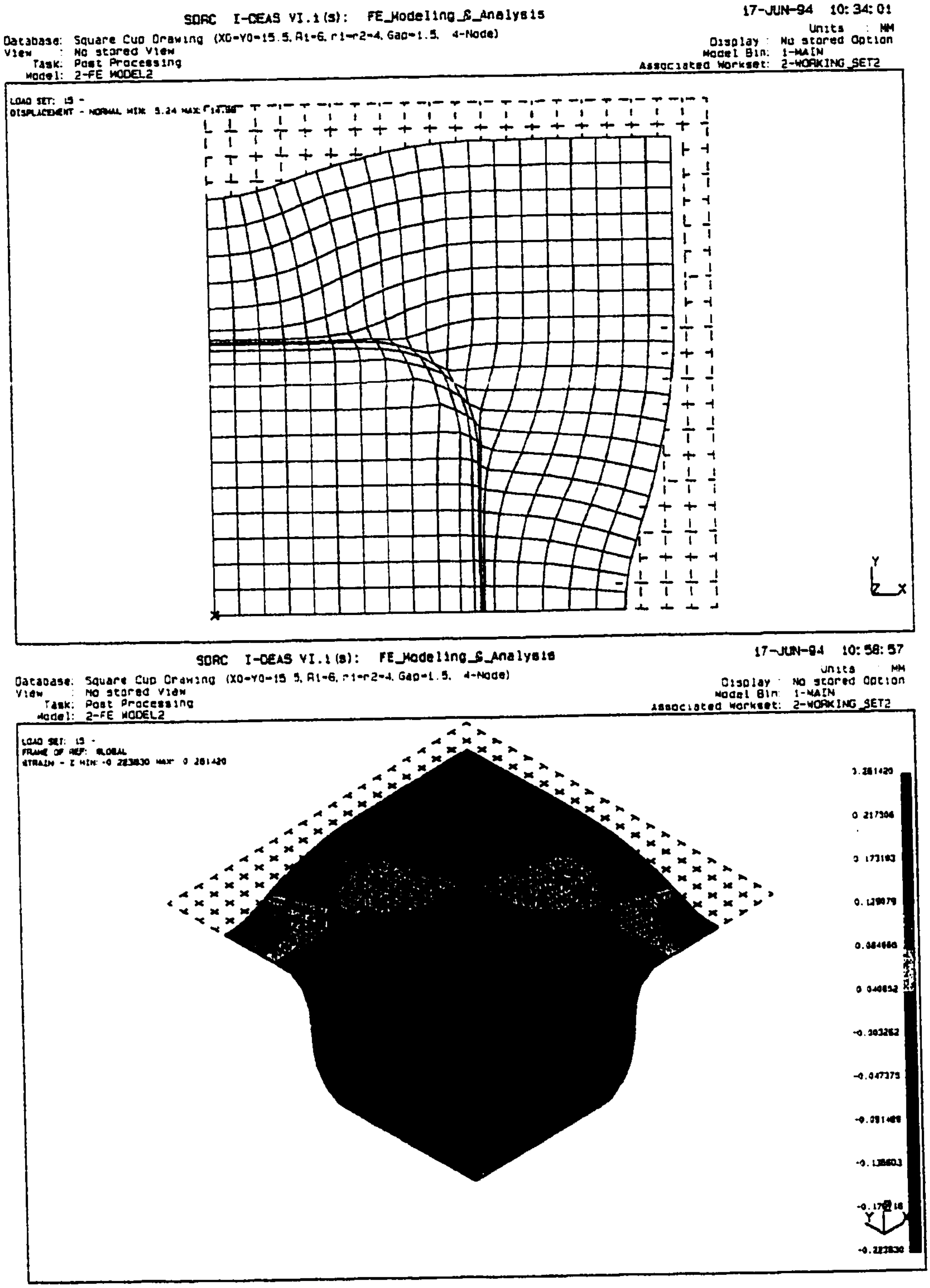

Figure 4.6(a) Square Cup Drawing with a Square Punch (Punch Depth = 14.98mm)

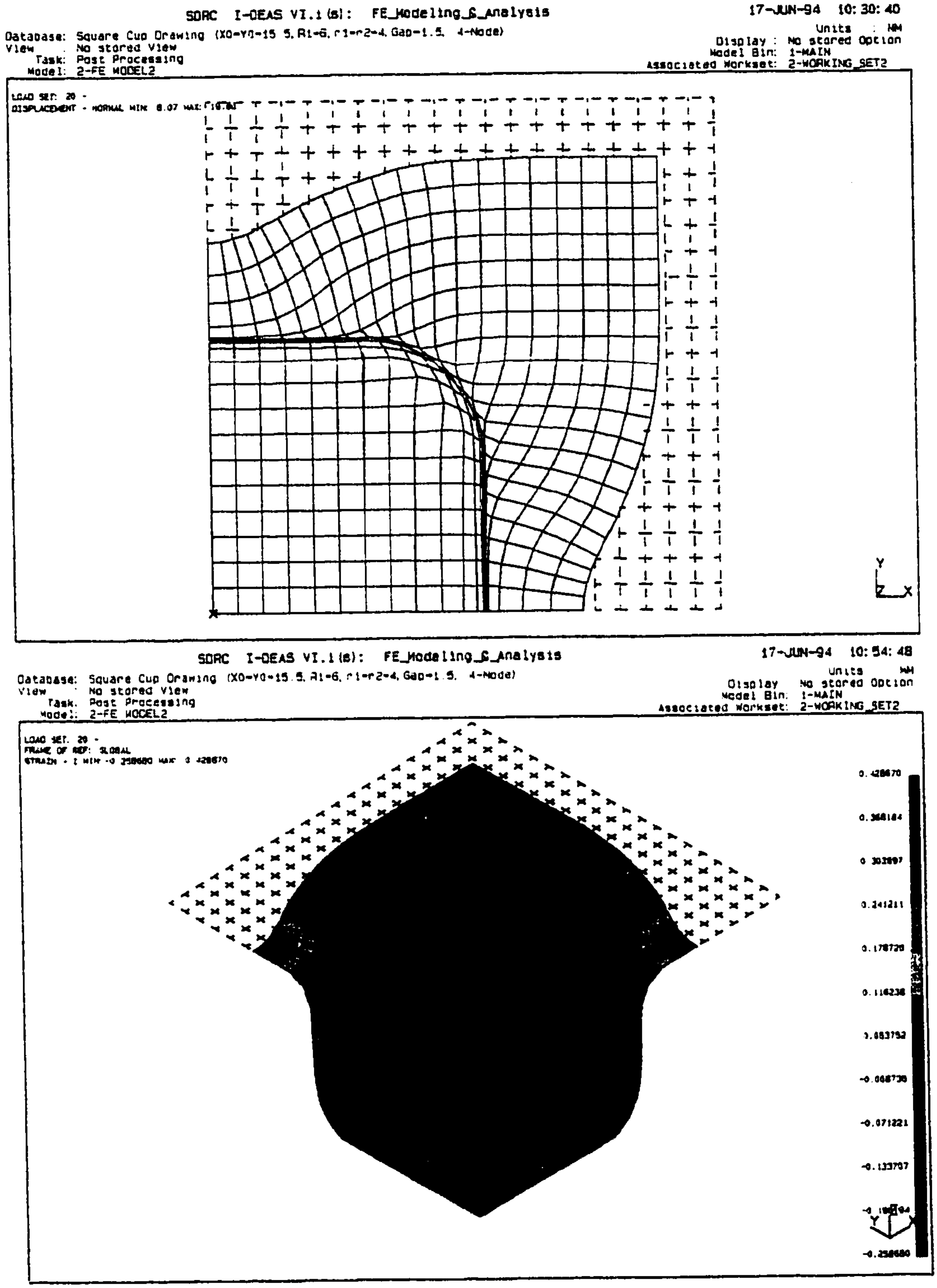

Figure 4.6(b) Square Cup Drawing with a Square Punch (Punch Depth = 19.80mm)

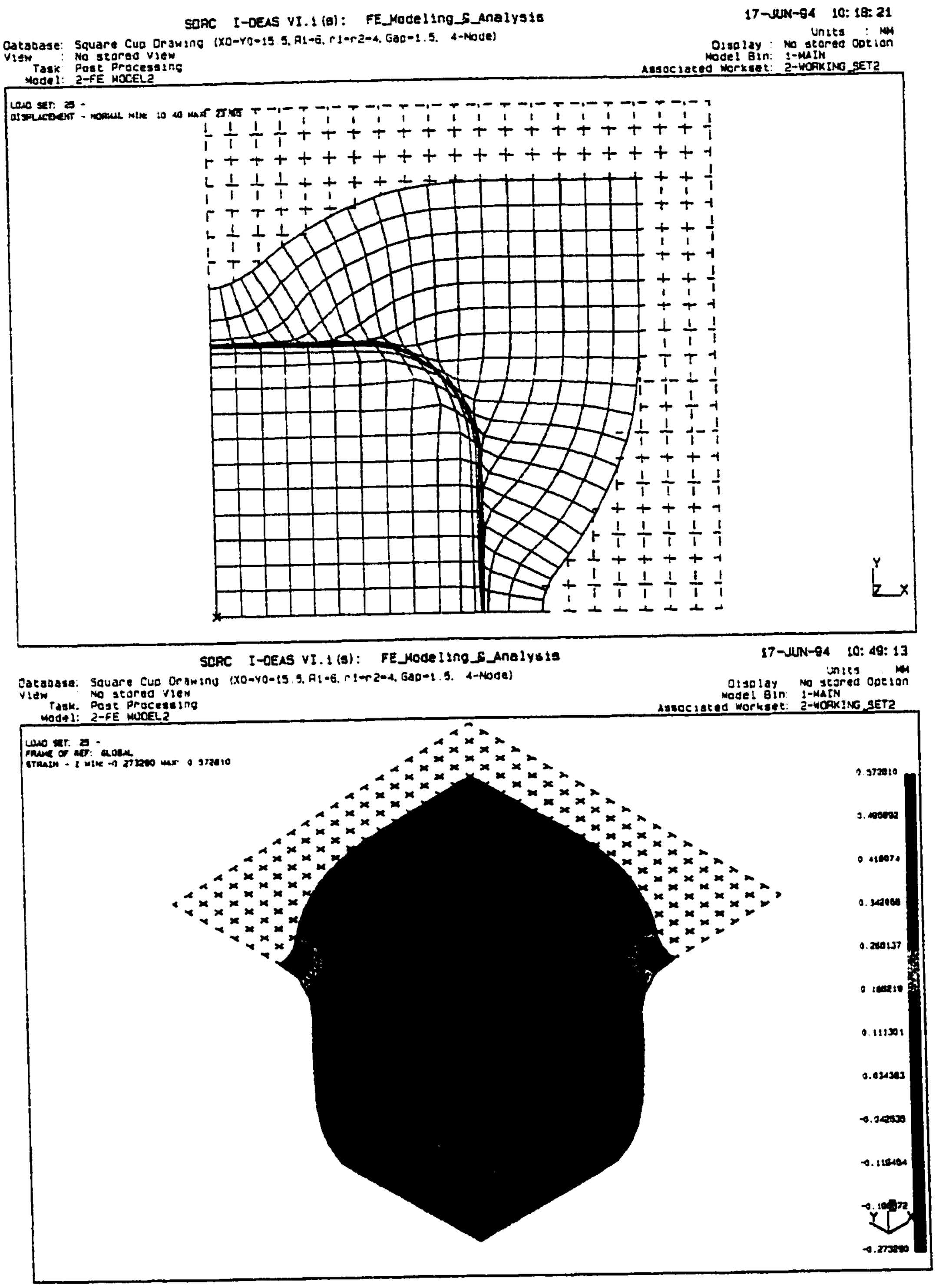

Figure 4.6(c) Square Cup Drawing with a Square Punch (Punch Depth = 23.65mm)

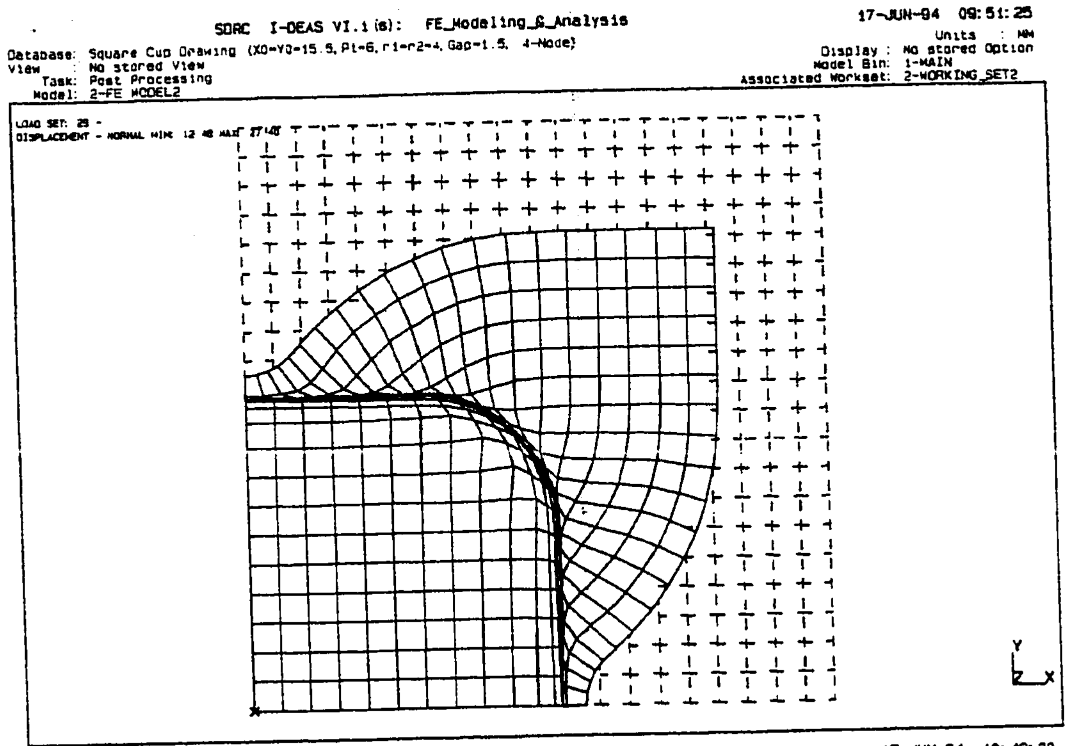

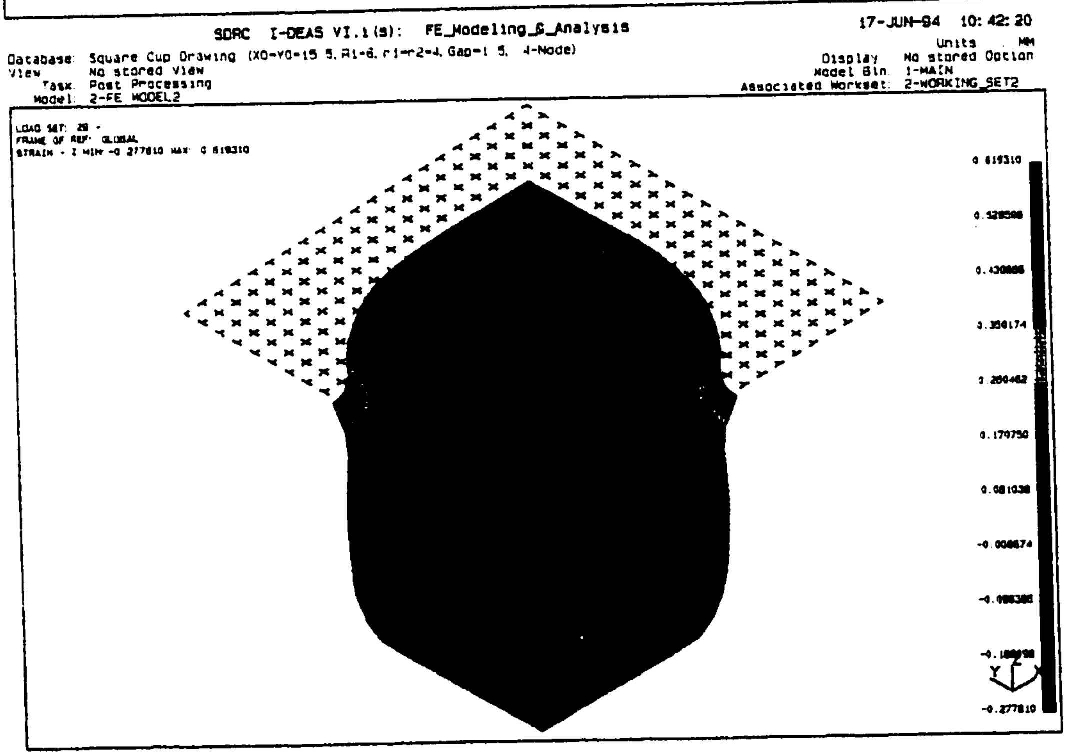

Figure 4.6(d) Square Cup Drawing with a Square Punch (Punch Depth = 27.40mm)

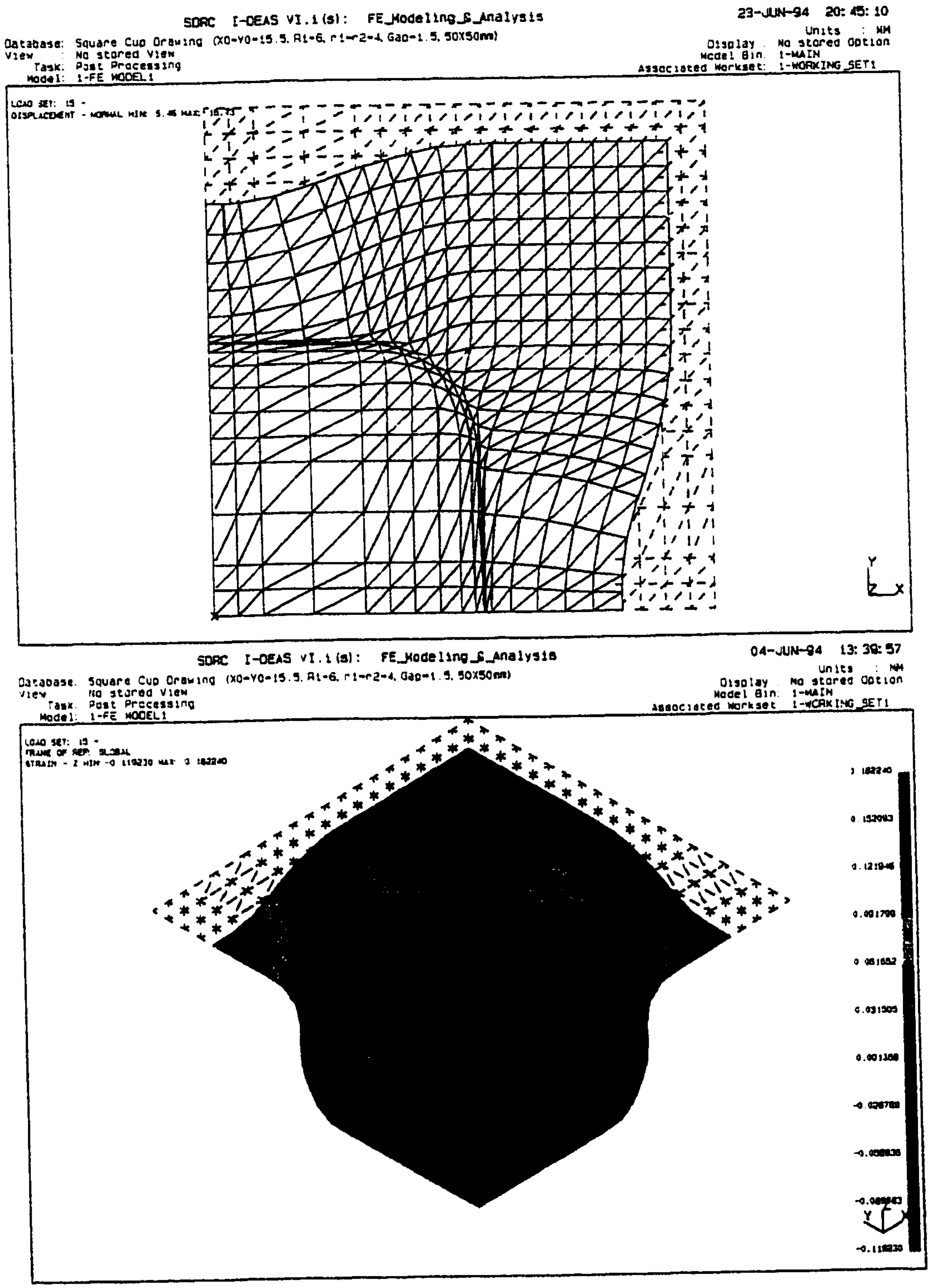

Figure 4.7(a) Square Cup Drawing with a Square Punch (Punch Depth = 15.43mm)

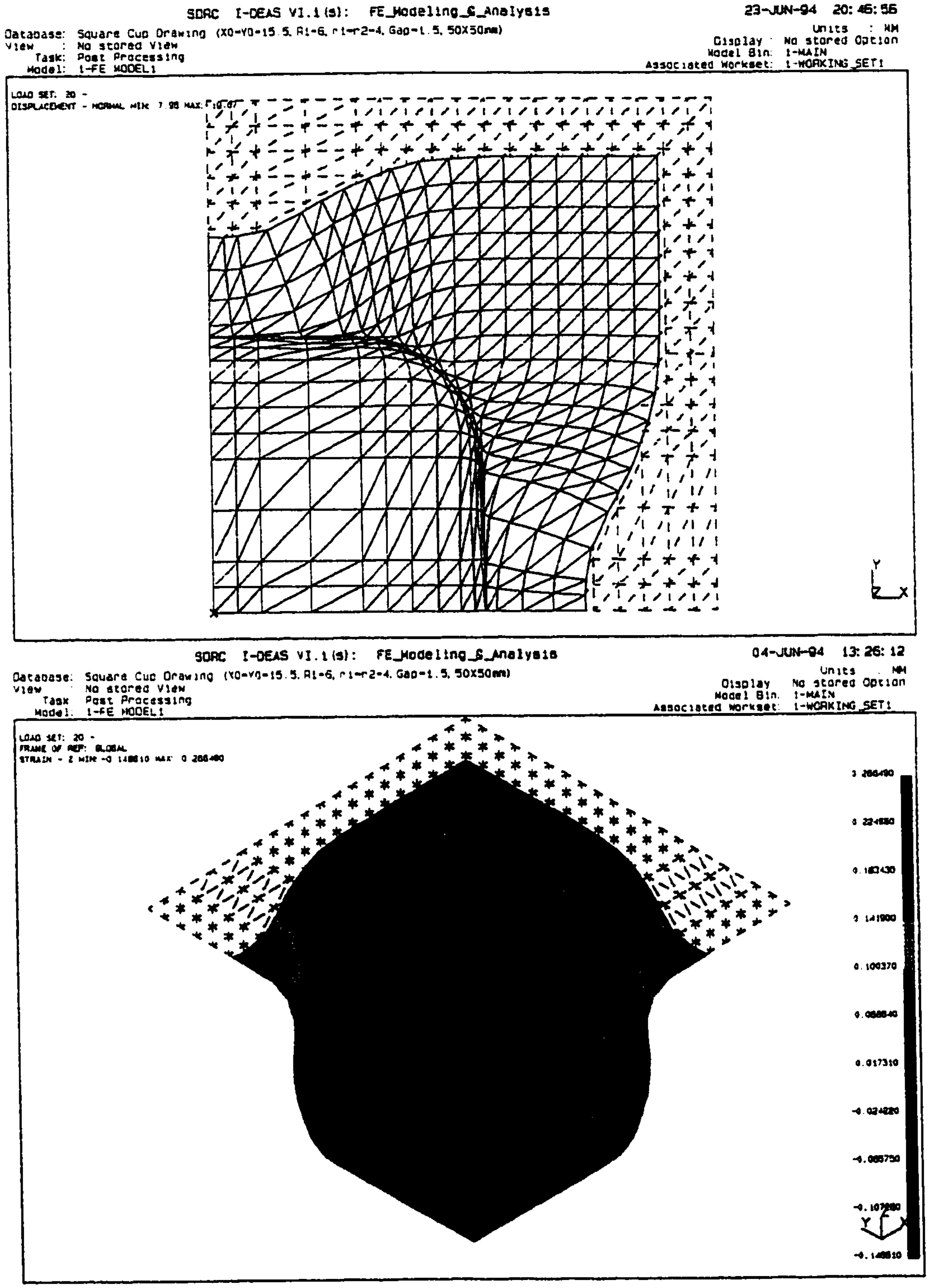

Figure 4.7(b) Square Cup Drawing with a Square Punch (Punch Depth = 19.07mm)

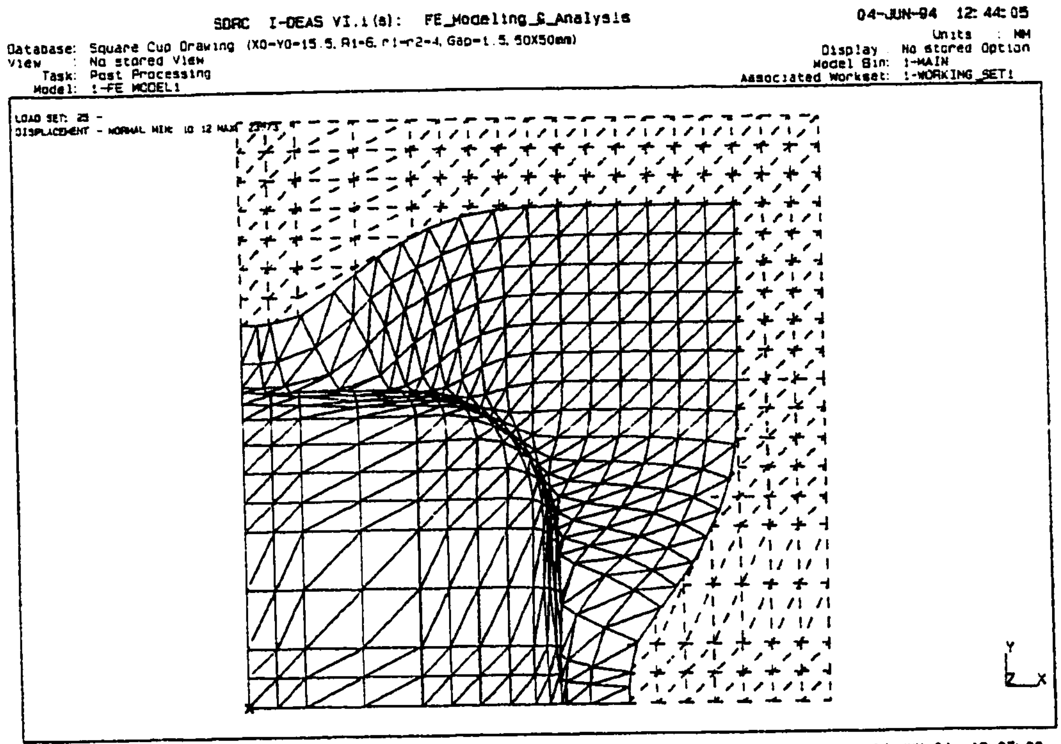

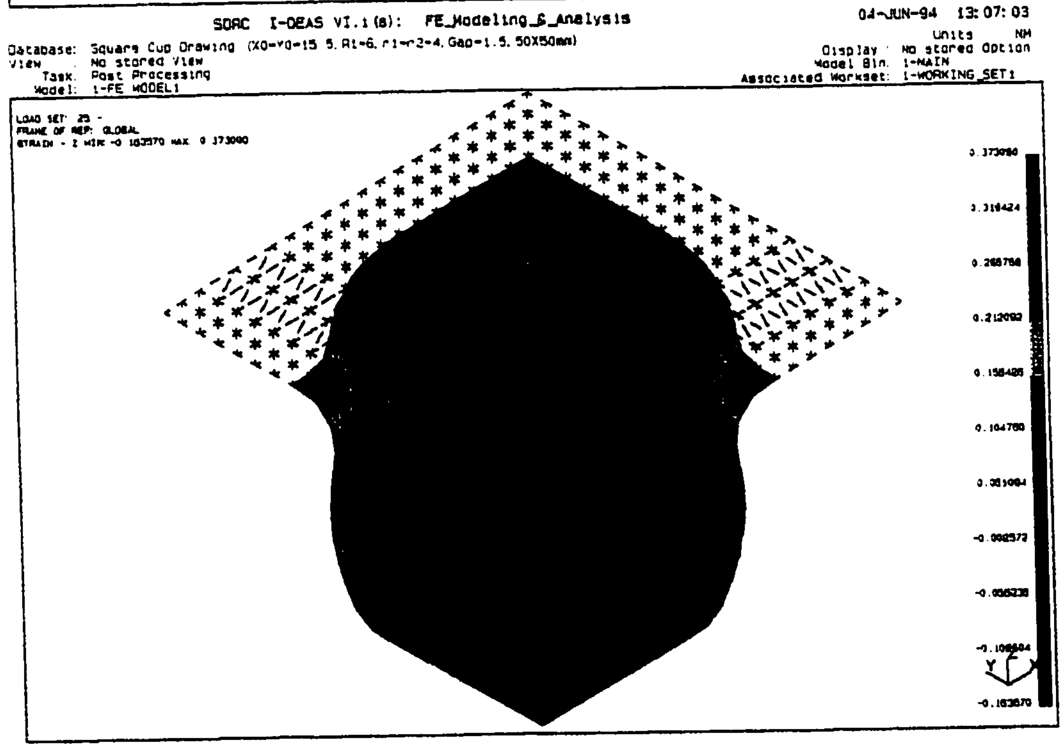

Figure 4.7(c) Square Cup Drawing with a Square Punch (Punch Depth = 23.73mm)

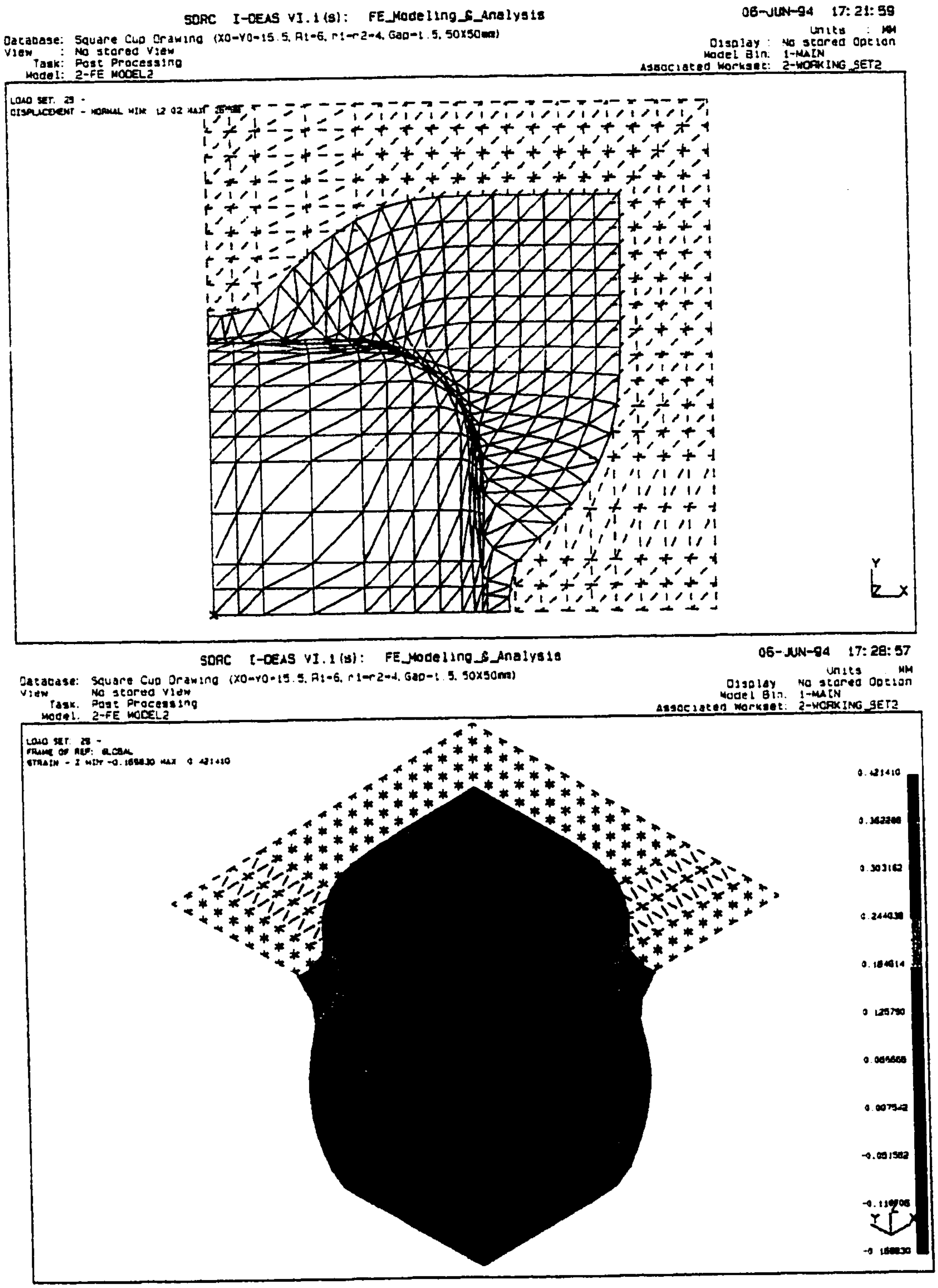

Figure 4.7(d) Square Cup Drawing with a Square Punch (Punch Depth = 26.98mm)

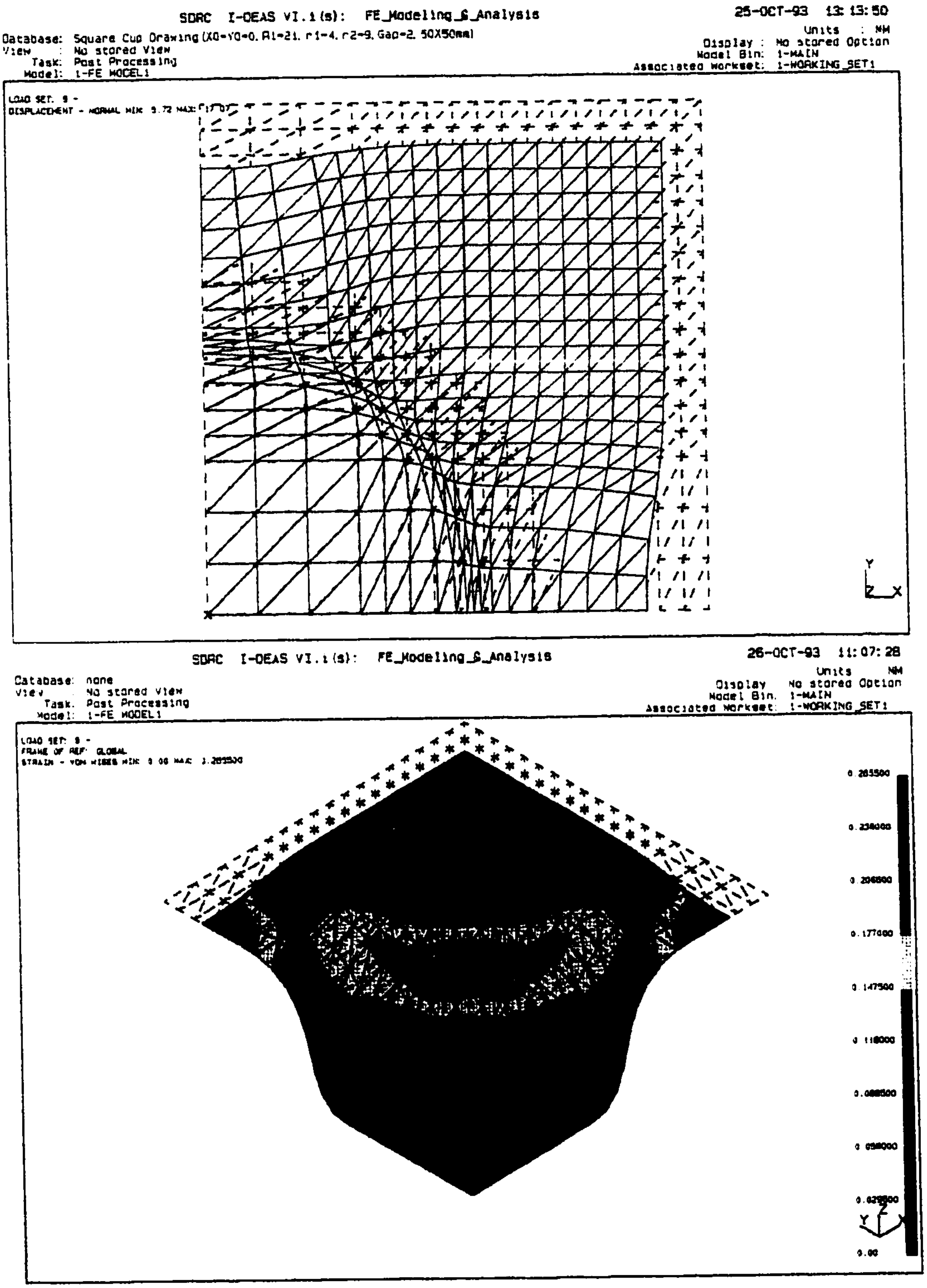

Figure 4.8(a) Square Cup Drawing with a Cylindrical Punch (Punch Depth = 17.07mm)

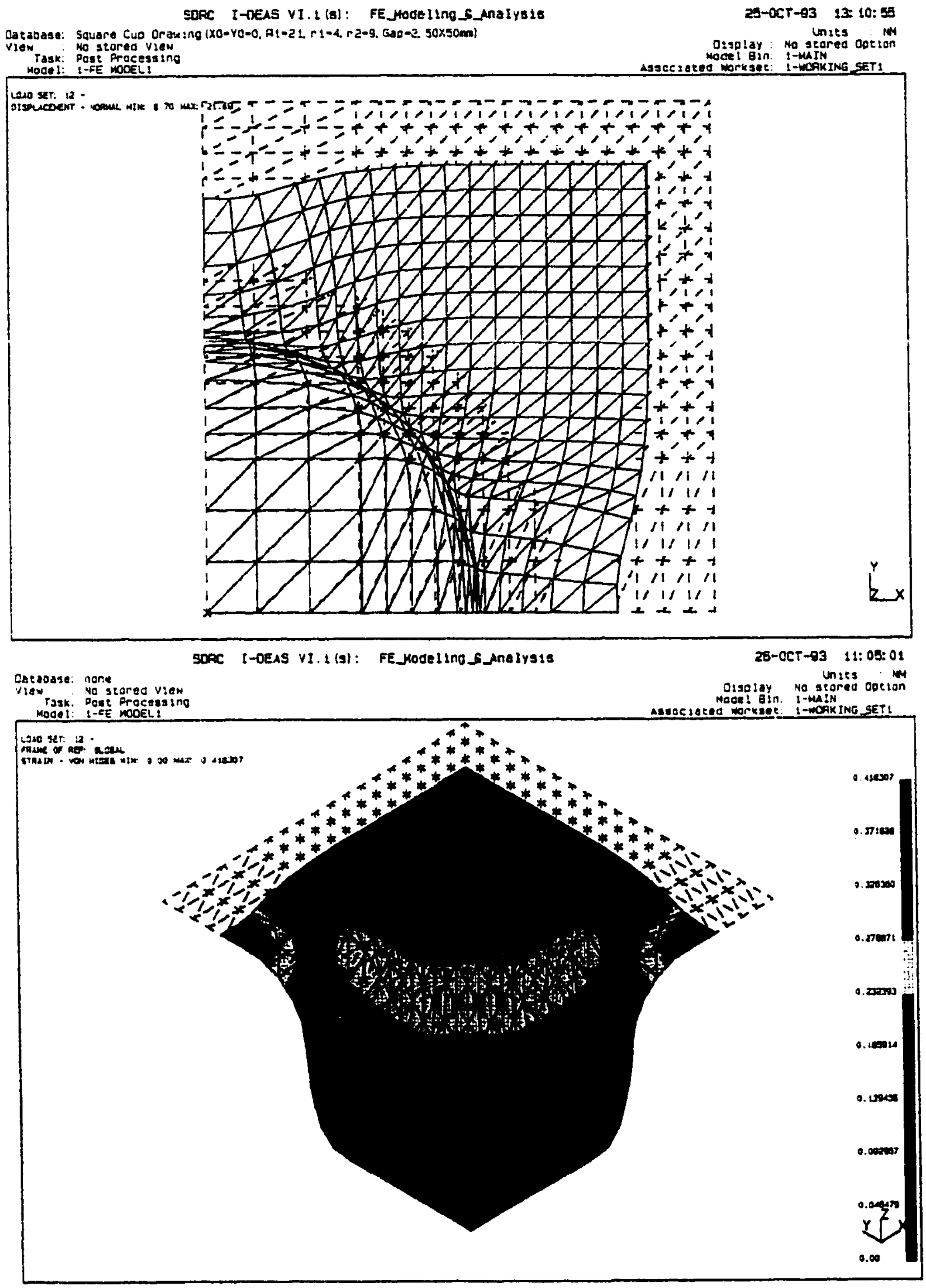

Figure 4.8(b) Square Cup Drawing with a Cylindrical Punch (Punch Depth = 21.69mm)

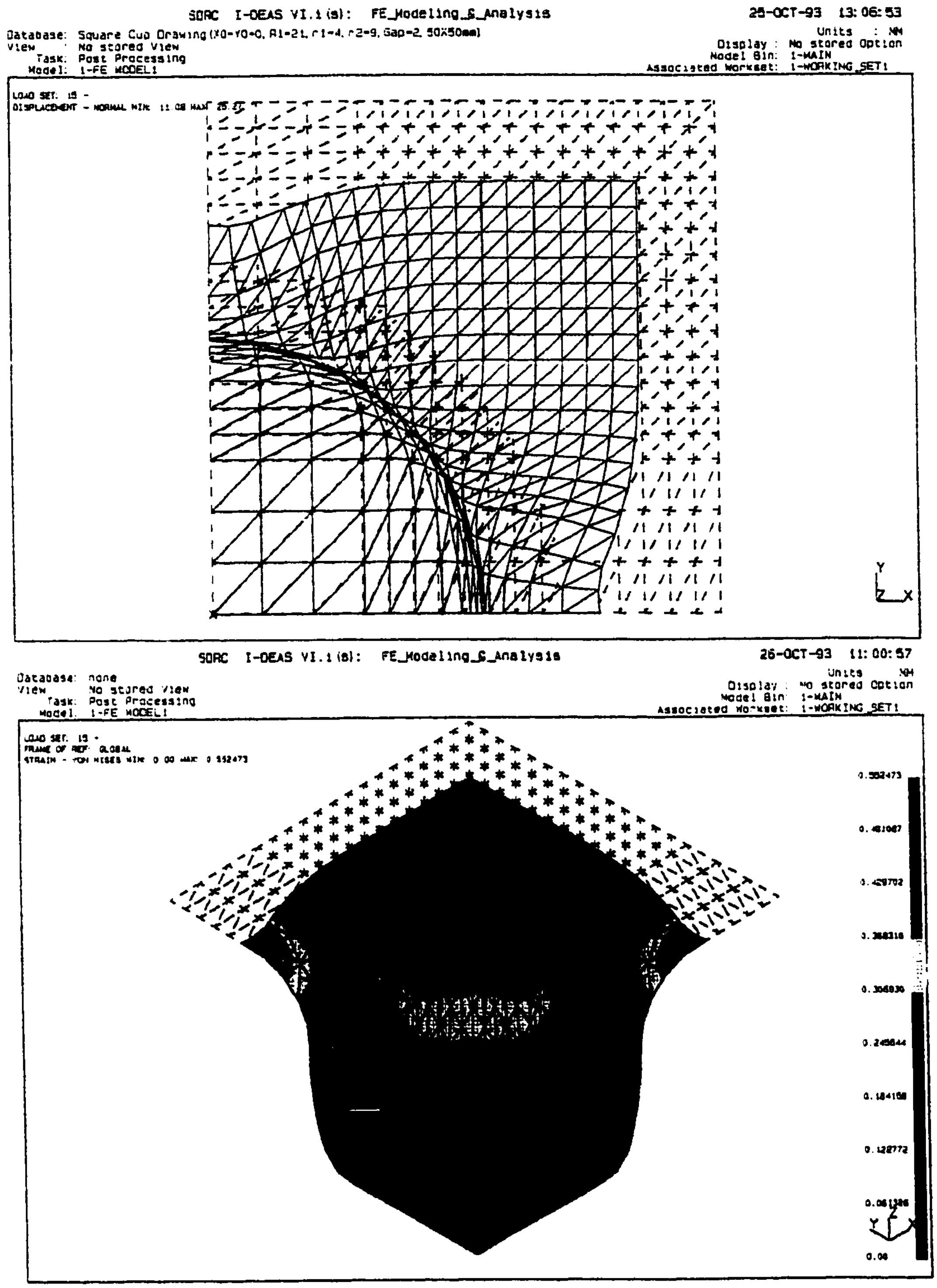

Figure 4.8(c) Square Cup Drawing with a Cylindrical Punch (Punch Depth = 25.27mm)

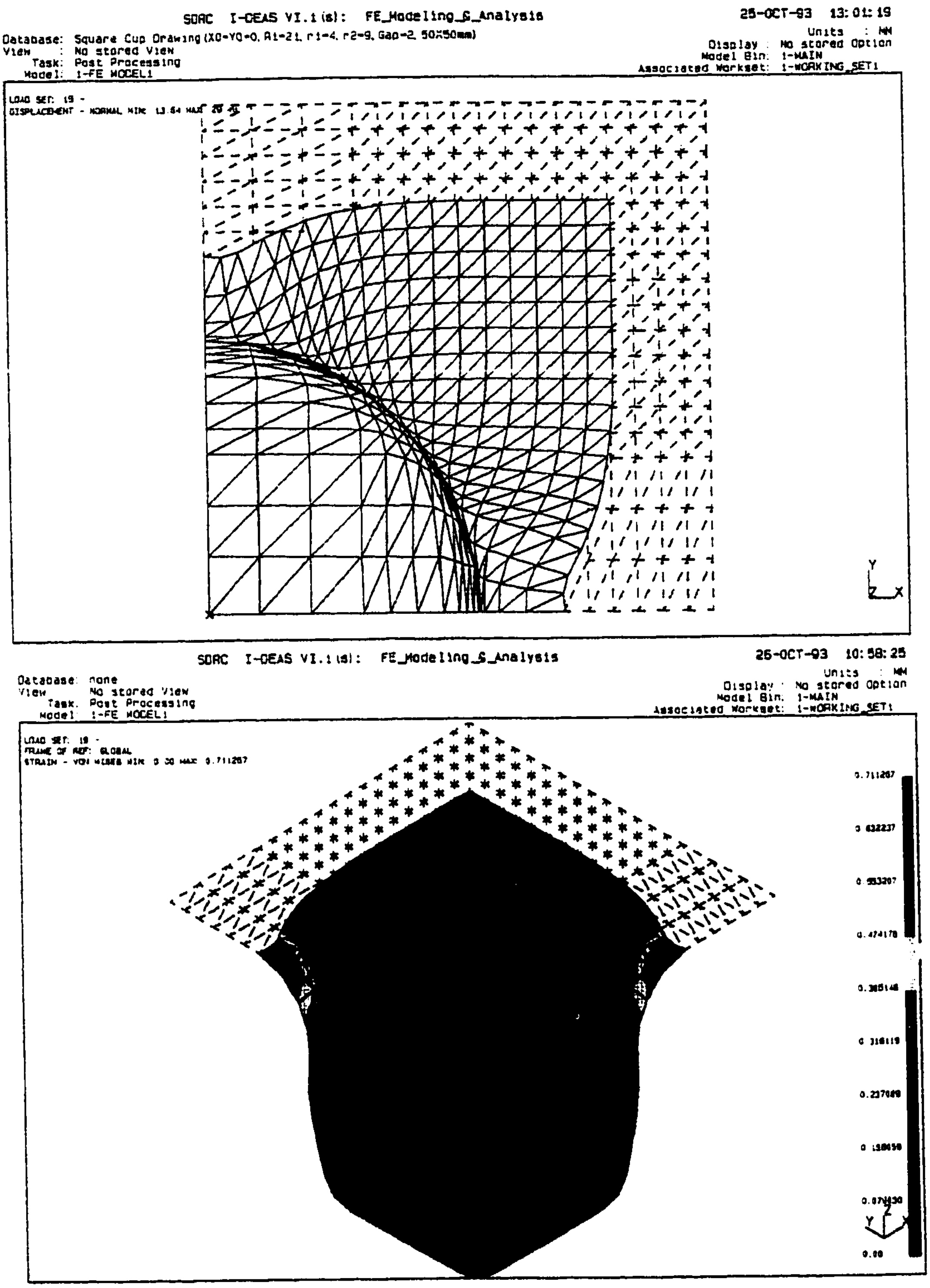

Figure 4.8(d) Square Cup Drawing with a Cylindrical Punch (Punch Depth = 29.49mm)

processes, one should very much careful in interpreting results. Discrepancies are still quite common in the nonliear analysis results.

To my knowledge, nonlinear finite element analysis has not reached the point that a reliable error estimation is achievable. In most cases, a converged equilibrium solution is the major goal. However, a converged solution is not necessarily the correct solution. Various element behaviours in various nonlinear situations are still very much unclear. Therefore, there is no surprise in seeing discrepancies among nummerical results. This is the single most important difference between linear and nonlinear analysis.

Figure 4.8 shows the simulation results for the cylindrical punch case. Three-node triangular element is used in the analysis.

Figure 4.9 shows the comparison between results from finite element analysis and experiment. The numbers shown in the table indicate a maximum discrepancy of less than 1% in flange shape is achieved.

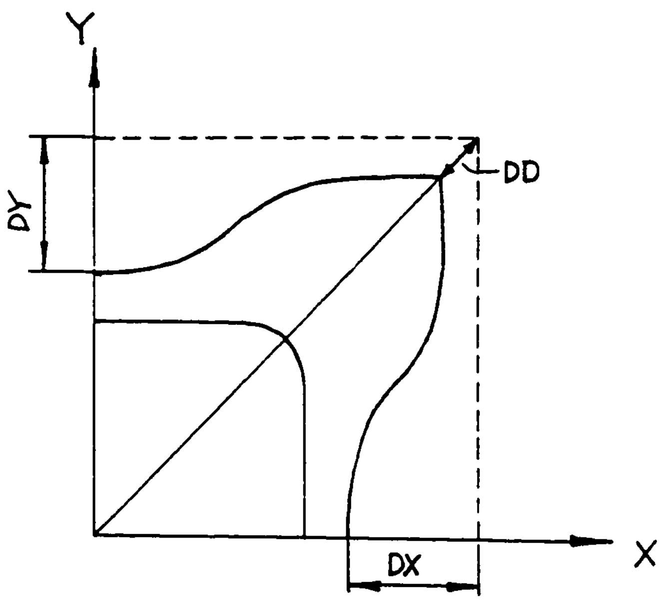

Punch Stroke	Dx & Dy Numerical	Dx & Dy Experiment	DD Numerical	DD Experiment
12.77	7.02	6.25	4.02	3.59
16.26	10.14	9.9	5.94	5.66
22.18	15.67	15.10	9.50	8.71
24.53	18.08	17.97	11.11	10.26

Figure 4.9 Comparison between results of FEA and Experiment

§9 References

[1] Ahmad, S. Irons, B.M. and Zienkiewicz, O.C. *Analysis ofthick and thin shell structure by curved finite elements*, Int. J. Numer. Meth. Engng. **2**, 1970, 419-451

[2] Hinton, E. and Owen, D.R.J., *Finite Element Software for Plate and Shell*, Pineridge Press, 1984

[3] Zienkiewicz, O.C., Taylor, R.L., and Too, J.M., *Reduced integration technique in general analysis of plates and shells*, Int. J. Numer. Meth. Engng. **3**, 1971, 275-290

[4] Hughes, T.J.R. and Taylor, R.L. and Kanoknukulchai, W. *A simple and efficient finite element for plate bending*, Int. J. Numer. Meth. Engng., 11, 1977, 1529-1543.

[5] Malkus, D.S. and Hughes, T.J.R. *Mixed finite element method - reduced and selective integration techniques: an unification of concepts*, Comput. Meth. Appl. Mech.Engng., 15, 1978, 63-81.

[6] Hughes, T.J.R. and Tezduyar, T.E. *Finite Element Based upon Mindlin Plate Theory with particular reference to the 4-node bilinear isoparametric element*, J. Appl. Mech., 48, 1981, 587-596

[7] Bicanic, N. and Hintion, E. *Spurious modes in two-dimentional isoparametric element*, Int. J. Numer. Engng., 14, 1979, 1545-1557.

[8] Cook, R.D. and Zhao-Hua, F., *Control of spurious modes in the nine node quadrilateral element*, Int. J. Numer. Meth. Engng, **18**, 1982, 1576-1580

[9] Kosloff, D. and Frazier, G.A. *Treatment of hourglass patterns in low order finite element codes*, Int. J. Numer. Anal. Meths. Geomech., 2, 1978, 57-72.

[10] Belytschko, T., Tsay, C.S. and Liu, W.K., *A stablization matix for the bilinear mindlin plate element*, Comput. Meth. Appl. Mech. Engng., 29, 1981, 313-327.

[11] Belytschko, T., Ong, J.S., Liu, W.K. and Kennnedy, J.M., Hourglass control in linear and nonlinear problems, Comput. Meth. Appl. Mech. Engng., 43, 1984, 251-276.

[12] Belytschko, T., Liu, W.K., *et al*, *Implementation and application of a 9-node Lagrange shell element with spurious control*, Comput. Struct., **20**, 1985, 121-128.

[13] Belytschko, T., Liu, W.K., *et al*, *Stress projection for membrane and shear locking in shell finite element*, Comput. Meth. Appl. Meth. Engng, **51**, 1985, 221-258

[14] Belystchko, T., Wong, B.L. and Chiang, H.Y., *Advances in one-point quadrature shell element*, Comput. Meth. Appl. Meth. Engng, 96, 1992, 93-107.

[15] Kant, T. and Datye, D., *Finite elements available for the analysis of curved thin-walled structure*, Bull, J.W. (ed.), Finite Element Applications to Thin Walled Structure, Elsevier Sci. Pub. Ltd, 1990, 1-40

[16] Dvorkin, E.N. and Bathe, K.J. *A continuum mechanics based four node shell element for general nonlinear analysis*, Eng. Comput., **1**, 1984, 77-88

[17] Bathe, K.J. and Dvorkin, E.N., *A formulation of general shell elements - the use of*

mixed interpolation of tensorial componenets, Int. J. Numer. Meth. Engng., **22**, 1986, 697-722

[18] Huang, H.C. and Hinton, E., *A nine node Lagrangian Mindlin plate element with enhanced shear interpolation*, Eng. Comput., **1**, 1984, 369-379

[19] Huang, H.C. and Hinton, E., *A new nine node degenerated shell element with enhanced membrane and shear interpolation*, Int. J. Numer. Meth. Engng., **22**, 1986, 73-92

[20] Boisse, P. *et al*, *A simple isoparametric three node shell finite element*, Comput. Struct., **44**, 1992, 1263-1273

[21] Gelin, J.C., Boulmane, L. and Boisse, P., *Quasi-static implicit and transiant explicit analysis of sheet metal forming using a C^0 three node shell element*, Proc. of the 2nd Int. Conf. NUMISHEET'93, Isehara, Japan, 1993, 53-64

[22] ABAQUS 5.2, Theory Manual, 1994.

CHAPTER 5

Conclusions

§1 Conclusions

Metal forming has been a major challenge to modern nonlinear mechanics, because almost every such process involves all three major nonlinearities, i.e. large deformation, boundary contact and material nonlinearity. In applications, difficulties arise also numerically, such as, element distortion, volume locking, shear locking and etc. Therefore, the success of the numerical simulation of metal forming processes demands a systematic effort to attack various aspects of such a procedure. In this work, efforts are focused on three major areas.

The first is a consistent large deformation formulation based on continuum mechanics theory. In this area, the mathematical complexity and, sometimes, lack of common definitions of the discussion make it difficult to have a clear understanding of the various formulations in most of the publications. It is even more difficult to envision the details of numerical implementation, most of which have not been "standardized" to a textbook level. It is common in this area that different researchers publishes different analysis results with seemingly identical formulation theory. It is author's intention in chapter 2 to layout a clear and consistent formulation from the view point of implementation and coding. To facilitate achieving this purpose, an unique mathematical derivation is systematically developed. The uniqueness of this derivation is the absence of using any pseudo stress and strain tensor, which makes it much easier to present the entire mathematical process with clear physical interpretations throughout and, therefore, reduce the degree of ambiguity in implementation. For example, the need of a co-rotational stress increment tensor is so naturally derived that the complex mathematical descriptions about objective stress rates are simply bypassed. Under this unique frame, various aspects of numerical formulation and implementation are presented consistently. The other important aspect in nonlinear FEA is the "element performance" which has been much less focused in the large deformation literature than mechanical formulations. Due to the severity of the deformation endured by the mesh, the success of the analysis sometimes very much depends on the ability of the elements to perform in the situation. Throughout this work, particularly in presenting numerical examples, the author has also intended to present the issue as much as the author's experience allows. In Chapter 2, different elements are used in numerical calculation for comparison.

The contact boundary with friction is another challenge for numerical stability. A bond element algorithm is formulated and discussed in chapter 3 for the issue. The same algorithm may be presented under the concept of penalty method, however, for easier interpretation for people with engineering background, it is presented in the current bond element (or nonlinear spring) format. The algorithm is tested on the traditional ring compression problem. Excellent numerical stability and results are observed and presented. Comparisons with other publications are not particularly mentioned in this thesis. However, they are available in my master thesis and many literatures.

The last focus of this study is to implement the large deformation formulation into the 3D degenerated shell elements for the purpose of simulating sheet metal stamping processes. At first, a detail description on various aspects of implementing large deformation theories presented in Chapter 2 into the shell element formulation is presented. This is a particularly difficult area. Apart from the problems discussed in Chapter 2, the defect in degenerated shell element itself (i.e. shear locking or its inability to present Kirchhoff condition in thin shell situation) also imposes great numerical challenges for numerical stability. This has been a focus of many publications. A comprehensive summary of these studies are presented in Chapter 4. Based on the author's understanding about the cause of shear locking, a new algorithm is designed and successfully implemented in various degenerated shell elements. The principle of the algorithm is to enforce the Kirchhoff condition on the degenerated shell elements in the form of an extra penalty term. The major advantages of this algorithm are that it is clear targeted and very much independent of other part of numerical formulations so that it can be used on any degenerated shell elements either independently or combined with other algorithms in the literature. The numerical examples presented at the end of the chapter has demonstrated the effective of algorithm, where the algorithm is the only measure used to prevent the elements from shear locking.

§2 Recommendations for Future Work

Since the first draft of thesis was finished in June 1994, I have been able to continue my career in this field at Forming technologies Incorporated (FTI), Oakville, Ontario. The work experience at FTI has provided me an unique exposure to another breed of sheet metal forming solver, i.e. inverse one step solver. My research work there also allowed me to explore shell elements further. Those experiences have helped me to form a stronger view of the possible future enhancement of the work summarised in this thesis.

The major concerns in developing an incremental FEA solver for sheet metal forming have been efficiency and robustness. The solver developed here has to be faster and more robust in convergency for industrial applications. There two enhancements, in my view, could greatly help the current solver to be competitive in the field. One is to introduce a new breed of reduce-integrated shell elements, with a particular emphasis on the Belytschko type of 4-node elements (1 point integration with hourglass control). These types of shell elements are reputable for their numerical efficiency and resistance to shear locking. Combined with the technique discussed in Chapter 4, the formulations should be ideal for a efficient and reliable incremental solver. A newly published book by Richard MacNeal[1] was the first FEA reference book with particular emphasis on the development of new elements and the prevention of problems existing in conventional elements. The author's long time endeavour in developing NASTRAN codes gives the book the authority for the subject. The other important improvement could come from the implementation of the so-called "consistent tangent modular matrix"[2] algorithm. The algorithm was first derived by Simo and Taylor[3], which develops a stiffness matrix fully consistent with the backward-Eular stress integration algorithm (redial return method mentioned in Chapter 2 is a special form of this algorithm) in residual force calculation. This algorithm can dramatically increase the convergence rate and the magnitude of each increment.

The success of one step type of solvers should trigger rethinking of some of the traditional incremental approach. Compared with incremental solvers, one step solvers usually have two unique characteristics: one is to start from deformed geometry (inverse approach), the other is the much simplified constitutive relation (deformation theory) which ignores the deformation history completely. However, the convincing fact is that one step solutions from majority of sheet metal forming analysis are very much similar to the solutions by incremental solver, only at the dramatically reduced cost. The indication is clear that many of the traditional complicated assumptions on the sheet metal forming processes may not as critical as traditionally thought. The best improvement may only be achieved by dramatically changed thinking.

§3 Reference

[1] MacNeal, Richard H., *Finite Elements: Their Design and Performance*, Marcel dekker Inc. 1994

[2] Crisfield, M. A., *Nonlinear Finite Element Analysis of Solids and Structures*, John Wiley & Sons, 1995

[3] Simo, J. C. and Taylor, R. J., *Consistent tangent operators for rate-independent elasto-plasticity*, Comp. meth. Applied Mech. & Engrg., 48, 1985, p101-108